

DSE - Airborne Wind Energy

Design an automated launching and landing system for a rigid wing airborne wind energy system

M.T. van Beek	4368134	T.J.S. Gertsen	4224590
G.J. Bouman	4227964	D.H.A. Groeneveld	4372832
F. Bouwman	4371038	Y.C. Heijne	4389476
Y. Chiodi	4227271	J.W.D. Kroese	4371305
R.R. Fanijten	1356542	D. Sud	4345029

Technical Design Report
Design Synthesis Exercise

Preface

The Design Synthesis Exercise (DSE) is an eleven-week full time project that is performed at the end of the Aerospace Engineering bachelor at Delft University of Technology with a group of ten students. The subject comes from a research department of the university in collaboration with two companies named Ampyx Power and KitePower. The target of this project is to design a fully autonomous launching and landing system for an Airborne Wind Energy (AWE) system based on the design of the 2014 DSE group which designed a rigid kite. [19] Therefore it is advised to gain knowledge of their research first.

This report is the final report out of a series of four and can be used to gain insights in the final version of the rigid kite. Decided was to integrate an autonomous launching and landing system in the rigid kite and thereby creating an off-the-shelf product that can be sold to both the public and private sector. Readers who would like to get a global overview of the project and the design are advised to read the executive summary.

We as project group would like to thank and express our appreciation to Roland Schmehl as our principal tutor and Hussein Farahani and Yi Zhang as our coaches. We would also like to thank Ampyx Power and KitePower as our customers and Twingtec and Kitemill for supporting us with information and feedback. Finally we would like to thank PhD student Sebastian Rapp for his feedback throughout the project and the Organisational Committee (OSCC) for setting up this project.

Delft, DSE Group 24

July 2017

Contents

Preface	III
Executive overview	VII
Nomenclature	XV
1 Introduction	1
2 Concept development	3
2.1 Requirements & constraints	3
2.2 Concept analysis	4
2.3 Trade-off	4
3 System analysis	7
3.1 Functional flow block diagram	7
3.2 Functional breakdown	8
3.3 N2 chart	8
3.4 Communication flow diagram	9
3.5 Data handling	9
3.6 Resource allocation	11
3.7 Power performance analysis	13
3.8 Technical risk analysis	18
4 System interfaces	21
4.1 Configuration & lay-out	21
4.2 Electric systems	22
5 Aerodynamics	27
5.1 General principles	27
5.2 Specifications	33
5.3 Final design	33
6 Stability & control	39
6.1 Flight paths	39
6.2 Stability	52
6.3 Control	59
7 Power & propulsion	63
7.1 Airfoil selection	63
7.2 Main rotor sizing	64
7.3 Tail rotor sizing	67
7.4 Motor sizing	69
7.5 Battery sizing	72
7.6 Wire sizing	75
8 Structures	77
8.1 Ground station	77
8.2 Kite	79
9 Verification & validation	93
9.1 Guidelines & procedure	93
9.2 Rotor sizing model	93
9.3 Power model	94
9.4 Structural model	96
9.5 Aerodynamic model	97
9.6 Stability & control	98

10 Sensitivity analysis	101
10.1 Scalability	101
10.2 Mass & centre of gravity	102
10.3 Tether & drum diameter	103
11 Financial projection	105
11.1 Cost breakdown structure	105
11.2 Return on investment	105
11.3 Market analysis	106
12 Sustainable development strategy	111
12.1 Sustainable use of materials	111
12.2 Sustainable integration into the surroundings	112
12.3 Economical sustainable future	112
13 Project design & development logic	113
13.1 Design & development	113
13.2 Operations & logistics	114
14 Requirements compliance	117
14.1 Requirements compliance matrix	117
14.2 Feasibility analysis	118
Conclusion	121
Recommendations	123
Bibliography	127
Appendices	129
A Functional analysis	129
A.1 Functional flow diagram	129
A.2 Functional breakdown	130
B Fault tree analysis	131
C Cost breakdown structure	132
D Replacement costs	134
E Operations and logistics diagram	135
F Component mass breakdown	136
G Task division	137

Executive summary

In this chapter the executive summary, or overview of the project, is presented. First the mission is analysed, the objective is stated and the most important requirements are stated. The next section elaborates on the concepts and the trade-off method. After that, the final design is presented and the most important performance specifications are stated. The next section contains the financial analysis and the projected costs of the system. Finally, conclusions and recommendations are presented in the last section.

Mission analysis

Background

Scientists and engineers around the globe are constantly researching and developing new ways of generating renewable energy, and making it economically feasible. Kite power generation is a type of Airborne Wind Energy (AWE) technology, that is starting to prove its economical viability. Airborne Wind Energy kites can be a more material and cost efficient alternative to horizontal axis wind turbines. This is due to the fact that they are not carried by a huge supporting structure, but stay up in the air using lift force. However, an important problem arises as it is required that the kite reaches its operational altitude and can be landed safely when conditions are not suitable. Therefore, a fully automated launching and landing system for a rigid wing airborne wind energy system has to be developed.

Mission statement

A mission need statement can be defined from the above stated problem:

A fully autonomous system that can safely and reliably launch and land the tethered 2014 DSE airborne wind energy aircraft.

From this mission need, a project objective statement is derived:

Design an economically competitive fully autonomous system that can launch and land the 2014 DSE airborne wind energy aircraft using a 10 FTE team for 10 weeks.

Requirements

The mission need and objective statement give guidance and direction to the project. However, in order to constrain the possible solutions, a set of requirements was specified for the project by an external customer. The most important requirements are stated here:

- The system shall be fully compatible with the 2014 DSE AWE aircraft.
- The system shall have an output of no more than 40 kW during the reel-out phase.
- The system shall have a functional lifetime of 20 years.
- The system shall require maintenance no more than once every 3 months.
- The system shall have a cost price of no more than €40.000 for one complete system.
- The launching and landing system shall be scalable to a 2MW system

In order to start generating concepts for the design, a good understanding is required of what the design needs to do. With the requirements as constraints on the system, the functionality of the system can be determined. A **functional flow** was made for the system, and the top-level functions outline the scope of the project:

1. Initialise launch system
2. Launch aircraft
3. Perform nominal flight
4. Land aircraft
5. Store aircraft
6. Perform scheduled maintenance

Concepts and trade-off

After the mission was clearly defined and the requirements thoroughly investigated, a large number of possible concepts to launch and land the aircraft was established. These concepts were sanity checked and the infeasible options were discarded. This resulted in four final concepts that moved on to the final concept trade-off.

- **Linear rail:** a horizontal take-off along a rail using a hydraulic catapult.
- **Lighter-than-air:** a helium-filled balloon that can lift the kite to operational altitude.
- **Multi-copter:** operationally comparable to the lighter-than-air concept, but with a drone instead of a balloon.
- **Vertical take-off and landing:** uses rotors on the kite to take off and climb vertically like a drone.

The four concepts were worked out and analysed technically to get a clearer picture of the feasibility of each solution. After this, a trade-off method was developed with which the four concepts could be compared quantitatively. The trade-off method was designed to incorporate the Levelised Cost of Energy (LCOE). The LCOE is a measure of how much the system costs per unit of energy produced and is expressed in €/kWh. The LCOE gave rise to 11 weighted criteria that were used to assess the four concepts. With these criteria a trade-off table was made for each concept and the results are shown in table 1. As can be seen, the linear rail, VTOL, and the multi-copter have a similar score. The weights were changed in order to see what happens to the scores, but that still gave no significant differences between the concepts. Therefore a vote was done internally and the **VTOL** concept came out as final design solution.

Table 1: Trade-off of the four concepts

	Linear rail	Lighter-than-air	Multi-copter	VTOL
Aerodynamics (29%)	2	2	3	2
Mass (9%)	3	3	3	1
Launch energy (7%)	3	4	2	2
Land energy (7%)	3	4	2	3
Maintenance interval (7%)	4	3	4	4
Service costs (7%)	2	1	3	3
Chance of failure (14%)	3	2	3	4
Cost of failure (8%)	3	1	3	4
Man hour costs (3%)	3	2	2	4
Kite attachment costs (3%)	4	1	1	3
Ground station costs (4%)	2	1	4	4
Total	26%	21%	27%	26%

Detailed design

System configuration

The VTOL concept configuration is shown in figure 1. The technical drawing shows the isometric, top, side, and front view of the kite. As can be seen in the drawings, three rotors were added to the DSE 2014 kite design. The rotors on the wing will be used for lifting the kite, the tail rotor will be used to stabilise the kite.

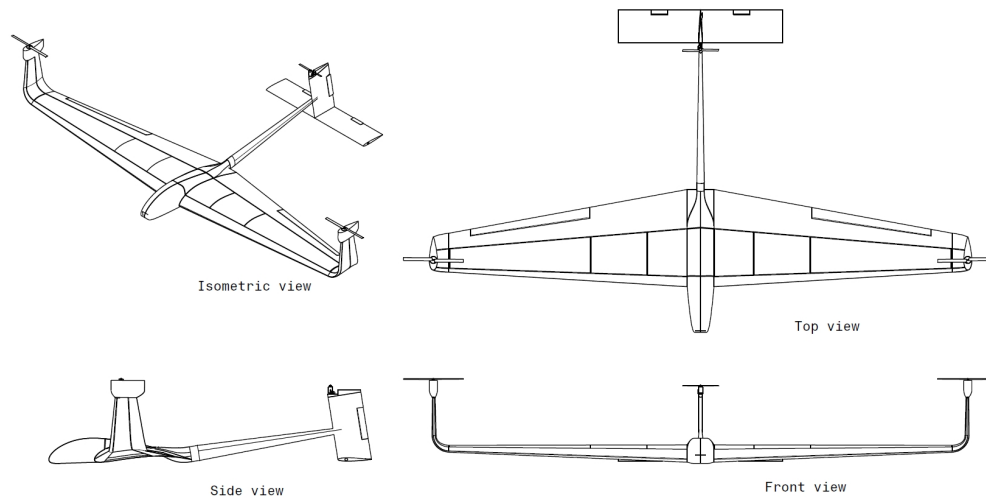


Figure 1: Technical drawings of the VTOL design

Power generation

The power output is an important aspect of the wind energy system. The system will generate power during the reel-out phase by pulling on the tether, and it will consume power during the reel-in phase, because the tether will need to be retracted. The power generated during the traction phase and the power input needed during the reel-in phase were calculated and from this the average power output could be obtained. Finally, the rated power was calculated, which is the power generation under the optimal conditions. The results can be seen in table 2.

Table 2: Summary of the power and energy produced

Parameter	Value
Rated cycle power	116 [kW]
Average cycle power	43 [kW]
Annual energy produced	248 [MWh]
Capacity factor	38%

Aerodynamics

In order to analyse the aerodynamic properties of the kite, the program XFLR5 was used. With the use of XFLR5 the 2D airfoils can be analysed, after which they can be modelled into a 3D wing. Furthermore,

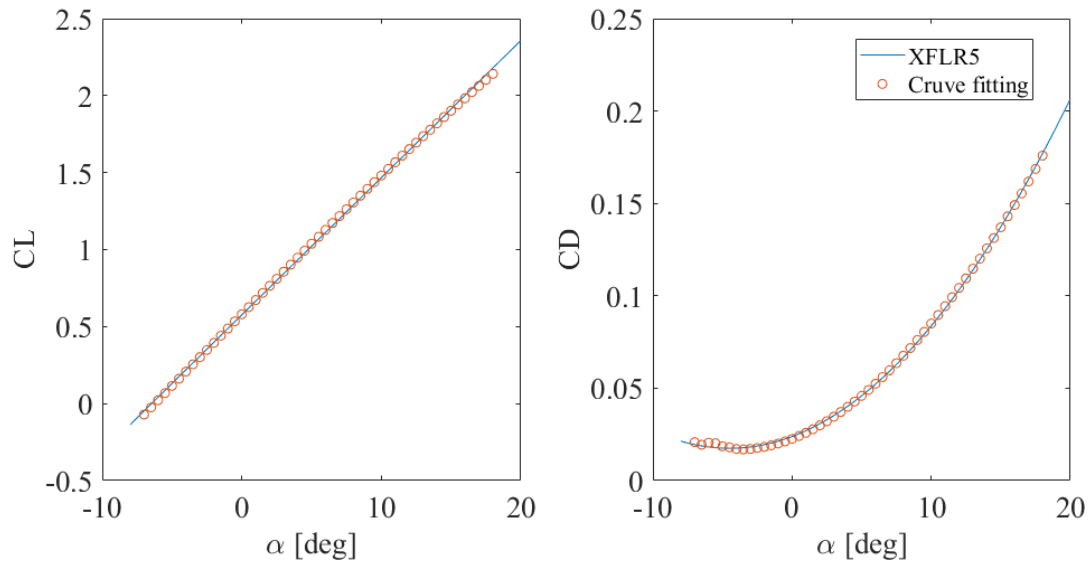


Figure 2: Curve fitting for lift and drag coefficients from XFLR5 data of the whole rigid kite

rotors and wing tips needed to be added to the design to allow for vertical take-off and landing. The XFLR5 program could not model the aerodynamic changes of these alternations so an alternative method had to be used. The rotors were modelled as flat plates, this way a drag coefficient was obtained which could be used as input in XFLR5. The aerodynamic properties for the entire kite can be seen in figure 2.

Finally, the rotor/wing interaction was investigated to determine how much the wing affects the propeller effectiveness. An extensive literature study was done, and the theory was compared with data from the V22 aircraft, which has a similar propeller layout. In conclusion, a wing download -including safety margin- of 8% was obtained.

Power & propulsion

Thrust needs to be generated using rotors to be able to perform the launching and landing manoeuvres. The airfoil that is used for the rotors is the NACA 4412 airfoil, because of its high C_{L0} value which contributes to the amount of thrust that can be generated. In order to size the rotors, Blade Element Theory (BET) was used. An extensive model was made that optimised the rotors for the necessary thrust setting of 437 N. The tail rotor was sized for a thrust of 70 N. The results can be seen in table 3.

Table 3: Rotor characteristics

(a) Output parameters for the main rotor geometry and (b) Output parameters for the tail rotor geometry and corresponding rpm setting

Output	Value	Output	Value
R	0.538 [m]	R	0.31 [m]
c	0.0556 [m]	c	0.0323 [m]
Ω	4750 [rpm]	Ω	6825 [rpm]
$\vartheta(x)$	14 - 6.6667x	$\vartheta(x)$	14 - 6.6667x
M	0.7438 [-]	M	0.7438 [-]
Q	16.77 [Nm]	Q	2.1872 [Nm]

After the propellers were sized, the motors were chosen. It was opted to use brushless direct current (BLDC) motors because of their high efficiency and long lifetime. Furthermore, the efficiencies and the required power were calculated for both the main and the tail rotors, the results are presented in table 4. The motors that provide the required power for the main propellers and the tail propeller are the R-Snake 154 series, and the Hacker Q80-6L V2 respectively. Finally, the batteries were sized and it was found that Lithium Manganese Oxide batteries with a total mass of 18 kg were needed.

Table 4: Safety factor, efficiencies and Power required for the tail and the main rotor

(a) Safety factor		(b) Power required for main rotor		(c) Power required for tail rotor	
Parameter	Value	Parameter	Watt	Parameter	Watt
S	1.5 [-]	P_p	8228.5	P_p	908.2
η_{motor}	0.86 [-]	P_i	6120.4	P_i	1153.4
η_{fom}	0.7438 [-]	Total (incl. η_{total})	22432	Total (incl. η_{total})	3223
η_{total}	0.6397 [-]	Total (incl. S)	33648	Total (incl. S)	4834

Stability & control

A key component of designing an automated launching and landing system for the rigid kite is the suitable trajectory that the kite should follow under different conditions. Simulating the climb and descend phase of the rigid kite is important in understanding the flight performance characteristics. The trajectories for climb and descent were modelled and simulated in MATLAB. One trajectory, the ideal trajectory for a wind speed of 6.8 m/s, can be seen in figure 3. The necessary tail thrust for equilibrium was calculated using MATLAB models. After the ideal flight trajectories and equilibrium have been determined, the stability of the kite was analysed for climb and for hover. It was concluded that both for hover the kite is statically stable. However, the kite requires active stabilisation from the tail rotor during the climb phase.

Structures

The first structural components of the system that were analysed are the tether and drum of the ground station. Instead of using the common method of choosing a tether diameter and iterate till the tether is sized for a certain lifetime it is chosen to take a certain design lifetime and calculate backwards to the corresponding tether diameter. Since the main goal to achieve with AWES is a competing LCOE this is a more straightforward method as one can choose a certain lifetime for which the system will be profitable. The kite was also analysed structurally by the use of the stress analysis theory. The parts that were analysed are the wing box, the tail beam, the empennage, and finally the winglets and tail beam attachment. Several load cases were defined and it was checked whether the aforementioned structural parts fail under the specified load case. The main conclusion from these analyses is that the tail beam thickness was reduced to increase the kite stability, and that its skin should be made of the high-strength carbon fibre T700S.

Table 5: Tether and drum dimensions

Description	Value
Tether diameter (nominal)	9.59 [mm]
Tether diameter (worked-in)	8.15 [mm]
Drum diameter	768 [mm]
Drum length	2.37 [m]
Pulley diameter(s)	768 [mm]

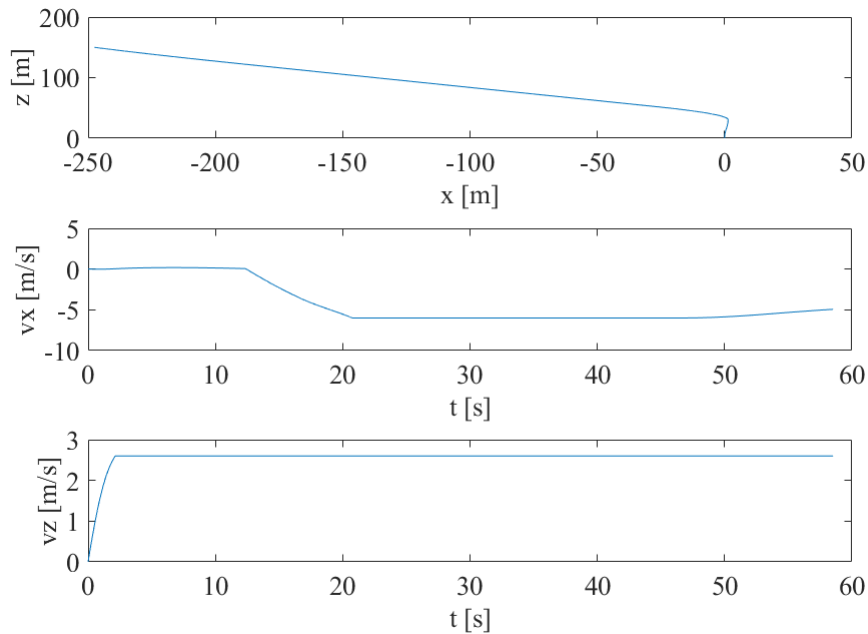


Figure 3: Climb trajectory of the rigid kite at $V_w = 6.8$ m/s at 100 m

Cost analysis

With the entire system known, a first estimate for the cost can be made. A detailed cost breakdown was made, and a summarised table is presented in table 6a. Furthermore, in order to financially sustain the system, a positive Return on Investment (RoI) is required. Since the designed system will approximately cost €65,374 when 150 systems are expected to be sold, a certain price per kWh, which is called Levelised Cost of Energy (LCOE), is required to ensure profit is made. It can be seen in table 6b that by taking 95€/MWh as LCOE, investing in the system becomes viable and profitable.

Conclusion and recommendations

It was concluded that a VTOL concept is the best approach to meet performance requirements and design constraints. Furthermore, the concept also meets reliability, availability, maintainability and safety requirements. In the preliminary design phase of the VTOL concept, two propellers are added to the wingtips, and winglets were used to create an offset from the wing. Furthermore, a tail rotor was added to provide pitch control.

The subsystems aerodynamics, stability and control, power and propulsion and structures were analysed in detail. The main conclusion for the aerodynamics is that the added winglets increase the lift over drag ratio, and that 8% of the thrust is lost due to rotor wing interaction. In the structural analysis it was concluded that the critical part of the structure is the tail beam, but when using the high strength carbon fibre T700S it can handle the loads generated during nominal flight. The power and propulsion designed a configuration with two vertically oriented main rotors and a horizontally oriented rotor on the vertical tail. Their rotor radii are respectively sized to 54 cm and 7 cm and the motors to drive these rotors were sized and found to require 35 kW and 7 kW of power. The stability and control analysis concluded that the kite needs active stabilisation using the tail propeller during climb.

Table 6: Cost analysis

(a) Summarised cost breakdown		(b) Return of Investment calculation summary	
Description	Value	Description	Value
Expected #systems sold	150	Expected systems sold	150
Total Development cost	€930,262	System costs	€65,374
Production cost ground station	€21,070	Annual energy production	281,000 kWh
Production cost kite	€38,103	Replacement costs	€4,161.32/y
Total cost per system	€65,374	General maintenance	€1,800.00/y
		Insurance	€1,000.00/y
		Tax rate	52%
		Annual inflation	2%
		Annual discount	8%
		MARR	10%
		RoI for 80 €/MWh	9 %
		RoI for 95 €/MWh	12%

The average power per cycle is determined for different reference wind velocities. Found was a rated power per cycle of 116 kW, an average power per cycle of 43 kW and a capacity factor of 38%. When combining the energy generated with the estimated costs per system that was found to be €66,500, the return on investment is 11% when the energy produced is sold for €95/MWh. The market analysis showed that if the energy is sold for this price, the system is a competitive product while having room and profit to keep on innovating.

The main recommendations for future work are related to two design errors. The first is an overestimation of the required power. Correcting this and using the right equations would result in a much lower power requirement for each motor. The second error that could be improved is the estimation of the mass of the sandwich panel in the kite. The error has been assessed and it was found that the mass would increase to 106.7kg. Finally, some improvements to power, take-off, and rotor models are suggested.

Nomenclature

Abbreviations

AR	Aspect Ratio
AWE	Airborne Wind Energy
AWG	American Wire Gauge
BET	Blade Element Theory
BMS	Battery Management System
C-rate	Battery discharge rate
CBS	Cost Breakdown Structure
CFD	Computational Fluid Dynamics
CTF	Cycles To Failure
D4S	Design for Sustainability
DSE	Design Synthesis Exercise
ESC	Electronic Speed Controller
FBS	Functional Breakdown Structure
FEM	Finite Element Method
FFBD	Functional Flow Block Diagram
FoM	Figure of Merit
LMO	Lithium Manganese Oxide
MARR	Minimum Acceptable Rate of Return
MCU	Micro Controller Unit
NPW	Net Present Worth
OSCC	Ontwerp Synthese Coördinatie Commissie
RoI	Return on Investment
rpm	Revolutions per minute
SCOE	Society's Cost of Energy
SF	Safety factor
SSL	Safe Service Life
TRL	Technology Readiness Level
V&V	Verification and validation

Symbols

α	Angle of attack	[rad]
α	Friction coefficient	[-]
α_0	Zero lift angle	[rad]
Δr	Tether length step	[m]
Δt_{out}	Reel-out time step	[s]
κ	Temperature lapse rate	[K/m]
λ	Inflow factor	[-]
Ω	Angular velocity	[rad/s]
\bar{z}	Neutral axis z-position	[m]
φ	Angle between the horizon and the apparent velocity	[deg]
φ	Azimuth angle	[deg]
φ	Inflow angle	[rad]
ρ	Atmospheric density	[kg/m ³]
ρ	Density	[kg/m ³]
σ	Stress	[N/m ²]
τ	Shear stress	[N/m ²]
ϑ	Elevation angle	[deg]
ϑ	Pitch angle	[rad]
ϑ	Root pitch angle	[rad]
$\vartheta_{75\%}$	Pitch angle at 75% of the radius	[rad]
\tilde{z}	Area element z-position	[m]
\vec{F}_A^a	Aerodynamic force	[N]
\vec{T}^b	Thrust force	[N]
\vec{v}_{app}	Apparent aerodynamic velocity	[m/s]
\vec{W}^e	Weight	[N]
ζ	Force offset	[m]
A	Area	[m ²]
A	Swept area	[m ²]
a	Lift slope	[1/rad]
a	Semi-major axis	[m]

B	Boom area	[m ²]	g ₀	Gravitational acceleration	[m/s ²]
b	Boom distance	[m]	h	Height	[m]
b	Semi-minor axis	[m]	h	Operational altitude	[m]
b	Wingspan	[m]	h _{ref}	Reference altitude connected to a reference wind velocity	[m]
c	Chord length	[m]	I	Area moment of inertia	[m ⁴]
C _D	System drag coefficient	[-]	k _i	Empirical correction factor	[-]
C _L	Kite lift coefficient	[-]	k _q	Torque constant	[Nm/A]
C _P	Power coefficient	[-]	k _v	Voltage constant	[rpm/V]
C _Q	Torque coefficient	[-]	L	Lift	[N]
C _T	Thrust coefficient	[-]	l	Length	[m]
C _{D_k}	Kite drag coefficient	[-]	M	Figure of Merit	[-]
C _{D_t}	Tether drag coefficient	[-]	M	Molar mass of air	[kg/mol]
C _{d_t}	Circular tether drag coefficient	[-]	M	Moment	[Nm]
C _{D₀}	Drag coefficient at zero AoA	[-]	m	Mass	[kg]
C _D	Drag coefficient	[-]	N	Number of blades	[-]
C _{L₀}	Lift coefficient at zero AoA	[-]	P	Force	[N]
C _L	Lift coefficient	[-]	p	Atmospheric pressure	[N/m ²]
C _P	Betz limit	[-]	p	Distributed load	[N/m]
CF	Crest factor	[-]	p	Moment arm	[m]
D	Drag	[N]	P _a	Generated power	[W]
d	Distance	[m]	P ₀	Standard atmospheric pressure on sea level	[N/m ²]
DL	Wing download	[N]	P _{cycle}	Power generated per cycle	[W]
E _{impact}	Impact energy at landing	[J]	P _{in}	Power consumed during reel-in	[W]
E _{in}	Reel-in energy	[J]	P _{out,i}	Power generated during reel-out per altitude	[W]
E _{out}	Reel-out energy	[J]	Q	Torque	[Nm]
F	Force	[N]	q	Shear flow	[N/m]
F _{imp}	Impact force at landing	[N]	R	Radius	[m]
f _{out}	Normalised reel-out velocity	[-]	R	Universal gas constant	[JK/mol]
F _r	Tether force during reel-in	[N]	r	Tether length	[m]
F _{t,max,i}	Maximum tether force during reel-out per altitude	[N]	S	Shear force	[N]
g	Gravitational acceleration	[m/s ²]	S	Surface area	[m ²]

s	Solidity factor	[-]	V_a	Apparent kite velocity	[m/s]
T	Temperature	[K]	$V_{r,in}$	Reel-in velocity	[m/s]
T	Thrust	[N]	$V_{r,out,i}$	Reel-out velocity per altitude	[m/s]
t	Thickness	[m]	$V_{w,ref}$	Wind velocity at reference altitude	[m/s]
T_0	Standard temperature on sea level	[K]	V_w	Wind velocity	[m/s]
t_{in}	Total reel-in time	[s]	w	Width	[m]
t_{out}	Total reel-out time	[s]	W_{kite}	Weight of the kite	[N]
V_c	Climb velocity	[m/s]	$X_a Z_a$	Aerodynamic reference frame	[-]
V_i	Induced velocity	[m/s]	$X_b Z_b$	Body reference frame	[-]
$V_{a,i}$	Apparent kite velocity during reel-in	[m/s]	$X_e Z_e$	Vehicle carried Earth reference frame	[-]
$V_{a,o,i}$	Apparent kite velocity during reel-out per altitude	[m/s]	$X_g Z_g$	Ground station reference frame	[-]
			z	Vertical offset	[m]

1 | Introduction

For many years the global energy transition, from fossil fuels to renewable energy, has been a pressing matter on the agendas of the world's political leaders. Lately, it is becoming more apparent that a decarbonised energy market is necessary to meet the environmental goals set by the 2015 Paris Climate Agreement. The development of renewable energy sources has taken huge leaps in the past years, but still faces heavy competition from the currently established fossil fuels sector. Policy makers around the globe are pressing measures like low-carbon and energy efficiency mandates, introducing carbon taxes, and extensive energy market reforms. On the other hand, scientists and engineers should keep researching and developing new ways of generating renewable energy, and making it economically feasible. Kite power generation is a type of Airborne Wind Energy (AWE) technology, that is starting to prove its economical viability. AWE is aiming to compete with conventional wind turbines, and is promising to become a big player in the renewable energy market, since material costs can decrease up to 90% when compared to horizontal axis wind turbines. However, a problem arises when using AWE systems, since they require a lot of manpower during operation, as opposed to conventional wind turbines. Therefore, a robust and sustainable way of autonomously launching and landing AWE kites needs to be developed.

The purpose of this final report is to provide a detailed design of an automated AWE system, with a launching and landing system integrated in the design. In previous design phases, a Vertical Take-off and Launch (VTOL) concept was chosen to be most suitable to design an AWE system. The baseline for the designed concept is a previous design from the Fall 2014 DSE group 03. [19] Winglets are added to their design, to which a rotor is implemented to provide sufficient thrust for a climb towards operational altitude. By adding the rotors, a full AWE system is designed, which is viable and commercially attractive. The final design is made by doing a full analysis of the aerodynamics with the added winglets and rotors. A flight path is designed for both take-off and landing, for which stability measures are taken to ensure safe travels to operational altitude. The rotors are designed for these paths, after which motors and battery sizing is performed. A complete structural analysis is done for both the kite and the ground station, which ensures no failure should occur throughout the mission. For this designed system, electrical and data blocks are determined according to the created functional flow diagrams. A complete Catia model is created to obtain an estimate for the centre of gravity and mass budget. Financial projections are created to assess the feasibility of the project, together with a timeline for further development and an approach to achieve sustainability. Finally, a technical risk analysis based on the Reliability, Availability, Maintainability and Safety (RAMS) method is done together with verification and validation, which ensures a reliable product.

This report starts with a description where the project start-up is explained, consisting of the concept development in chapter 2. Next, the final design is presented, starting with a full system analysis in chapter 3. This system analysis consists of a functional breakdown, communication diagrams, configuration lay-out and resource and power allocations, together with an accurate and revised power model. In chapter 4 the system interfaces are defined. In chapter 5, an aerodynamic study is performed on the kite. After that, a stability & control research is done in chapter 6 for the entire flight envelope of the kite. Following from the obtained parameters, the rotors, motors and batteries can be sized, which is done in chapter 7. The performed structural analysis is elaborated upon in chapter 8, followed by verification and validation of the used models in chapter 9. A sensitivity analysis is done in chapter 10 regarding centre of gravity and scalability. Next, the development projections are described, starting with a financial analysis in chapter 11. The approach towards sustainability is outlined in chapter 12, which ensures the design leaves the smallest impact as possible on the environment. Finally, the project design and development logic are elaborated upon in chapter 13. The report is concluded with a requirements compliance matrix in chapter 14.

2 | Concept development

This chapter is a summary of the earlier baseline and mid-term report, for further elaboration read [20] and [15] respectively. The first section is about the boundaries of the project on the basis of the main requirements. Section 2.2 describes how the linear rail, lighter-than-air, multi-copter and vertical take-off and landing concepts were developed, respectively. Different possibilities were considered and eliminated using a RAMS and Technology Readiness Level (TRL) analysis. Section 2.3 elaborates on the method on how these four concepts are compared to each other and concludes with the final concept which is worked out in the remainder of this report.

2.1 Requirements & constraints

This section will briefly discuss the requirements the design has to full fill. The full list of requirements is specified in the baseline report [20]. The compliance with the list of requirements is presented and discussed in chapter 14 of this report. Any requirement that has not been met is elaborated upon in the associated feasibility analysis. Below, the most driving requirements are shown.

1.1 - The system shall conform to the 2014 DSE AWE system. As a basis, the rigid wing AWE system designed by [19] is taken. This means that the designed launching and landing system must be applicable to this design. The AWE system may be altered if needed, but it should be noted that this will consume precious time.

1.1.1 - The system shall launch an aircraft with a mass no less than 42 kg. Part of the applicability to the 2014 DSE AWE system, the system is to launch a craft with a mass of at least 42 kg.

1.1.2 - The system shall add no more than 10 kg to the airborne clean aircraft mass. This requirement directly limits the mass of any components that are to be added to the AWE system.

1.1.3 - The system shall induce a drag addition of no more than 10 % of the clean aircraft drag. Similar to requirement 1.1.2, this limits the addition of components to the kite.

2.1 - The system shall conform to sustainability constraints. As the exercise concerns a design in the field of renewable energy, sustainability is an important factor in the design.

2.4.1 - The system shall be designed by a 10 FTE team within 11 weeks. With a relatively short time for the project, a major challenge is to utilise the team's time in such a way that a complete design of sufficient quality can be reached.

2.5.3 - The system shall use no more ground space than a circle with a 10 m radius. The ground space requirement limits the size of any ground-based features of the system.

2.5.5 - The system shall be scalable to a 2 MW AWE system. It is suggested that a larger aircraft is more efficient. Therefore, the scalability of the chosen design has to be shown.

2.2 Concept analysis

Linear rail

The linear rail concept was divided into four different phases: launching, climbing, descending and landing. For launching the choice was made to further analyse the catapult launch. To assist this type of launch, horizontal propellers are used during climb. Descending will be performed with a gliding flight after which touchdown is done with electromagnets.

Lighter-than-air

Since the lighter-than-air concept was still very vague multiple possibilities were still taken to the trade-off, as it was not yet possible to eliminate enough subconcepts to come up with one concept after the RAMS and TRL analysis. The lighter-than-air concept was divided into three different categories: launching, landing and retrieval. For launch, a kitoon was selected filled with either a hybrid mixture of air and helium or only helium. Landing and retrieval is done by catching the kite with the kitoon after which it is safely reeled in with the tether of the kitoon.

Multi-copter

For the multi-copter concept two concepts are considered for the trade-off. The first concept is with a pulley, belonging to the multi-copter, attached to the tether of the kite. By flying up the multi-copter and stalling the kite it will hang under the multi-copter which can land the kite safely. The second concept is a multi-copter which flies independently to the kite to pick it up with electromagnets and bring it into launch or land position.

Vertical take-off and landing

The VTOL concept is a straightforward and proven concept. However, for the location of the rotors multiple options were possible. After some calculations it was concluded that two options were still viable. A configuration with rotors attached to the end of the wings (wingtips) and a configuration with winglets and rotors attached on top of these winglets.

2.3 Trade-off

To come up with one final concept a trade-off had to be made of the four concepts that were still left. The criteria for this trade-off are chosen by analysing parts that contribute to the Levelised Cost Of Energy (LCOE). The LCOE is a way to express the price of energy per kWh produced [€/kWh]. The grading is done on a scale from one to four with the following global meaning (for further elaboration read [15]):

1. Unacceptable
2. Correctable deficiencies
3. Good, meets the requirements
4. Excellent, exceeds the requirements

To determine the weights of the criteria the Analytical Hierarchy Process (AHP) is used [21]. This tool determines the relative importance of the criteria. Each group member had to fill in a table, to score the relative importance, where after the geometrical mean is taken to come up with the final weights.

As can be seen in table 2.1, the Linear rail, Multi-copter and VTOL concept had a similar score. The LTA concept, however, scored significantly lower. Changes in either the weights or the scores on a criterion did not change the total scores by much. Therefore, the final trade-off had been decided in a group vote. Out of

Table 2.1: Trade-off of the four concepts

	Linear rail	Lighter-than-air	Multi-copter	VTOL
Aerodynamics (29%)	2	2	3	2
Mass (9%)	3	3	3	1
Launch energy (7%)	3	4	2	2
Land energy (7%)	3	4	2	3
Maintenance interval (7%)	4	3	4	4
Service costs (7%)	2	1	3	3
Chance of failure (14%)	3	2	3	4
Cost of failure (8%)	3	1	3	4
Man hour costs (3%)	3	2	2	4
Kite attachment costs (3%)	4	1	1	3
Ground station costs (4%)	2	1	4	4
Total	26%	21%	27%	26%

the final three competing concepts, each group member had indicated a first and second preference. A first preference was worth two points, while a second choice was worth one point. This scoring was done without knowledge of the other members' choice. The results of this vote were gathered and are shown in table 2.2. Note that the two scores of 1 for the multi-copter and VTOL concept were discussed and looked into again after which these deficiencies were considered correctable.

Table 2.2: Final concept vote

Concept	Number of first choices	Number of second choices	Total score
Linear rail	4	1	9
Multi-copter	4	1	9
VTOL	2	8	12

From table 2.2, it can be seen that the VTOL concept had a clearly higher score than the linear rail and the multi-copter concept. It can be noted that the VTOL concept had been given the least amount of first choices. However, it is also the only concept that received a vote from every single team member, leading to a higher total score. It was concluded that the VTOL concept was chosen for further evaluation until the final review.

3 | System analysis

In this chapter a functional analysis for the system is performed in sections 3.1 and 3.2. Then the N2 chart for the system is given and explained in 3.3. After that the communication flow diagram and data handling are explained in respectively 3.4 and 3.5. Also a resource allocation is given in section 3.6 followed by an extensive power performance analysis of the system in section 3.7. Finally the technical risk analysis performed using the RAMS method can be found in section 3.8.

3.1 Functional flow block diagram

In appendix A.1, the Functional Flow Block Diagram (FFBD) is shown. Starting at the top left, the first function "Initialise launch system" is found. Following the arrows along the top row, the sequential function flow can be found. For a more detailed functional analysis one has to follow the arrows down. There, one can see a single function broken down in sub-functions. One can see that only initialise launch, launch aircraft, and land aircraft are elaborated upon. The other top-level functions are shown for completeness, but are considered to be outside the scope of this project.

1. **Initialise launch system:** As mentioned, the function "Initialise launch system" describes all the required actions that result in the aircraft and the launch system being ready to perform the launch procedure. The atmospheric and wind conditions will be checked to ensure a safe launch. The data for this will be provided by an external source and then compared to reference data to find out if the conditions are suitable for launch. Then the control surface actuators, as well as the rotors will be checked.
2. **Launch aircraft:** At this point, the actual launch can be performed by the system. First, let propellers rotate at the right angular velocity to start producing lift and let the aircraft climb. To ensure safe climb, the position has to be known at all times, so an autopilot can bring the aircraft to the operational altitude. First, the aircraft will climb vertically to an altitude of 30 m. Then the tail rotor will turn 90 deg into horizontal position to cover horizontal distance as well. Finally, when the desired altitude is reached, the attitude of the aircraft will be altered to 30 deg elevation, which is the correct attitude for transition into nominal flight.
3. **Perform nominal flight:** The nominal flight phase is important for the entire mission and the aircraft itself, but not fully relevant for the launch and landing. The aircraft and its nominal flight have been designed by the 2014 DSE team [19]. However, the VTOL concept results in some very drastic changes to the nominal flight configuration of the aircraft. Therefore, the impact on aerodynamics, stability & control and structures of the kite is analysed. Nevertheless, these are not part of the functions of the aircraft, which explains why they are left out of the FFBD.
4. **Land aircraft:** If a decision is made to abort nominal flight and land the aircraft, the descend manoeuvre is started. Firstly, the nominal flight pattern will be terminated after which the attitude is adjusted. Now, the aircraft is in position to move towards the landing space. The angle of attack is increased, tether is reeled in, and the rotors are mainly used to guide the aircraft towards the ground station. The gliding, descending motion is sustained until the desired position for the final landing phase is reached. At this decision point, it is chosen whether or not the system can carry out the final landing procedure. This is done by transitioning into hovering flight and vertically descend and touch down. Alternatively, the aircraft needs to perform a controlled crash landing on the ground, which inevitably inflicts damage on the aircraft.
5. **Store aircraft:** After a complete standstill is achieved on the ground, the boundaries of the design space are encountered again. The aircraft needs to be removed from the landing site, which is why this function is called "Store aircraft". Several sub-functions may consists of checks to the aircraft and

the system, moving the aircraft and keeping it in a storage unit. If this function is finished, a loop is created to the first function, completing the entire system or a scheduled maintenance is performed. For a detailed overview of the 'Store aircraft' function, further research is required since it is outside the scope of the launching and landing system that is being designed.

6. **Perform scheduled maintenance:** A scheduled maintenance can be carried out when the kite is not operational. This can range from cleaning the aircraft to replacing deteriorated components. This is the only part of the mission which is not automated.

3.2 Functional breakdown

In appendix A.2, the Functional Breakdown Structure (FBS) of the system is shown. It shows hierarchically the functions that the system needs to perform at a relatively high level. The FBS shows a number of functions that are similar to the ones shown in the FFBD in appendix A.1. These are the functions grouped under 'prepare launching', 'perform launching' and 'perform landing'. The storage of the aircraft and the maintenance that needs to be conducted are grouped under 'Conduct operations & logistics' and 'Perform nominal flight' only holds the two main components of nominal flight, as its detailed design is outside the scope of this report.

Furthermore, two other functions are added to the FBS compared to the FFBD. These are functions that are present during the entire mission and, therefore, cannot be put into a functional flow diagram due to their time independence. The first one is 'Communicate within system'; this represents the internal communication needed to control the aircraft and provide stability during its manoeuvres. This is done by managing the control surfaces, which are the key drivers that determine the flight paths of the aircraft. Another aspect which is related to communication within the system is determining whether the aircraft needs to land or not. Sensors have to identify when the conditions are not suitable for operations anymore and communicate this to the autopilot. The autopilot will then start the landing manoeuvre.

The other added function is powering the aircraft. There are four subsystems that need energy to be able to function well and this is provided by the batteries by means of wiring which is present within the aircraft structure. During nominal flight, the tail rotor also generates energy which is used for powering the system while in nominal flight.

3.3 N2 chart

The N2 chart is an analysis tool that represents functional interfaces between the various subsystems. By generating the chart the functional dependencies between subsystems are identified. This is done by specifying what input a certain subsystem needs, and what output is generated by the subsystem. Consequently, the output from one subsystem will be the input to the next subsystem. This analysis is used to design the system and integrate its functions in a way such that they are compatible with each other. The chart is structured as follows: the diagonal in the chart shows the various functions or subsystems, the other blocks are the inputs and outputs. One can read it like this: if one looks at a function, the outputs for the other functions will be listed in rows, whereas the inputs from other functions can be read from the columns. The generated N2 chart for the final design is shown in figure 3.1.

The first functional block is the power system: it receives the power setting from the autopilot and ground station, and it outputs the power to the other subsystems. The next subsystem are the sensors, their output is atmospheric data, attitude, altitude and velocity which the sensors will pass to the autopilot and the communication subsystems. The next block is the propulsion subsystem, it receives the throttle setting from the autopilot. The next functional block contains the control surfaces, they will receive the required deflections from the autopilot, and they will output their actual deflections back to the autopilot as a feedback loop. The next block is the autopilot, which is the main input handling subsystem. The autopilot receives attitude, altitude, velocity, control surface deflections, tether tension and ground station commands from

Table 3.1: N2 chart of the subsystems of the final concept

							→
Power System	Power	Power	Power	Power	Power		
	Sensors			Attitude, Altitude, Velocity, Atm. conditions	Attitude, Altitude, Velocity		
		Propulsion		Thrust			
			Control Surfaces	Actual deflections			
Power Settings		Throttle Settings	Required Deflections	Autopilot			
					Communication	Velocity	Attitude, Altitude, Velocity
				Tether Tension		Winch	
↑ Commands				Commands			Ground station
							←

the other subsystems. Next, it handles the data and sends commands to the various subsystems. The communication subsystem is used to communicate from the aircraft to the ground station, it tells the winch what the velocity of the aircraft is, such that reel-out speed can be determined. The final block is the ground station, which receives the attitude, altitude and velocity information to determine whether landing and descent is performed correctly.

3.4 Communication flow diagram

The communication flow diagram shown in figure 3.1 contains two main parts: the ground station, and the aircraft autopilot. These are the main controllers of the system, and hence they will be handling the various data streams. The ground station will receive data from nearby weather centres, as well as manual controller input. This data will be processed and commands will be sent to the winch (reel-in, reel-out, etc.), and the aircraft autopilot (prepare take-off, adjust attitude, etc.). The autopilot will get input from the ground station, as well as from on-board sensors. The autopilot will perform data processing, for example position, velocity, etc., and send appropriate commands to the propulsion subsystem and actuators. The autopilot also keeps track of the commands it has sent to the propulsion subsystem and control surfaces to be able to know their current settings and deflections. This will be done via the internal feedback loop of the autopilot, which makes the system closed-loop.

3.5 Data handling

Following from the communication flow from figure 3.1, a measure to handle the data needs to be established. The result is shown in a data block diagram, represented in figure 3.2. Here the labelled arrows are present data streams and the blocks are processors or sensors which pass on, modify or generate data. Starting with the ground station, commands can be sent to the kite while sent data from the kite is obtained. This is done using a ODIN-W2 telemetry unit¹, which provides a safe and reliable connection, well within the range between the kite and the ground station. This telemetry unit acts as a transceiver, which passes on data received from either the ground station or the main MCU (Micro controller unit). The selected MCU is the SAM E70², which contains a processor, memory allocation for predefined commands and other data to be stored and a voltage regulator. This processor does not contain a board for the autopilot, for which a different processor is used. This main processor obtains commands from the ground station and provides the current settings of the aircraft. The Pixhawk autopilot³ provides a platform on which the autopilot can be developed. The module comes with a PX4 control board, which contains a separate processor and extra memory. The Pixhawk also contains gyroscopes, barometers and accelerometers, which give the autopilot

¹Retrieved from: <https://www.u-blox.com/en/product/odin-w2-series> [Accessed on 27-06-2017]

²Retrieved from: <http://www.atmel.com/products/microcontrollers/arm/sam-e.aspx> [Accessed on 27-06-2017]

³Retrieved from: <https://pixhawk.org/modules/pixhawk#specifications> [Accessed on 27-06-2017]

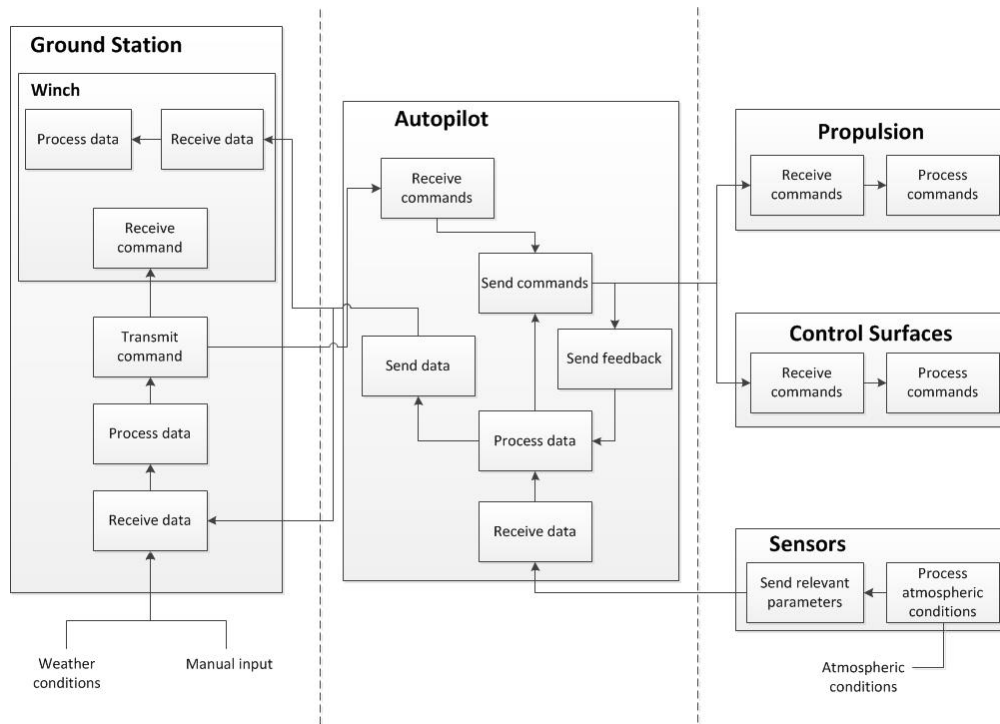


Figure 3.1: Communication flow of the final concept

with the values that it needs. Together with a separate GPS sensor, the autopilot can use the required trajectory to determine the required deflection settings and the throttle settings.

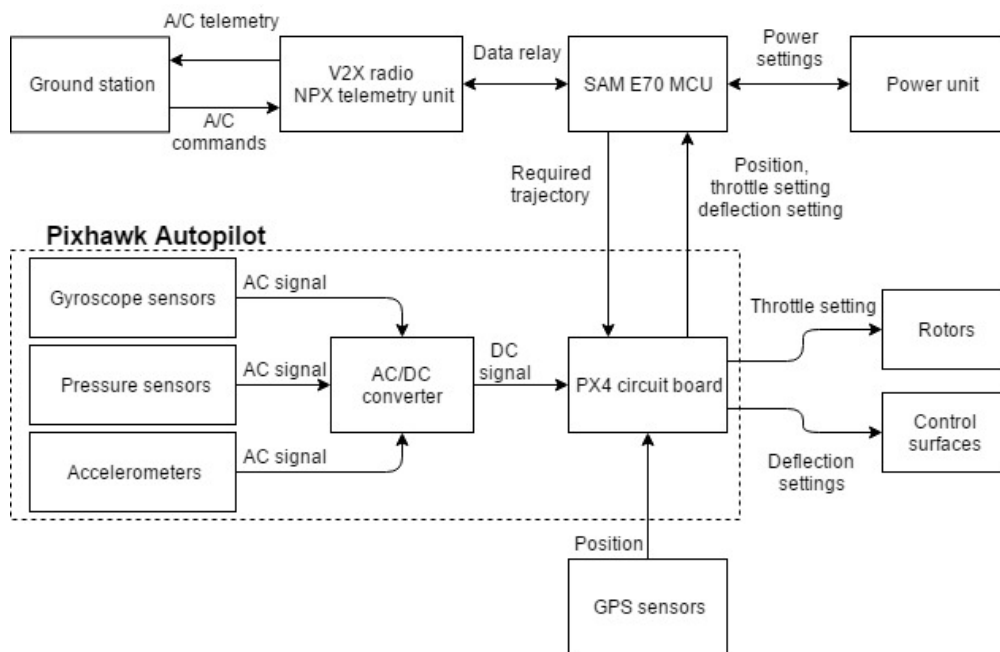


Figure 3.2: Data handling block diagram of the final concept

3.6 Resource allocation

This section provides the resource allocation for the mass budget and power budget. The contingency of the design is taken into account by adding a safety factor to the total mass found and a safety factor for the main contributors of the power budget, namely the motors.

3.6.1 Mass budget allocation

For the estimation of mass and centre of gravity location, two tools are used: a CAD model, created in CATIA, and a spreadsheet. The CAD model is used to make quick and accurate estimations on mass, position of the centre of gravity and the moments of inertia. The spreadsheet is used to quickly check sensitivity of the mass and centre of gravity to certain component's mass or placement, as well as to make an estimation on the weight of coating. Finally, an additional 10% of the expected mass is taken into account for the final estimated mass, to allow for contingency. This includes any unforeseen masses, such as bonding and filling pastes used in production which are not modelled, masses that are higher than expected and production errors.

In the CAD model, the standard density of aluminium of 2700 kg/m^3 are used for all aluminium components. Carbon fibre skin parts use a density of 1400 kg/m^3 , while the stiffened panels are allocated a density of 52 kg/m^3 . The breakup for the densities of the carbon fibre skin and stiffened panels is shown in tables 3.2a and 3.2b. For coating, dry film weights for AkzoNobel Aerodur primer [2] and Eclipse topcoat [3] are being used as reference, for dry film thicknesses of $20 \text{ }\mu\text{m}$ and $70 \text{ }\mu\text{m}$, respectively, resulting in a total coating weight of 146 g/m^2 . This will be applied to the surfaces of the wings, winglets, body, tail boom and tail surfaces.

Table 3.2: Calculation of composite densities

(a) Carbon fibre density calculation		(b) Stiffened panel density calculation	
Element	Value	Element	Value
Dry fibre weight	200 [g/m ²]	Foam density	32 [kg/m ³]
Number of layers	2 [-]	Resin absorption	125 [g/m ²]
Thickness per layer	0.2 [mm]	Panel thickness	11 [mm]
Fibre volume content	0.65 [-]	Total weight per area	570 [g/m ²]
Resin density	1.15 [kg/m ³]	Total density	51.8 [kg/m ³]
Total weight	561 [g/m ²]		
Total density	1402.5 [kg/m ³]		

The resulting mass breakdown is shown in table 3.3, along with the contribution to the total weight in percentage. In this table, the components are grouped for ease of reading, a complete breakdown is presented in appendix F. The category 'Structure' includes all load carrying components, namely the wing spars, ribs, top panels, tail boom and empennage structure. Note that in table 3.3 the masses are presented for entire sections, i.e. 'skins' includes both the left and right wing's skins, while the masses shown in table F.1 are for single parts, multiplied by two if a symmetric part exists.

A topic of great interest in the mass breakdown is the centre of gravity location. For static stability in forward flight, this must be located in front of the aerodynamic neutral point. For control and stability in hover mode, the centre of gravity must be located between the main rotors and tail rotor, to prevent the need for negative lift from the tail rotor. With the neutral point at 602 mm or 0.47 x/c from the wing's leading edge at the root and the main rotors at 500 mm or 0.39 x/c from the leading edge, this leaves a small range for the centre of gravity location. In the current design, the centre of gravity is located at 577 mm or 0.45 x/c.

Table 3.3: Mass budget

Element	Mass [kg]	Percent of mass [%]
Wing and body skins	18.06	26
Batteries	18.00	26
Structure	11.67	17
VTOL motors/rotors	8.00	12
Electronics	6.57	10
Coating	5.22	8
Control surfaces and mounts	0.93	1
Total mass	68.46	100
Design mass	75.30	110

In table F.1, all components' coordinate in x are shown in [mm], as well as the associated moment around the neutral point in [Nm]. The mass of the empennage, tail rotor assembly, and tail boom shift the centre of gravity back significantly, due their the large arm. All components in the main wing are located close to the neutral point. To get the centre of gravity in front of the neutral point, a forward protruding, lifting body in the centre of wing is added. This body is used give an offset to the arm of the batteries and the flight control computers, which counteracts the contributions of the aft masses. The body is constructed by inserting the same airfoil as the main wing in the middle with a larger chord length, whilst keeping the trailing edge at the same location.

3.6.2 Power budget allocation

For the power budget allocation all the components that use power in the kite are taken into account. Besides the electric motors for the rotor, these components are sensors to measure the attitude, altitude and location of the kite as well as actuators to control the attitude and flight trajectory. Also communication between the kite and ground station is needed and for that transmitters and receivers are used. The values of the components are based on research of the available market and recommended by KitePower in the DSE2014 report [19]. The power budget allocation can be found in table 3.4. The main components are, as expected, the motors needed to perform the VTOL. The rest of the components are marginal compared to those values.

Table 3.4: Power budget

Component	Power [W]	Percent of power [%]
Attitude sensors	1.6	0.01
Wireless transceiver	0.02	0.00
GPS sensors	0.27	0.00
Control actuators	68	0.21
Total nominal flight power	69.89	0.22
Main motors	29,400	92.54
Tail motor	2,300	7.24
Total on board power	31,770	100
Total on board design power	34,947	110

3.7 Power performance analysis

In this section both the power output generated during the traction phase as the power input needed during the reel-in phase are calculated. These two powers are then combined to find the average generated power per cycle. To do this first an estimation of the wind profile is made along with a density profile.

3.7.1 Wind velocity profile

To be able to find the output power during traction and the input power during reel-in of the generator, the wind velocity at different altitudes should be modelled. The wind velocity encountered by the kite tends to increase in velocity when the kite gains altitude, which should be taken into account while estimating the generated and used power.

While performing a literature study, it was found that the altitude in which the kite operates during nominal flight is between 100 m and 350 m, which is considered to be in the boundary layer of the wind. Because of the surface of the Earth, a net loss of energy to the ground occurs within this boundary layer [19] [22]. Because of this loss of energy, the wind velocity profile is harder to predict within than outside the boundary layer. However, equation 3.1, which is based on empirical data, has been set up to approximate the wind velocity profile.

$$V_w(h) = V_{w,\text{ref}} \left(\frac{h}{h_{\text{ref}}} \right)^\alpha \quad (3.1)$$

In equation 3.1 $V_{w,\text{ref}}$ is the wind velocity at the reference altitude h_{ref} , α is the friction coefficient and has an average value of 0.14 for open grass fields. [22] V_w is the wind velocity on a certain altitude h . Note that this equation is only valid for altitudes lower than 500 m. The reference values are as an average set to $V_{w,\text{ref}} = 5$ m/s and $h_{\text{ref}} = 6$ m [19]. Using the values above with an altitude range of $0 \leq h \leq 500$ m, the wind velocity profile will look like in figure 3.3a.

3.7.2 Atmospheric density profile

The power generated and consumed by the generator also depends on the density of the air, through which the kite is. The density of air is calculated using the International Standard Atmosphere (ISA) [5]. The density at different altitudes ($0 \leq h \leq 500$ m) is determined using equations 3.2, 3.3 and 3.4.

$$p = p_0 \left(1 - \frac{\alpha h}{T_0} \right)^{\frac{Mg_0}{R\alpha}} \quad (3.2)$$

$$T = T_0 - \alpha h \quad (3.3)$$

$$\rho = \frac{pM}{RT} \quad (3.4)$$

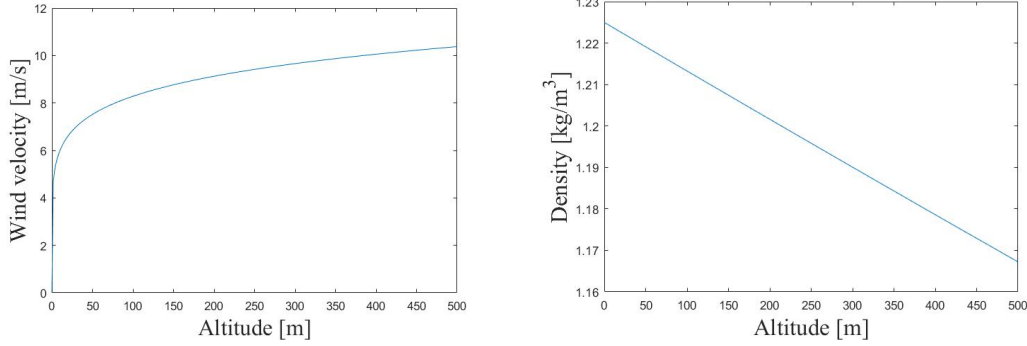
Except for the altitude h , the pressure p , the temperature T and the density ρ , all the parameters are constants and their value can be found in table 3.5. Using equations 3.3-3.4, the atmospheric density profile as a function of altitude can be created, which is shown in figure 3.3b.

3.7.3 Power output

The power output uses the previous determined wind velocity and atmospheric density profiles to calculate the power output of the system. The profiles are relevant because they give different power outputs per altitude. The numerical method, described in chapter 14 of the Airborne Wind Energy book [22], is used to determine the power output per altitude $P_{\text{out},i}$, where i denotes the altitude step number. The assumptions for the power output model are listed below.

Table 3.5: Standard values of the ISA method

Parameter	Definition	Value
p_0	Standard atmospheric pressure on sea level	101325 [N/m ²]
T_0	Standard temperature on sea level	288.15 [K]
κ	Temperature lapse rate	0.0065 [K/m]
g_0	Gravitational acceleration	9.81 [m/s ²]
M	Molar mass of air	0.0289644 [kg/mol]
R	Universal gas constant	8.31447 [JK/mol]



(a) Wind velocity versus altitude with $V_{w,ref} = 5$ m/s and $h_{ref} = 6$ m (b) Atmospheric density versus altitude with standard ISA values

Figure 3.3: The velocity profile is shown left and the atmospheric density profile is shown right

- The tether is assumed to be a straight line between the kite and the winch. This assumption increases the power output slightly.
- The mass of the kite and the tether is neglected. This assumption will increase the power output slightly.
- The kite is assumed to fly at a constant elevation angle of $\vartheta = 30$ deg. This assumption can both increase and decrease the power output. If the real elevation angle is lower than 30 deg this assumption results in an underestimation of the power output, if the real elevation angle is higher than 30 deg this assumption results in an overestimation of the power output.
- The dynamics of the kite and of the drum on the ground station are neglected. In reality the drum needs to respond fast, for example in the case of gusts, which results in a loss of efficiency. This assumption will thus increase the power output.
- To compensate the non-ideal real-world behaviour, crest factors are used as well as a dead time of 10 seconds without any power generation between reel-out and reel-in.

The first performed step in the model, is the determination of the tether drag coefficient C_{D_t} with use of equation 3.5. In equation 3.5, r is the tether length, d_t is the tether diameter and C_{d_t} is the circular tether drag coefficient. C_{D_t} is then added to the drag coefficient of the kite C_{D_k} to obtain the drag coefficient of the whole system C_D as done in equation 3.6. Because only the upper end of the tether is moving with the speed of the kite and the lower end is not moving at all, an approximation of the average effective tether drag should be made. Therefore, in equation 3.5, about 31% of the drag that the tether would have if the full length of the tether would move with the speed of the kite, is used. [22]

$$C_{D_t} \approx 0.31 \frac{rd_t}{S_{proj}} C_{d_t} \quad (3.5)$$

$$C_D = C_{D_k} + C_{D_t} \quad (3.6)$$

Apart from the drag coefficient, also the apparent velocity during reel-out per altitude $V_{a,o,i}$ should be determined, which is done using equation 3.7. In this equation 3.7 ϑ is the angle of tether with respect to the ground and is set to 30 deg. φ is the azimuth angle and is set to 0 deg. To achieve a maximum $V_{a,o,i}$, the C_L/C_D should be maximum, which is achieved by using the highest angle of attack $\alpha = 18$ deg. The normalised reel-out velocity is called f_{out} and is defined as in equation 3.8, where $V_{r,out,i}$ is the reel-out velocity of the tether per altitude. Ideally, the kite would fly with $\vartheta = 0$ deg, which results in a full crosswind flight. However, this is unfeasible and thus a ϑ of 30 deg is chosen. This results in a maximum tether length of $r = 700$ m and an acceptable cosine loss.

$$V_{a,o,i} = (\cos(\vartheta) \cos(\varphi) - f_{out}) V_{w,i} \sqrt{1 + \left(\frac{C_L}{C_D}\right)^2} \quad (3.7)$$

$$f_{out} = \frac{V_{r,out,i}}{V_{w,i}} \quad (3.8)$$

Now, the only thing that needs to be calculated to find the final power output per altitude is the maximum tether force per altitude $F_{t,max,i}$, which is defined in equation 3.9.

$$F_{t,max,i} = \frac{1}{2} \rho V_{a,o,i}^2 S_{proj} C_D \sqrt{1 + \left(\frac{C_L}{C_D}\right)^2} \quad (3.9)$$

$$P_{out,i} = \frac{1}{CF} F_{t,max,i} V_{w,i} f_{out} \quad (3.10)$$

The final equation of the power output per altitude can be found in equation 3.10. Power, by definition is force times velocity. The maximum tether force is corrected by using a crest factor CF, because the kite is not always flying in the centre of the wind window. In the case of nominal flight, Argatov's value is used and therefore $CF = 1.11$. [22]

The limiting factor for this model is $V_{a,o,i}$, since it influences the aerodynamic forces generated, as well as the tether force. These forces in turn influence the loads on the structure. Since the structure is designed to be able to handle loads generated with a maximum apparent velocity of $V_{a,o,i} = 35$ m/s. $V_{a,o,i} = 35$ m/s results in a more or less constant tether force of 20 kN, which is the limiting factor of the structure, for reference wind velocities higher than $V_{w,ref} = 5.5$ m/s at $h_{ref} = 10$ m. This means that the two remaining variables, $V_{w,i}$ and f_{out} , determine $P_{out,i}$. However, as $V_{w,i}$ depends on $V_{w,ref}$, the two final variable inputs of the model are $V_{w,ref}$ and f_{out} .

To determine the optimum f_{out} for every $V_{w,ref}$, the input power P_{in} needs to be calculated as well. When the input power is known, the average cycle power per wind condition can be calculated. How P_{in} is found is explained in subsection 3.7.4.

3.7.4 Power input

The determination of the reel-in power P_{in} is more or less the same as for $P_{out,i}$. However, there is no ideal angle of attack α known yet. To determine the power it takes to reel the kite back in some assumptions are made, that can be found below.

- The flight path of the kite during reel-in has an angle of $\vartheta = 30$ deg with respect to the ground. In reality this flight path changes constantly, the reel-in force will therefore be underestimated.

- The reel-in phase is modelled as a 2D problem where forces in the y-direction of the kite are neglected. This decreases the reel-in force.
- The reel-in phase is a steady state phase, where the velocity is assumed constant and the kite is in force equilibrium. In reality an acceleration is needed, increasing the input power needed.
- The variation of the wind velocity on different altitudes is not taken into account, instead the average wind velocity between $100 \leq h \leq 350$ m is used. This assumption decreases the input power slightly.
- The mass of the tether has been neglected. This assumption increases the reel-in force slightly.

The equations for the apparent velocity during reel-in $V_{r,in}$ and normalised reel-in velocity f_{in} are similar to the ones used for $P_{out,i}$ and can be found in equations 3.11 and 3.12. For this case however, only an average power is calculated instead of the power per altitude. This is due to the uniform wind assumption.

$$V_a = (\cos(\vartheta) \cos(\varphi) + f_{in}) V_{w,avg} \sqrt{1 + \left(\frac{C_L}{C_D}\right)^2} \quad (3.11)$$

$$f_{in} = \frac{V_{r,in}}{V_{w,avg}} \quad (3.12)$$

As mentioned in the assumptions, ϑ is again fixed to 30 deg and φ is again 0 deg. Also mentioned in the assumptions, is that first the average wind velocity $V_{w,avg}$ of the wind profile created with equation 3.1 is calculated. In this case for this equation $100 \leq h \leq 350$ m and a particular $V_{w,ref}$ is used.

Since the optimal α changes with the different possible reel-in velocities $V_{r,in}$ and wind profiles, a range that needs to be investigated is set as $-8 \leq \alpha \leq -4$ deg. Every different α corresponds with a different C_L and C_D which are determined with equations 5.3 and 5.4. The range of reel-in velocities is set as $1 \leq V_{r,in} \leq 40$ m/s, that are used to determine f_{in} in equation 3.12.

Now the apparent velocity V_a can be determined for every combination of $V_{r,in}$ and α . V_a is then implemented in equation 3.13 with the corresponding C_L and C_D . This then gives the reel-in tether force F_r , which is then multiplied with the corresponding $V_{r,in}$ to find P_{in} as in equation 3.14. The limiting factor for P_{in} is the force the tail can handle, which is 2000 N.

$$F_r = \frac{1}{2} \rho V_{a,i}^2 S_{proj} C_D \sqrt{1 + \left(\frac{C_L}{C_D}\right)^2} \quad (3.13)$$

$$P_{in} = F_r V_{r,in} \quad (3.14)$$

The P_{in} that is now found can be used in combination with the multiple $P_{out,i}$ found in subsection 3.7.3 to determine the average power per cycle P_{cycle} . Note once again that P_{in} is the average reel-in power while $P_{out,i}$ is the reel-out power per altitude. The method to find P_{cycle} and the corresponding results are discussed in subsection 3.7.5.

3.7.5 Average cycle power

The most interesting part of the power model, is to obtain the optimised average power per cycle P_{cycle} . P_{cycle} is partly depended on the previously calculated P_{in} and $P_{out,i}$. All the relevant formulas used to find the average power per cycle are given in equations 3.15-3.20 and will be addressed one by one.

$$P_{\text{cycle}} = \frac{E_{\text{out}} - E_{\text{in}}}{t_{\text{out}} + t_{\text{in}} + t_{\text{trans}}} \quad (3.15)$$

$$E_{\text{out}} = \sum_{i=1}^n P_{\text{out},i} \Delta t_{\text{out},i} \quad (3.16)$$

$$\Delta t_{\text{out},i} = \frac{\Delta r}{V_{r,\text{out},i}} \quad (3.17)$$

$$t_{\text{out}} = \sum_{i=1}^n \Delta t_{\text{out},i} \quad (3.18)$$

$$E_{\text{in}} = P_{\text{in}} t_{\text{in}} \quad (3.19)$$

$$t_{\text{in}} = \frac{r}{V_{r,\text{in}}} \quad (3.20)$$

The main equation is 3.15 where E_{out} and E_{in} are the generated and consumed energy respectively. E_{out} is defined as in equation 3.16 where the output power per altitude $P_{\text{out},i}$ is multiplied by the corresponding time step $\Delta t_{\text{out},i}$. This time step in turn is determined with equation 3.17 where Δr is the tether length step corresponding to the altitude steps of the wind profile. The total reel-out time t_{out} can be calculated by summing up all the different time steps.

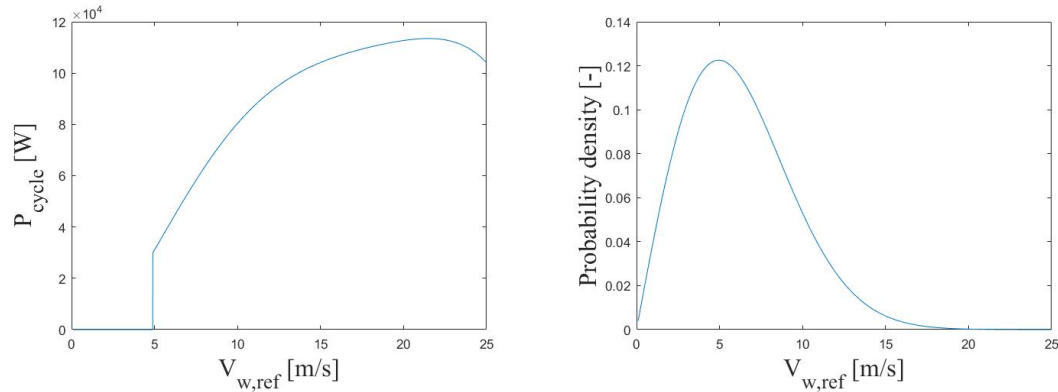
E_{in} is defined as in equation 3.19 which is just the average reel-in power P_{in} multiplied by the total reel-in time t_{in} . The reel-in time is defined in equation 3.20 and is simply the tether length r divided by the reel-in velocity $V_{r,\text{in}}$.

The P_{cycle} can be calculated with as input $V_{w,\text{ref}}$, $V_{r,\text{in}}$, α and f_{out} . The model will, for every $V_{w,\text{ref}}$ find a combination of $V_{r,\text{in}}$, α and f_{out} for which the P_{cycle} is maximised. The array of reference wind velocities at $h_{\text{ref}} = 10$ m that is used ranges from $0 \leq V_{w,\text{ref}} \leq 25$. This gives the result as in figure 3.4a which shows the average power per cycle for every reference wind velocity and figure 3.4b shows the probability density graph of the reference wind velocities. The reason why until $V_{w,\text{ref}} = 5$ m/s the average cycle power is zero is because that is the cut-in velocity. The optimum is found at $V_{w,\text{ref}} = 20$ m/s and has a value of $P_{\text{cycle}} = 112$ kW, which is referred to as the rated power. The reason why there is an optimum on $V_{w,\text{ref}} = 20$ m/s and not on a higher reference velocity is that the reel-out velocity keeps increasing while the reel-in velocity decreases, to not exceed the apparent velocity that results in the critical loads for the wingbox and tail. This results in shorter reel-out times and longer reel-in times, which in turn results in a decrease in P_{cycle} if the reference velocity is higher than $V_{w,\text{ref}} = 20$ m/s.

Table 3.6: Summary of the power en energy produced

Parameter	Value
Rated cycle power	116 [kW]
Average cycle power	43 [kW]
Annual energy produced	248 [MWh]
Capacity factor	38[%]

However, more interesting is the P_{cycle} at the reference wind velocity that occurs most often. To get an idea of how often certain reference wind velocities occur, a probability density function is created using a Weibull distribution, based on data from Den Helder, which can be found in figure 3.4b. [10] It was found that the most probable reference wind velocity is $V_{w,\text{ref}} = 6$ m/s, which results in $P_{\text{cycle}} = 43$ kW. The annual energy can now be determined, using the time it operates yearly. If it is assumed that the kite will operate 75% of the time. The energy that is annually produced is then 248,000 kWh. This energy production corresponds with a capacity factor of 38%. A summary of the most important parameters and values can be found in table 3.6.



(a) The average power per cycle curve using a reference altitude of $h_{\text{ref}} = 10$ m (b) The probability density function of the reference wind velocity based on data for Den Helder [10] with a reference altitude of $h_{\text{ref}} = 10$ m

Figure 3.4: These graphs show the results of the power model

3.8 Technical risk analysis

In the midterm report a trade-off between the different concepts 2.2 was done. The different concepts were graded based on their risk performance. A risks map for each concept was created and used as an estimation for the possible impact of risks. The finally chosen VTOL concept outperformed the other concepts based on safety. To analyse the risks of the VTOL concept in the concept was analysed using the RAMS principle addressing: reliability, availability, maintainability and safety.

Reliability

Since the airborne wind energy field is still an upcoming industry, little data is available to perform a quantitative reliability analysis. Therefore, a qualitative analysis in the form of a fault tree analysis is established in order to map possible risks (see appendix B). As shown in table 3.8 all risks have low probability of occurrence which is also an aspect why this concept is chosen. To design a commercial viable product it needs to be robust and reliable.

Availability

The AWE system has three steady state modes:

- Grounded
- Nominal flight
- Parking mode

To define the availability of the system the percentage nominal flight must be specified since this is the only mode where energy is produced. The other two modes, grounded and parking mode, are initialised when there is no wind for a long or short time respectively. The grounded mode is also initialised when maintenance needs to be performed. The percentage nominal flight is calculated to be 75% as explained in section 3.7.5.

Maintainability

The maintenance interval for the VTOL concept is based on the replacement or turn around interval of the tether as this is the most critical part. As shown in table 8.2a the interval for replacing the tether will be six months if it is chosen to turn around the tether after three months. The maintenance interval is therefore three months. There will be aimed for planning the maintenance during bad wind conditions to minimise the downtime of the system. Furthermore the system does not need any additional scheduled maintenance so general checks on the kite can be performed while changing the tether.

Safety

The OPRs of table 3.7 are mapped in 3.8. This table clearly shows the reliability and robustness of this concept. Most of the risks are negligible and have a very low probability of happening. OPR-8 is the only risk with catastrophic consequences, bird impact will destroy the rotors and structure of the kite. Since the probability that this failure occurs is rare and hard to mitigate it is chosen to neglect. Further data needs to be harvested when real systems are deployed.

Table 3.7: List of technical risks

ID	Risk statement
OPR-01	Tether fails during operation.
OPR-02	Approach manoeuvre failure.
OPR-03	Launch manoeuvre failure.
OPR-04	Structural failure of the kite.
OPR-05	Propulsion failure.
OPR-06	Communication is lost between the ground station and the kite.
OPR-07	Winch failure during operation.
OPR-08	System failure due to a bird strike.
OPR-09	System return of investment are lower then expected.

Table 3.8: Risk map showing the risk from table 3.7 for the VTOL concept

Probability ↑	Likely				
	Possible				
	Unlikely	OPR-06 OPR-07	OPR-01	OPR-05 OPR-09	
	Rare	OPR-02 OPR-03		OPR-04	OPR-08
		Negligible	Marginal	Critical	Catastrophic
		Impact →			

To analyse the risks in more detail a fault tree analysis was done. This tree is shown in appendix B. The fault tree was created top-down starting with in-flight shutdown, the most general mode of failure. One level down an or-gate connects three failures to in-flight shutdown, these three could all individually cause shutdown. The fault tree shows that tether breakage can occur without any preceding failure, therefore this is an important failure that should be prevented. Maintenance protocols should account for this.

Propulsion shutdown only happens when the winch and rotors fail at the same time. When only one of the two fails, the kite can still be accelerated and therefore stay airborne. Rotor failure can be caused by battery failure, motor failure or rotor breakage. Furthermore wire failure, caused by short-circuit or breakage, can result in rotor failure too.

Winch failure without rotor failure could also cause direct in-flight shutdown. Winch failure can originate from either hardware or software failure.

The final failure that could cause in-flight shutdown is failure of the autopilot. The autopilot could fail due to sensor failure, software failure or wire failure. Wire failure can again occur due to short-circuit or breakage.

Risk mitigation

After determining and analysing the risks, methods for risk mitigation were identified. Risk mitigation was done to limit the probability and the impact of a risk. During the mitigation the focus was on OPR-01, OPR-05 and OPR-09 as the probability and impact of these risks were most harmful to the system. The most important way of limiting the chance of occurrence of the risks involving system failure (OPR-01 to OPR-08) is maintenance. During the periodic maintenance, inspection of the full kite will take place. The aim of this inspection is to detect wear and decrease the probability of unexpected failure. The second measure to lower the probability of system failure was taken during the design process. This was done by using design factors for all parts. The design factors increase the lifespan of parts and ensure that characteristics are as intended even though mistakes could be made during the analysis. The most critical risk that is possible to mitigate using design factors was OPR-01, a bigger tether diameter lowered the possibility of tether breakage to a minimum.

On top of limiting the probability of risks, the impact of risks was limited. To limit the effect of OPR-01 the kite will be crash landed after performing a gliding flight. Considering OPR-5 redundancy is hard to implement because this will contribute to losses in nominal flight. Therefore a flight manoeuvre, a controlled crash landing, is performed when this failure occurs.

As OPR-08 was estimated to have a rare probability of occurrences it was not taken into account during the design of the system. But if bird strikes prove to occur more often than anticipated, measures need to be taken. A possibility is using similar laser technique systems as are being used at airports.

OPR-09 needed to be split up to mitigate the risks. The system's return on investment depends on multiple inputs as explained in detail in section 11.2. If due to unforeseen events the the amount of systems sold is lower, the system costs are higher or if the energy production is lower the return on investment decreases. To mitigate these risks, design steps were taken. As the amount of systems sold depends on the market's demand and the demand is determined by the price of a system, the system costs are essential for the return on investment and should be limited and estimated precisely. For a precise estimate the unforeseen costs should be minimised a detailed cost breakdown was done to prevent this from happening. During production a close eye on costs will need to be held.

As the annual energy production is mostly determined by wind conditions, mitigation was difficult. The probability of having a year with relative bad wind conditions is low but has an influence on the produced energy. As this is an external risk, no real risk mitigation on the probability could be done. To limit the impact of bad wind conditions, the design is aimed at a large range of flyable wind speeds increasing the availability. After risk mitigation a new risk map was created. This map is shown in figure 3.9

Table 3.9: Risk map showing the risk from table 3.7 for the VTOL concept after risk mitigation

Probability ↑	Likely				
	Possible				
	Unlikely	OPR-06 OPR-07	OPR-09	OPR-05	
	Rare	OPR-02 OPR-03	OPR-01	OPR-04	OPR-08
	Negligible	Marginal	Critical	Catastrophic	
		Impact →			

4 | System interfaces

This chapter will present the final configuration and lay out in section 4.1. Then the electric equipment of both the aircraft and ground station and a schematic representation of the hardware and software in the aircraft and the ground station is shown in section 4.2.

4.1 Configuration & lay-out

This section shows the internal and external structure of the kite. The technical drawing in figure 4.1, shows the isometric, top, side and front view of the kite. For clarity reasons, the dimensions of these views are shown in section 5.2. It can clearly be seen that the tail beam has an angle which causes the horizontal tail to be lifted a bit above the main wing. The relative size of the tail rotor compared to the main rotors is also clearly visible from this figure. It can be seen that the tail rotor is smaller than the main rotors, which is a logical consequence of the lower thrust requirements. Another aspect that becomes clear from the figure is that the tail beam decreases in size while approaching the tail.

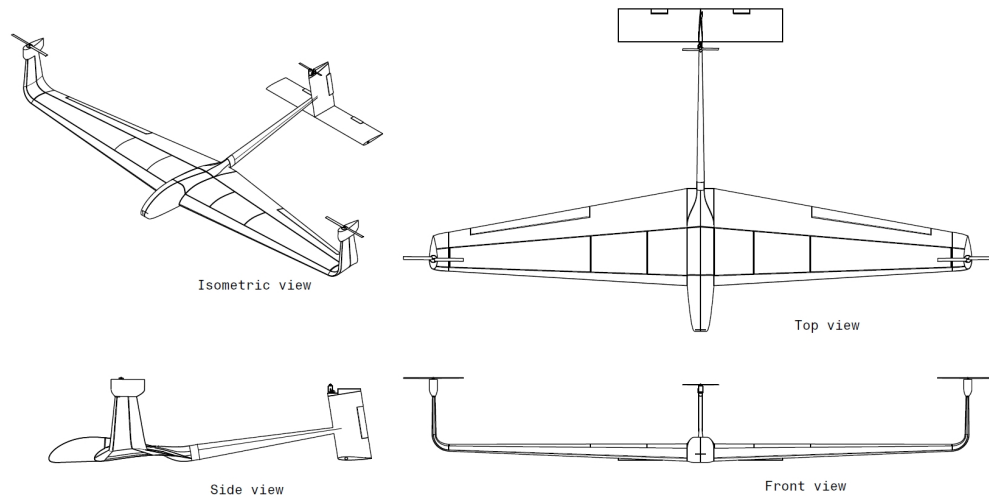


Figure 4.1: Technical drawings of the aircraft

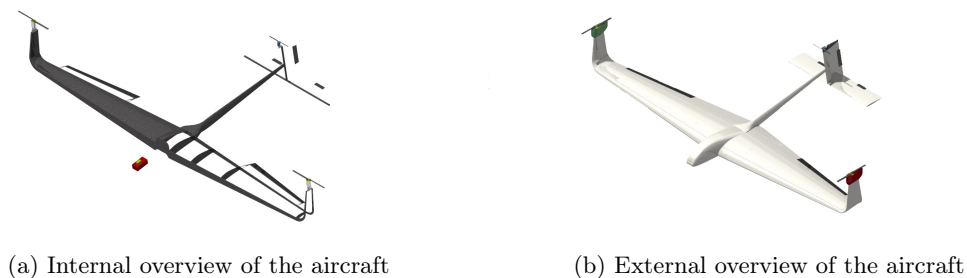


Figure 4.2: Overview of the aircraft

Figures 4.2a and 4.2b show an internal and external overview of the aircraft. The internal overview gives a clear image of the size and location of the control surfaces, which are the flaps, elevators and rudder. It

can also be seen that the batteries are placed all the way in the nose of the aircraft to shift the centre of gravity. Another aspect that can be noticed is the placement and amount of ribs. The two ribs in the middle are there to carry the loads of the tail beam. All the way at the wing tip there is a less clearly visible rib present that closes the wing box and connects to the motor. The three ribs on either side of the ribs in the middle are there to prevent the skin from buckling. The external overview gives an overall picture of what the aircraft is going to look like. For the electrical internal components of the kite is referred to sections 3.4, 3.5 and 4.2.

4.2 Electric systems

The electric system consists of the electronics in the kite, as in figure 4.3, and the electronics in the ground station, as in figure 4.4. The kite has as main power source the primary battery, these batteries only provide power to the three motors. The secondary battery provides power to all the other systems in the kite amongst them the actuators, all the sensors and communication systems. The tail motor receives power from the primary battery but in power generation mode it only provides power to the secondary battery. Next to the power lines there are also data lines which are all connected to the processor. The data lines provide the processor with information from the sensors and enables the autopilot to control the kite via the actuators. The batteries are also connected to the processor via the battery management systems, they provide info on the health of the batteries and when the secondary battery needs to be charged. The power lines are indicated as red bold lines while the data lines are black dotted lines.

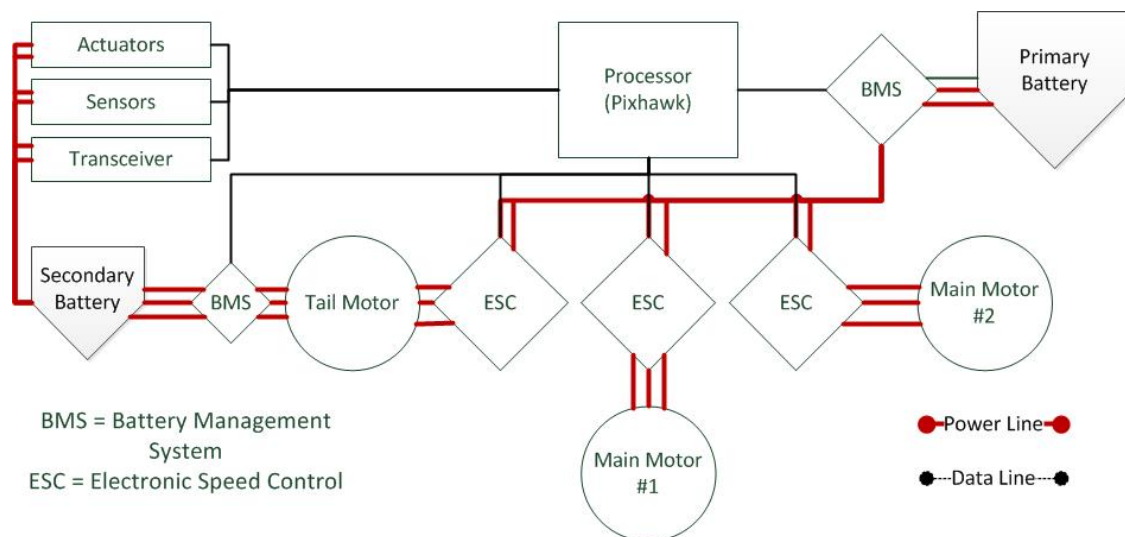


Figure 4.3: Electric diagram of the kite

The ground station has within the electric system analysis two main functions: transmit the generated power to the grid and provide the kite with all the information and power that it needs to function. The generated power has to be transformed to the right voltage and frequency before it can be transmitted to the grid therefore there is a transformer between the generator and the grid connection.

The generator also provides power when the kite needs to be recharged when it is not airborne. Since the energy from the generator is AC and batteries need to be charged using DC there is a AC to DC converter or "rectifier" which will provide DC power to the battery charger when necessary. The remaining ground station electronics are mostly related to control of the ground station itself and communication and control of the kite. This is done via a computer which is connected to a transceiver. The battery provides power to the computer but can also be used as storage when the unit is used off the grid.

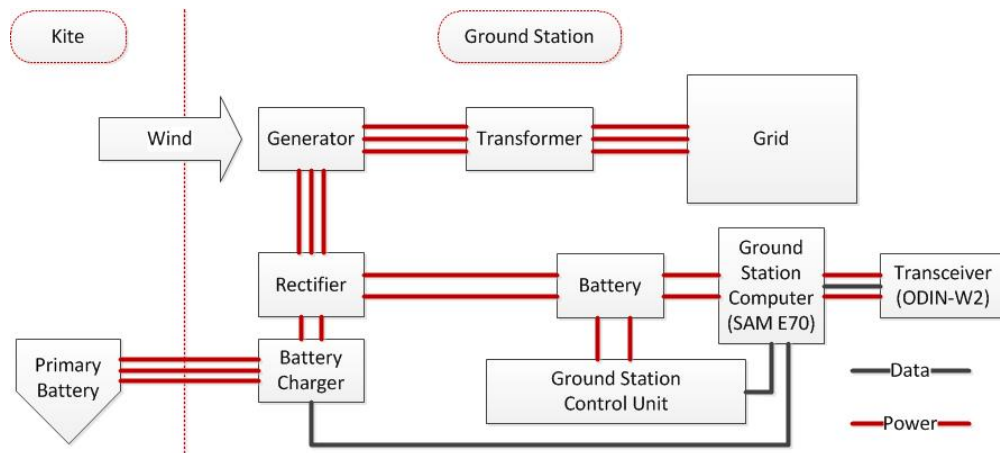


Figure 4.4: Electric diagram of the ground station

Following from the electrical diagrams, the hardware interfaces can be set up. Figure 4.5 gives a basic idea of the hardware present in the kite. Figure 4.6 gives a schematic view of the hardware in the ground station.

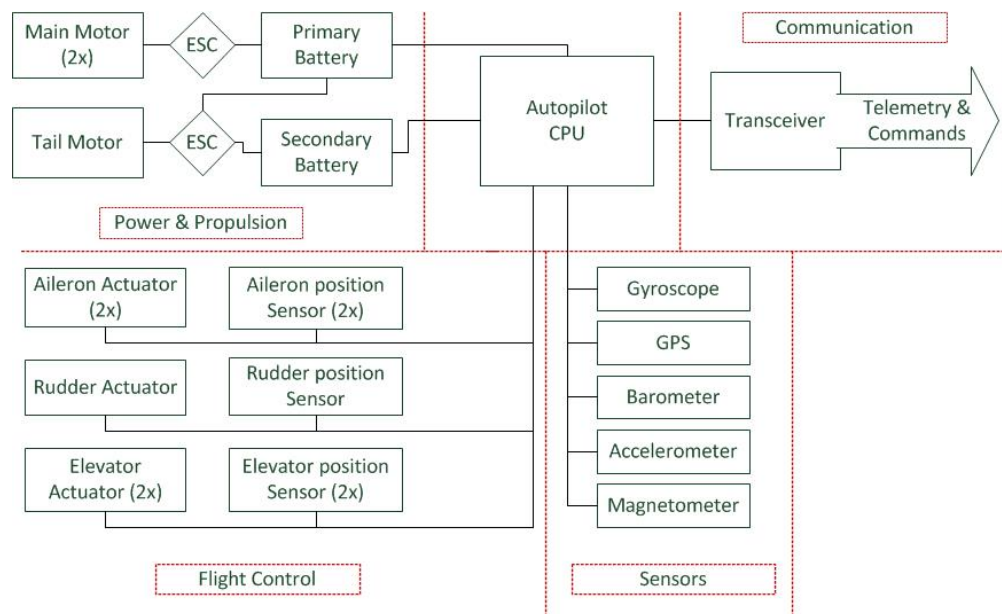


Figure 4.5: Hardware diagram of the kite

Following from the figure 4.5, a software diagram can be created as well. Figure 4.7 presents a schematic view of the inputs and outputs of each hardware component connected to the autopilot CPU, and thus provides an overview of the software that is present on the kite. Figure 4.8 provides a schematic view of the in and outputs of the ground station.

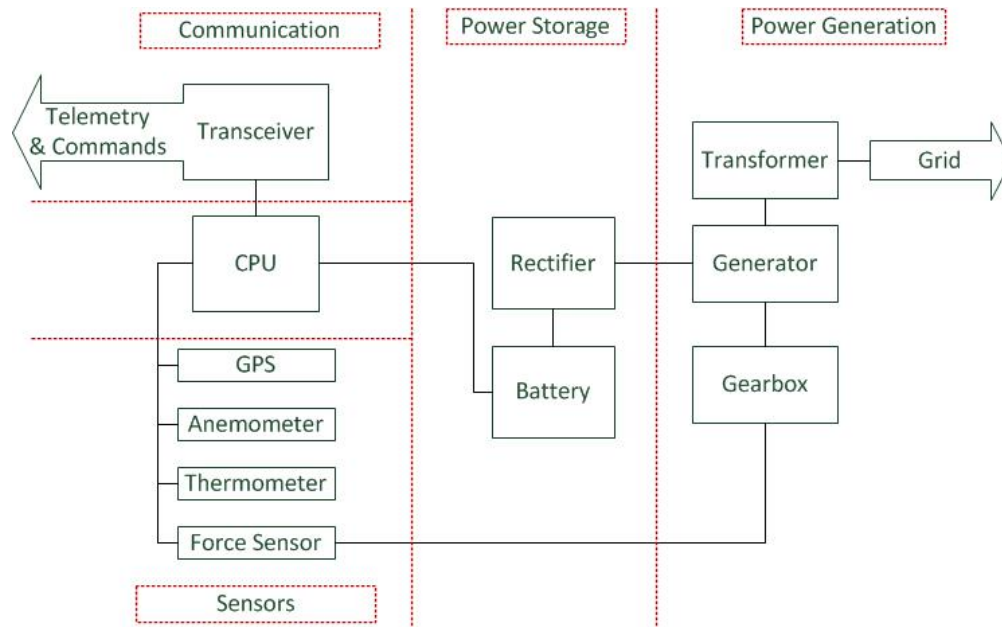


Figure 4.6: Hardware diagram of the ground station

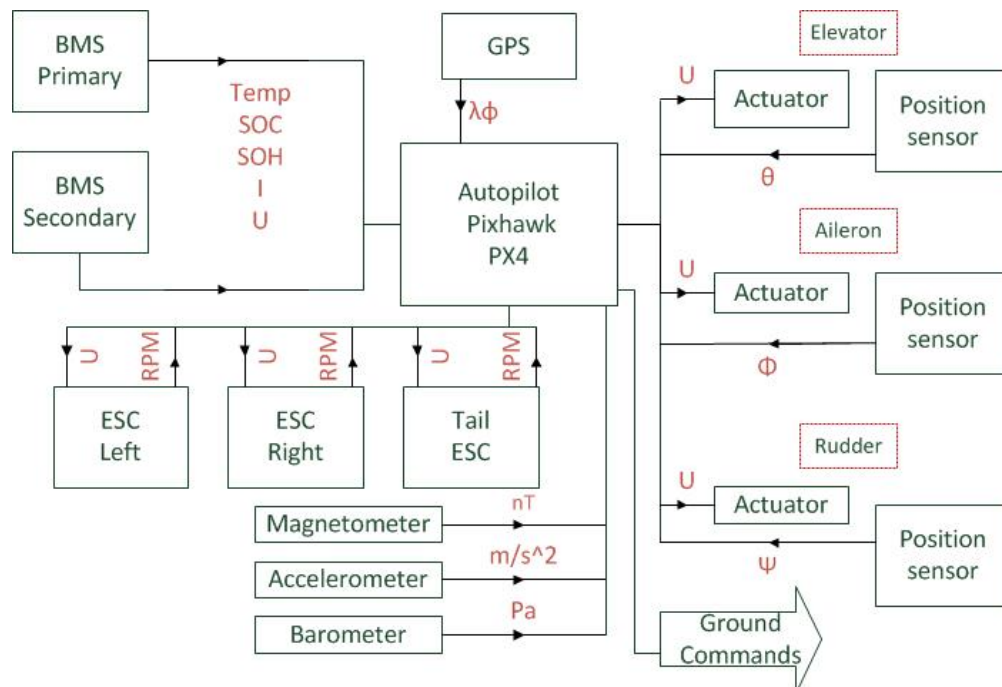


Figure 4.7: Software diagram of the kite

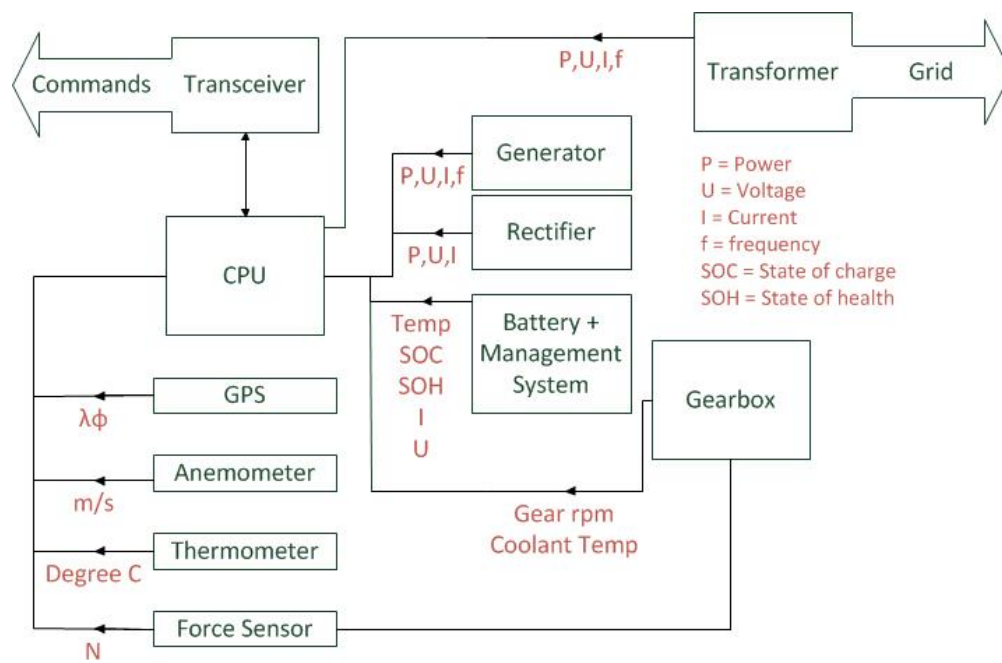


Figure 4.8: Software diagram of the ground station

5 | Aerodynamics

This chapter describes the aerodynamic analysis of the design. The 2014 DSE kite was completely designed for optimum aerodynamic performance, alternations to the design needed to be done to make vertical take-off and landing possible. To model the influences of changes on the aerodynamics the program XFLR5 was used. The same program was used by the 2014 group and analyses the aerodynamics using the lifting line theory, vortex lattice method and 3D Panel Method. During creation of the model limitations in the modelling software were found. Alternative analysis methods were used to estimate the effects that could not be modelled in XFLR5. The general principles of XFLR5 and the alternative analysis methods is described in section 5.1. The final values and outputs of the aerodynamic model are given in section 5.2, the reasoning behind these specifications is given in section 5.3.

5.1 General principles

This section explains the general principles used. Section 5.1.1 explains the principles behind the software. As added drag by the rotors could not be modelled using XFLR5 a separate analysis was performed this is further explained in section 5.1.2. The C_L and C_D the post stall phase are described in section 5.1.3, section 5.1.4 elaborates on the effects of winglets and finally the wing/rotor interaction is discussed in section 5.1.5.

5.1.1 XFLR5

To model the aerodynamics of the kite a systematic approach was taken to ensure that all possible options were analysed. Before elaborating on this approach, the method used by the aerodynamic modelling program XFLR5 will be explained.

XFLR5 uses three methods to analyse the aerodynamics: Prandtl lifting line theory, vortex lattice method and a 3D Panel Method. The Prandtl lifting line theory is a theory that uses the geometric properties of a 3D wing to model the lift distribution [11]. Prandtl theory reasons that a vortex filament with strength Γ experiences a force $L = \rho_\infty V_\infty \Gamma$ based on the Kutta-Joukowski theorem. Solving the integral from wingtip to wingtip for the span-wise circulation variation gives the lift distribution over the wing.

The second method used is the vortex lattice method. This method divides the full wing into 2D panels, in this way the the entire wing is covered by a lattice of horseshoe vortices [11]. The strength of the vortices Γ_n is unknown and varies per control point. Using the Biot-Savart law the normal velocity as a sum of all vortices at each point can be determined.

And third a 3D panel Method is used by XFLR5. This method divides the geometry of the wing into 3D panels with both source and vortex panels [11]. The unknown singularities of these panels are solved by a system of linear algebraic equations generated by applying the flow-tangency conditions and calculating the induced velocity at the control points.

After getting to know how the program XFLR5 models the aerodynamic properties, the first analysis was performed. To create a model of an aircraft XFLR5 requires that all used airfoils are analysed before applying them in a 3D wing. After this analysis a 3D wing can be created. The first step in creating the model for the VTOL concept was recreating the model of the 2014 group. To verify the results of this model, a comparison was made with the results of the 2014 group. As the new results were identical to those of the 2014 group the model was considered valid. This first model was used as a basis and alternated based on the input of the other designed subsystems.

5.1.2 Rotor drag

The used aerodynamic analysis program explained in section 5.1.1 was not able to analyse the influences of the rotors. Therefore these influences were analysed manually. During the design the objective was to minimise the amount of drag caused by the rotors. Therefore it was decide that the rotors would only have two rotor blades. These rotor blades can be placed parallel to the airflow during nominal flight to minimise

the frontal area and therefore drag. In chapter 7 the rotors were further analysed and the two rotor blade design turned out to produce enough thrust. During the design process the propulsion and aerodynamic groups had close interaction to come to the best concept.

To find a correct way of analysing the drag of the rotors a detailed literature study was performed. This research showed that analysing the rotor drag involved complicated modelling methods outside the scope of this project. It was decided that by using the windtunnel reference data shown in figure 5.1 a correct estimation of the added drag could be found. In order to use the reference data the rotors were analysed as if they were a flat plate. The rotor diameter was taken as the length and the cord as the width of the plate.

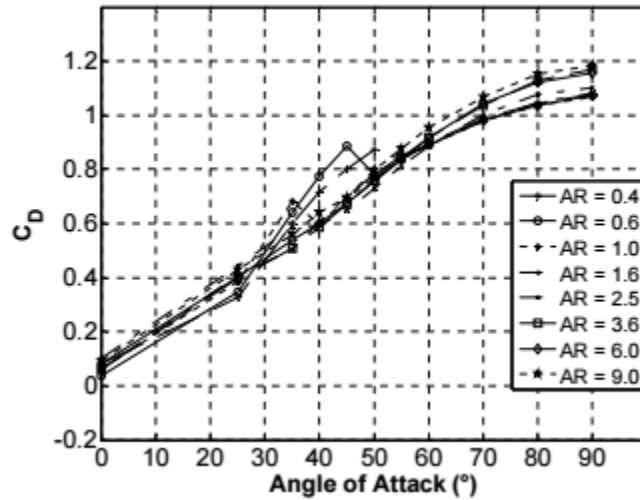


Figure 5.1: C_D with respect to angle of attack for a flat plate with different aspect ratios, taken from [24]

For the main rotors this resulted in an aspect ratio of $0.0556/0.538 = 0.103345$ using in figure 5.1 the nearest aspect ratio of 0.4, the C_D for every angle of attack could be found. Because of the impreciseness of the method used, the highest C_D value was taken: $C_{D_{rotor}} = 0.25$, this occurs at an 18 deg angle of attack. Using equation 5.1 the $C_{D_{rotor}}$ of the rotor blades could be converted into the C_D of the total kite.

The projected area of one rotor is $0.0556 * 0.538 = 0.0299 \text{ m}^2$ the projected area of the full kite is $S_{Kite} = 12.7 \text{ m}^2$ using these values it could be calculated that the added drag coefficient for both rotors is $C_{D_{rotor}} = 0.00117$ this is negligible compared to the total drag coefficient of the kite.

$$C_{D_{Total}} = \frac{C_{d_{rotor}} S_{rotor}}{S_{Kite}} + C_{D_{Kite}} \quad (5.1)$$

The same procedure was used to model the tail rotor. During the nominal flight this rotor is placed into the flow to produce power for the on board systems. Although the frontal area of the tail rotor during rotation is circular it was modelled as a square flat plate with aspect ratio of 1. Again figure 5.1 shows the drag coefficient. The projected area of the tail rotor is $0.31^2 * \pi = 0.301907 \text{ m}^2$ using the radius of 0.31 m^2 of the tail rotor discussed in section 7.3. Plugin in this value and using equation 5.1 it could be calculated that the added drag coefficient is $C_{D_{rotor}} = 0.00594$ This extreme case was considered for a conservative estimation. Further windtunnel tests need to be performed to validate this outcome.

5.1.3 Post stall C_L and C_D

The flight profile of the rigid kite includes high angles of attack due to vertical climb of the the VTOL system during low winds speeds. These angles of attack are usually post stall, and if the aircraft is not pitched, are

negative as well. The limitations of the XLFR model is that it does not simulate post stall behaviour of the rigid kite. Therefore, a simple analytic expression is used to calculate the lift coefficient by modelling the wing as a flat plate at post stall angles of attack. The expression is given in equation 5.2 as provided in [4]. In equation 5.2, the term $\text{sign}(\alpha)$ refers to whether α is positive or negative. Note, the equation requires in α in rad.

$$C_{L,\text{flatplate}} = 2 \text{sign}(\alpha)(\sin \alpha)^2 \cos \alpha \quad (5.2)$$

Similarly, the drag coefficient of the flat plate model is also obtained by using data provided in 5.1. Again, the drag coefficient is interpolated using the data given at post stall angle of attacks. Based on the wing Aspect Ratio (AR) of 7.9 as mentioned in section 5.2, the drag coefficients were interpolated using data of the AR = 9 curve in figure 5.1. Furthermore, it is also identified that the centre of pressure of a flat plate at post stall angles of attack occurs approximately at 50% of the flat plate length [24].

5.1.4 Winglets

The design goal was to keep the output power of the new design the same as the output of the 2014 design. As the choice for the VTOL concept involved changing the existing kite, the power output was most likely to change as well. Therefore all changes to the design were checked with the power model described in section 3.7. Using the power model it could be concluded that the added weight and drag of the rotors would bring the produced power down. In order to compensate for this, winglets were introduced. Winglets increase the C_L and decrease the C_D , in other words they improve the lift-over-drag ratio. This increase in performance is caused by the decrease of the wingtip vortices. In the 2014 design the pressure difference between the top and the bottom of the wing causes the air to spiral up and form vortices. These vortices create extra downwash and decrease the amount of lift produced. On top of that, due to the winglets, the lift induced drag is lowered. Figure 5.2 shows the influence of wing vortex and the change in vortex by adding a winglet.

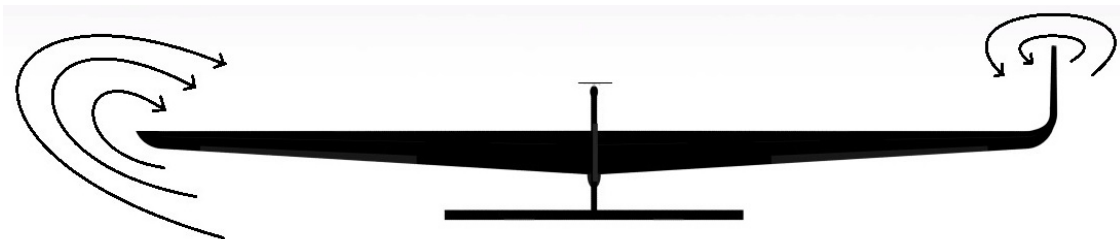


Figure 5.2: Difference in wingtip vortex due to winglets, with at the left part of the wing the 2014 design and at the right part the new design. The kite is shown from behind.

During the design phase multiple parameters determined the effectiveness of the winglets: the chord length, the taper ratio, the cant and sweep angle, the height and the degree of integration into the wing. The selection of these parameters was highly correlated to other design decisions. For instance, the height of the winglets is driven by the rotor wing interaction, described in section 5.1.5, and the sweep angle was limited by the centre of gravity. This selection procedure is further explained in section 5.3.

5.1.5 Rotor/wing interaction

For the sizing of the rotors and winglets, and the feasibility of the selected VTOL concept, the influence of the wing on the rotor's performance is a crucial factor. It was quickly observed that this is a very complex aerodynamic system, therefore an analysis was performed based on literature, used to estimate the rotor

performance. This section qualitatively describes the most important influences on rotor performance, and concludes with the estimated rotor performance.

As the wing is in part of the wake of the rotor, the outflow of the rotor is blocked, causing a reduction in rotor performance. While the rotor itself can receive a small gain in thrust T [N], the total efficiency is reduced, as the wing is forced down, indicated by the wing download DL [N]. The wing download is normalised by dividing it by the thrust, giving a ratio of DL/T . Throughout this section, extensive use is made of [6], concerning the wing download for the Bell Boeing V-22 Osprey, a tiltrotor aircraft. While it concerns an old analysis, it presents a clear and concise overview of the different phenomena involved, backed up by small-scale and full-scale testing. Moreover, all test have been performed using the same test set-up and methods, making the different effects comparable.

Ground effect

Considering the rotor thrust alone, the rotor's figure of merit is increased by introducing the wing. This can be seen in figure 5.3, where the figure of merit is increased by some 3 percent due to the addition of the wing. Note that this only describes the rotor performance; the wing download is not included in the figure of merit.

This increase in the figure of merit is attributed to the rotor being in ground effect, with the wing acting as the ground. In ground effect, the wingtip vortices are reduced in strength, and an area of higher pressure is formed below the wing. This causes an increase in lift, and a decrease in drag. [12] For the rotor, this makes for an increase in the figure of merit.

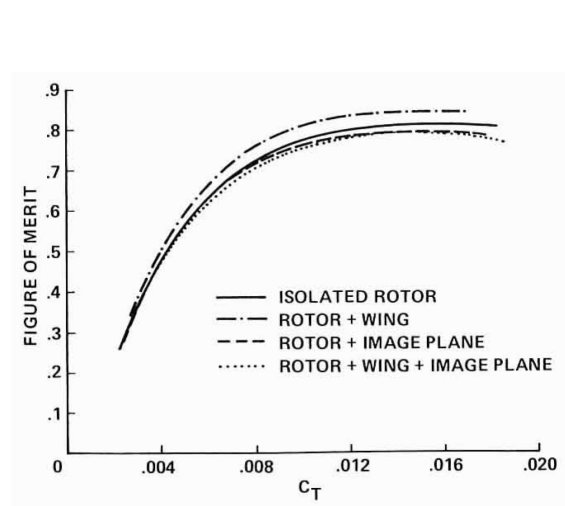


Figure 5.3: Large-scale V-22 rotor performance [6]

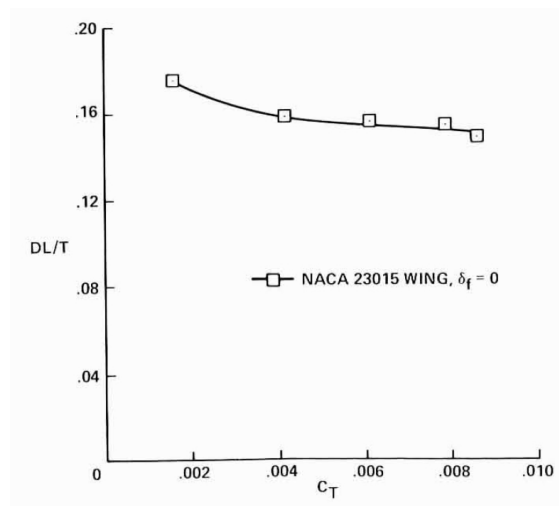


Figure 5.4: Effect of the thrust coefficient on wing download [6]

Effect of the wingspan

As the rotor downwash hits the wing, part of the airflow is redirected to a spanwise direction due to the high pressure area at the wingtip. When this spanwise flow reaches the centre of the aircraft, the opposing flow and fuselage (if present) force the air upwards. From this, it is recirculated into the rotors, creating a rotational flow. This rotational flow is schematically drawn in figure 5.5. It is reasoned that this both increases and decreases the performance.

An increase in performance is suggested by [6], as the rotation increases the inflow to the rotor, increasing its power. A decrease is expected, due to the upward flow in the centre, and the energy needed to redirect

the flow, thus changing its momentum. In total, a decrease in performance is predicted. It is expected that this effect is increased as the span b is decreased, or as the rotor radius R is increased. This can be combined by saying that for this effect to be smallest, the value of rotor radius to wing span, R/b needs to be small i.e., a relatively small rotor as compared to the wingspan is to be chosen.

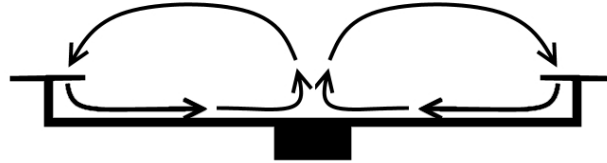


Figure 5.5: Schematic depiction of spanwise flow

Effect of thrust coefficient

The thrust coefficient, as described in equation 7.6, contributes to the wing download, the effect is depicted in figure 5.4. It can be seen that an increase in thrust coefficient brings about a decrease in wing download. A higher thrust coefficient can be seen as the same thrust being produced with a smaller rotor radius and thus a higher rotational speed. Due to the higher rotational speeds at high thrust coefficients, the rotor tips move faster with respect to the rotor root sections than at low thrust coefficients. This is directly related to the dynamic pressure in the wake, a higher thrust coefficient increases the dynamic pressure in the outboard sections of the rotor with respect to the dynamic pressure in the inboard sections of the rotor.

Test by [6] have shown that the outboard sections contribute mostly to spanwise flow, as described in the previous paragraph, while the inboard section contribute mostly to chordwise flow. The chordwise flow can be seen as the wing airfoil under an angle of attack of minus 90 deg, i.e., directly from above. Obviously, this comes with a very high drag coefficient, causing a high wing download. The effect of chordwise flow on wing download is larger than the effect of spanwise flow. As a higher thrust coefficient increases the amount of spanwise flow relative to the chordwise flow, a decrease in wing download is observed as the thrust coefficient is increased.

Effect of the vertical offset

The distance in the z -axis between the rotor and the wing affect the wing download significantly. The distance is determined in a ratio of vertical offset z to rotor radius R , resulting in a coefficient z/R . Intuitively, this would seem logical, as a larger offset should decrease all effects of the rotor and wing interaction, being zero at an infinite distance.

However, [6] suggests that the effect of vertical offset is not trivial. The rotor wake is wide and relatively slow just below the rotor, but accelerating and decreasing in radius further away. As described above, this would result in higher dynamic pressures further away, increasing wing download. However, at small values for z/R , the interaction between the separate rotor blades and the wing becomes larger, increasing wing download. Possibly, this is due to the air being squeezed between the rotor and wing. Overall, a decrease in wing download is caused by an increase in the coefficient z/R , as is shown in figure 5.6.

Effect of the rotor rotation direction

Tests have been performed addressing the different rotation direction of the rotors: leading edge to trailing edge, or vice versa. As both rotors need to turn opposite directions to counter the torque produced, the sign of the rotation expressed in leading edge to trailing edge direction of the inner part of the rotor will be the same for both main rotors. Figure 5.7 shows the results for measurements performed by [6], showing a clear preference for trailing edge to leading edge rotation.

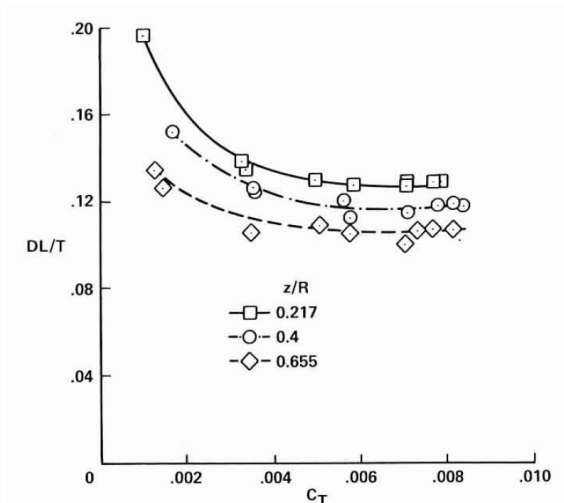


Figure 5.6: Effect of the vertical offset of rotor [6]

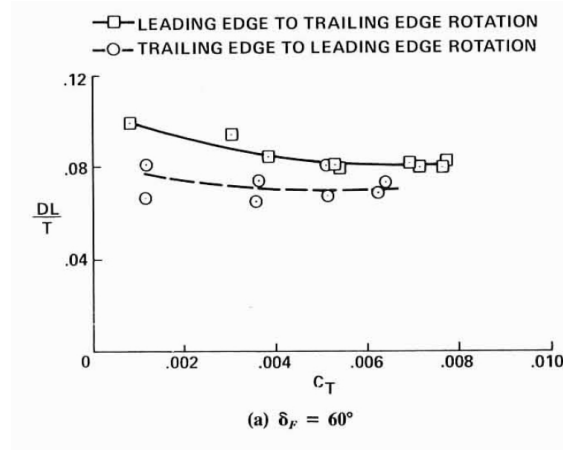


Figure 5.7: Effect of the rotation direction of rotor [6]

However, it should be noted that these tests have been performed with large flap angles, the figure shown is with a flap deflection of 60 deg. As the flaps cover the entire span of the V-22's wings, at a significant portion of the chord length, the influence these flaps can have is large. It was observed that the decrease in wing download was larger at larger flap angles. As the design of the VTOL kite does not allow the flaps (ailerons) to be placed under a significant portion of the rotor, it may be that a difference in wing download between rotational directions is no longer present.

Other effects

Several effects have been described by [6], which have not been included in this analysis, as they were deemed out of the scope of the design, or not applicable to the design.

First of all, as mentioned above, the effect of the flap angle has been excluded. This is due to the fact that the kite's ailerons are very small with respect to the span and chord, as compared to those of the V-22.

Secondly, the effect of airfoil, and the wings' incidence angle has been left out. While it contributes to the wing download due to the previously described chordwise flow, this effect is deemed very complex. Moreover, changing the wing airfoil was seen as a change too big to make, as it would lead to a complete redesign of the kite, leaving little time for the design of the launching and landing system.

One factor not discussed by [6] is the influence of the wing tip chord c_{tip} , relative to the rotor radius R . It is predicted that a higher value for c_{tip}/R increases wing download, as the wing area in the rotor downwash is relatively larger than for a low value of c_{tip}/R . A value of 0 would mean there is virtually no wing area affected by the rotor, therefore no wing download.

Finally, the investigation of [6] concerns tiltrotor aircraft, which have a straight angle between the motor and wing, due to the rotation. The design of the VTOL AWE system features fixed rotors on winglets, allowing for a blended winglet with a certain radius. The effect of this blend radius is not investigated. It is expected that a large radius will decrease the wing download, as the rotor downwash is given a smooth transition to the wing, instead of hitting it straight from above. This should reduce the chordwise flow effect, as well as the spanwise flow effect as the downwash is turned to spanwise flow more efficiently. There is, however, no experimental data to back up this suggestion.

5.2 Specifications

All specifications related to the aerodynamic design can be found in table 5.1. Table 5.1a contains all specifications of the main wing, note that the wing span excludes the winglets, but includes the central lifting body. Table 5.1b and 5.1d contain the specifications of the horizontal and vertical tail, respectively. Finally, the winglets' sizes are shown in table 5.1c. A schematic overview has been presented in figure 4.1.

Table 5.1: Main wing specifications

(a) Main wing specifications		(b) Horizontal tail specifications	
Element	Value	Element	Value
Wing span without winglets	9.4 [m]	Span	3.073 [m]
Airfoil	Wortmann FX 73-CL3-152	Airfoil	NACA 0010
Root chord	1.814 [m]	Root chord	0.62 [m]
Tip chord	0.726 [m]	Tip chord	0.62 [m]
Surface area	12.7 [m ²]	Surface area	1.9 [m ²]
Aspect ratio	7.9 [-]	Distance LE_tail to LE_wing	4.547 [m]
Quarter-chord sweep	0 [deg]	Quarter-chord sweep	0 [deg]
Dihedral	2 [deg]	Dihedral	0 [deg]
Angle of incidence	0 [deg]	Angle of incidence	-3.5 [deg]
Body central chord	2.664 [m]		
Body width	0.5 [m]		

(c) Winglet specifications		(d) Vertical tail specifications	
Element	Value	Element	Value
Height offset	1 [m]	Span	1.185 [m]
Airfoil	PSU-90-125WL	Root chord	0.62 [m]
Root chord	0.6 [m]	Tip chord	0.62 [m]
Tip chord	0.4 [m]	Quarter-chord sweep	-9 [deg]
Blend radius	300 [mm]		
Quarter-chord sweep	2 [deg]		
Cant angle	90 [deg]		

5.3 Final design

In this section, the performance of the system specified in section 5.2 is discussed. Also, the methods and steps taken to get to this design are described.

5.3.1 Aerodynamic performance

Based on the geometrical specifications of the rigid kite, the overall aerodynamic characteristics of the rigid kite was analysed based on the XFRLR5 model and the analytic expression for the flat plate. The results of the aerodynamic analysis are presented for the entire rigid kite and the separate lifting elements as $C_L - \alpha$ and $C_D - \alpha$ curves. Figure 5.8 shows the variation of the C_L and C_D coefficients with angle of attack α . As shown, the lift curve exhibits the expected linear behaviour in the nominal range of α . The rigid kite stalls

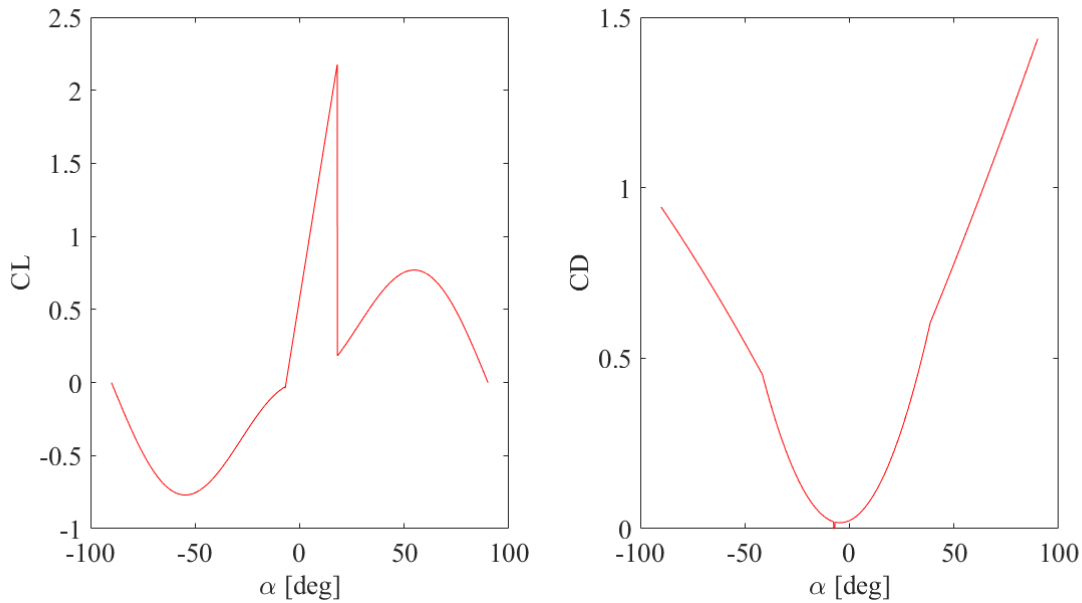


Figure 5.8: Lift C_L and drag C_D coefficients of the whole rigid kite without tether

at $\alpha_s = 18$ deg for positive angles of attack and $\alpha_s = -7$ deg for negative angles of attack. The stall angles originate from the direct foil analysis of the Wortmann FX-73-CL3-152 airfoil at a flight speed of 30 m/s. In the post stall angle of attack range, equation 5.2 is used to obtain the lift coefficients. A similar approach is used to obtain the drag C_D coefficient of the rigid kite. In the nominal α region, an interpolated relation from the XFLR5 data is used. In the post stall regions, an interpolated function based on flat plate drag data of figure 5.1 is used. Figure 5.9 shows the interpolated curves based on the XFLR5 analysis data. For the $C_L - \alpha$ curve, a linear interpolation is used given by equation 5.3. Similarly, a quadratic relation is used for $C_D - \alpha$ curve give in equation 5.4. Both interpolated functions show a good relation to the fitted data. Note that the input of the fitted function is α in unit rad. The interpolated function from the drag of flat plate model based on figure 5.1 is also given by equation 5.5.

$$C_L = 0.58 + 5.10\alpha \quad (5.3)$$

$$C_D = 1.04\alpha^2 + 0.1624\alpha + 0.02384 \quad (5.4)$$

$$C_{D,flatplate} = |0.07657\alpha^2 + 0.7567\alpha + 0.0581| \quad (5.5)$$

5.3.2 Airfoils and planform

As mentioned in section 5.1.5, changing the wing airfoil was considered not an option, unless absolutely necessary. No issues were found, however, so the wing airfoil was kept the same as determined by [19]. For the winglet, a PSU-90-125WL airfoil was chosen. This airfoil was suggested by [19], and proved effective in C_L and C_D performance in XFLR5.

It was found that the neutral point was in front of the centre of gravity. As explained in section 3.6, it was attempted to move the centre of gravity forward. Simultaneously, it was investigated whether the neutral point could be moved backward. This has been done by increasing the horizontal tail surface, e.g. the chord and/or span of the horizontal stabiliser, and changing the airfoil. Increasing the tail beam length was not considered, as this would shift the centre of gravity further back as well. Increasing the tail size proved to

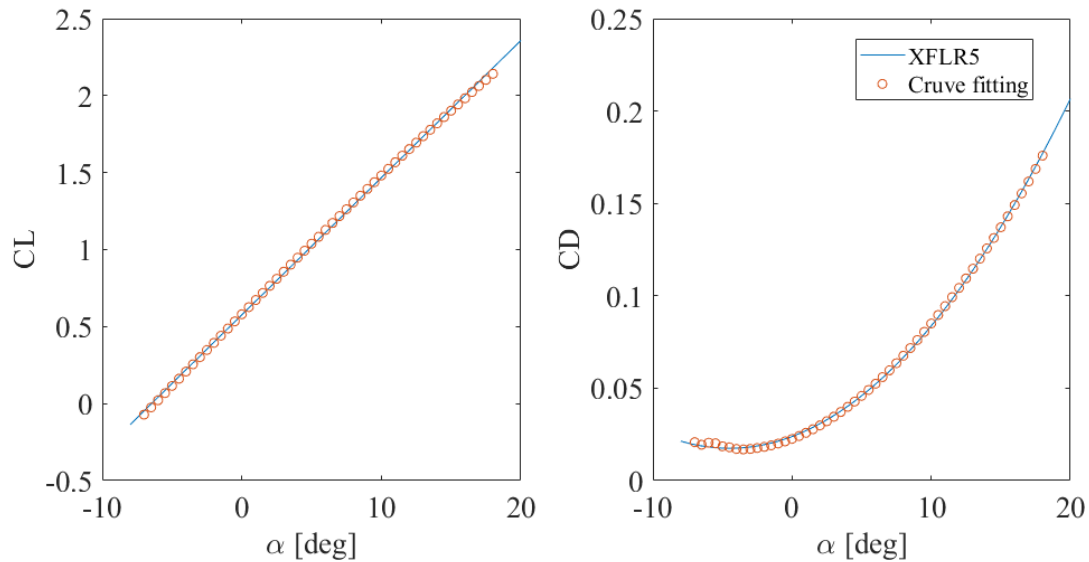


Figure 5.9: Curve fitting for lift and drag coefficients from XFLR5 data of the whole rigid kite



Figure 5.10: The four investigated winglet designs are shown, from left to right: the double winglet, integrated winglet, dropped winglet, spiroid winglet and the final design.

be not efficient, moving the neutral point back only slightly. As different airfoils, a symmetric NACA 0024 and cambered NACA 2412 and NACA 2424 airfoils have been evaluated using XFLR5. It was observed, however, that this proved ineffective in moving the neutral point backward. Therefore, it was concluded that the tail sizing was not to be altered with respect to the original design.

During nominal flight, the aircraft will fly close to its stall angle of 18 deg. As the NACA 0010 has a stall angle of 15 deg, the horizontal tail is given an angle of incidence of -3.5 deg. This is done so that if the stall angle of the wing is reached, the tail has not yet stalled, providing stability.

The maximum wingspan of 10 m was kept, to maintain a high power output. With a winglet blend radius of 300 mm, a wing span of 9.4 m was obtained. This wingspan includes the lifting body housing the batteries and electronics. The body was sized by keeping the trailing edge at the same x-coordinate, and increasing the chord length until the batteries could be given the correct offset forward.

5.3.3 Winglet sizing

As discussed in section 5.1.4 the winglets were evaluated on multiple parameters: the chord length, the taper, the cant and sweep angle, the height and the degree of integration into the wing. Before determining these parameters, proven concepts for winglets design were analysed. These concepts are shown in figure 5.10 this figure also shows the chosen design for comparison with the considered concepts.

Table 5.2: C_L and C_D at 18deg angle of attack for the different winglet concepts

	Double winglet	Integrated winglet	dropped winglet	Spiroid winglet	Final design
C_D	0.174	0.178	0.184	0.189	0.176
C_L	2.012	2.105	2.149	2.232	2.125

After investigating the commonly used winglet shapes, research was done into selecting the best airfoil. Reference literature showed that the PSU-90-125WL airfoil used for winglets of high-performance sailplanes was the most promising [13]. This airfoil is specially designed for a wide range of Reynolds numbers just as the operational range of the kite.

After selecting the airfoil a side step was made to draft the parameters. This was done independent of the winglet concept as most parameters originate from non-aerodynamic requirements. The determination of these parameters is described below.

The determination of the parameters was started with selecting the chord length. The chord length at the root of the winglet was fixed and given by the tip chord at the wing. The chord length at the top of the winglet was sized such that the motor could be integrated into the winglet, as was the design objective.

Secondly the sweep of the winglet was determined. The sweep angle was determined doing a trade-off between stability and aerodynamic performance. This was needed due to the fact that the 2014 design was only stable when attached to the tether. For safety reasons the centre of gravity needed to be shifted in front of the neutral point to make the kite stable in case of a tether breakage. As the motors and therefore a significant mass is located on top of the winglets the sweep angle could be used to shift the centre of gravity. On the other hand a negative sweep (forward) allowed the wingtip vortex to return and therefore cancelled out the positive effects of having winglets. After iterating this trade-off it was decided that the positive effect of having a negative sweep angle did not outweigh the negative effects on the aerodynamics. To solve the stability problem a blended body was introduced. Placing the battery mass in this body shifted the centre of gravity in front of the neutral point solving the stability issues.

The height of the winglet was determined by the amount of download the rotors would have on the main wing. This offset was determined to be 1 m and is further explained in section 5.3.4.

The cant angle was first chosen to be smaller than 90 deg and a large blend radius was selected, as can be seen in the second picture in figure 5.10. A more in-depth analysis of these parameters showed that this decreased the projected area which has a large influence on the power output. Therefore the cant angle was increased to 90 deg and the blend radius decreased to 300 mm.

Now that the parameters were fixed all winglet concepts could be analysed with the same parameters ensuring fair comparison. Table 5.2 shows the different C_L and C_D of each concept at 18 deg angle of attack. Based on this table the final concept was selected which is the most right concept in figure 5.10. The final design clearly performs better than the other concepts, only the spiroid winglet has a higher C_L although this comes with a higher C_D . As the spiroid concept seemed promising it was not selected for the final design as the projected area of the wing went down significantly influencing the power output. For the other concepts the projected area stayed approximately the same.

Finally the integration of the rotor was taken into account. On top of the PSU-90-125WL airfoil a NACA0024 was placed to fit the motor of the main rotors. The NACA0024 was selected based on the high thickness needed to house the motor.

5.3.4 Estimated wing download

To estimate the final download created by the proposed design, a quick method is setup based on the effects described in this chapter. As all coefficients influencing the download differ between the V-22 test setup and the proposed design, an exact prediction is difficult. As a start, the value for the wing download is predicted using the measurements from [6] for the coefficient that differs the most. From this value, the other influences are described, and the total difference is estimated.

The coefficient with the biggest difference is that for the vertical offset z/R . The extrapolated results from

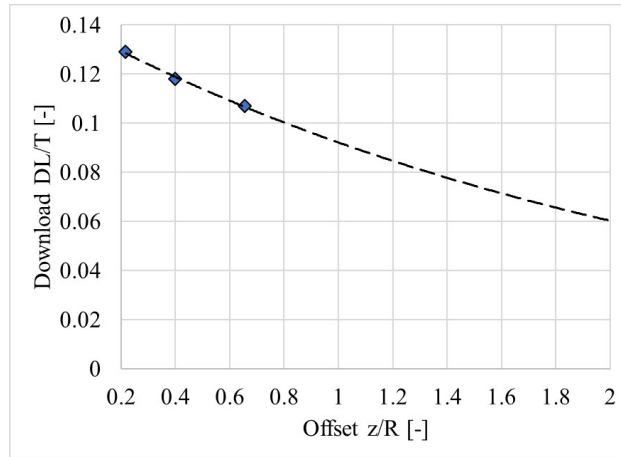


Figure 5.11: Extrapolated effect for the effect of vertical offset

the measurements is shown in figure 5.11. For the trendline, an exponential line is chosen as it approaches zero as the value for z/R goes to infinity. With a rotor radius of 0.538 m, as is obtained in chapter 7, and a vertical offset of 1 m as proposed, a value $z/R = 1.9$ is found, corresponding to a wing download of 6.3 %. From this value, the other effects are estimated. Table 5.3 shows the difference in coefficients between the V-22 test set-up and the proposed design. The final column qualitatively estimates the effect on the estimated value, where 1 indicates a very negative effect, i.e. higher download, 2 a negative effect, 3 neutral, and 4 and 5 positive and very positive, respectively.

Table 5.3: Comparison of coefficients for wing download between the design and the V-22 test setup

	V-22	DSE	Expected effect
c_{tip}/R	0.42 [-]	1.35 [-]	1
b/R	3.00 [-]	18.59 [-]	4
C_T	0.008 [-]	0.011 [-]	3
Blend radius	None	300 [mm]	4

When taking the average of the effects, a value of 3 is found, indicating that the positive and negative effects are expected to cancel each other out. This makes for an expected wing download of 6.3 %. A safety is added by increasing this to a wing download of 8 %. This last value is the value of wing download that the propulsion system is sized for.

6 | Stability & control

In this chapter the stability and controllability of the kite are analysed. In the first section, the kite's flight paths are simulated. From the flight paths the most important kite attitudes, or kite modes, are selected. The selected kite modes will be analysed for stability in section 6.2. In this section it is calculated whether it is possible to keep the kite in equilibrium, and what control surface deflection is required in order to do so. After the stability has been demonstrated, the final section will elaborate on the control system. An autopilot will be designed that uses the stability equations to keep the kite in the air.

6.1 Flight paths

A key component of designing an automated launching and landing system for the rigid kite is the suitable trajectory that the kite should follow under different conditions. These estimated trajectories can be optimised for design considerations such as energy and power requirement. Therefore, simulating the climb and descend phase of the rigid kite is important in understanding the flight performance characteristics. In this chapter the trajectories for climb and descent are modelled and simulated in MATLAB as shown in sections 6.1.2 and 6.1.3.

6.1.1 Flight path assumptions

The flight paths of the climb and descend phase can be simulated by developing and solving the equations of motion for the system. However, the equations of motion can be quite complex depending on the level of fidelity of the model. In this stage of the design phase, a low fidelity model is built to estimate the flight parameters during the climb and descend phases. Therefore, a number of assumptions are introduced in the system that must be accounted for. These assumptions have been listed and described below.

- The flight path model assumes a two degrees of freedom model. This assumption implies that the dynamics of the rigid kite are only simulated in a single plane.
- The rigid kite is simulated as a point mass. Therefore, the attitude of the rigid kite remains independent of the dynamics of the kite through the simulation as pitching moment is neglected.
- The model assumes the wind shear model as explained in section 3.7.1. Therefore, the wind velocity is discretised along the trajectory altitude. The aerodynamic forces significantly depend on the wind speed. Therefore, this assumption has a significant affect on the climb and descend trajectory.
- The model assumes a symmetric flight condition. Therefore, the side forces acting on the aircraft are ignored and it is assumed that the rigid kite has no rolling or yawing moment. In static conditions, this assumption will have a minimal affect on the flight trajectory as the aircraft is oriented in a headwind configuration and no sideslip occurs. Furthermore, the control surfaces are assumed to have zero deflection and thus, produce no asymmetric moments on the kite.
- The tether force is modelled based on the tether weight. Other contributing factors such as pulley friction and winch inertia are neglected. These inertia and friction coefficients depend on the tether force and reel out speed. Thus, the affect of this assumption is negligible on the flight trajectory as tether force and reel out speed are low compared to other considerations.
- The model also assumes the same assumptions listed in chapter 5 for the aerodynamic model. This assumption includes the post stall lift and drag coefficients for the rigid kite. This assumption is likely to have the most significant affect on the model as the post stall aerodynamic coefficients are first order estimates. Therefore, the aerodynamic forces are likely to be the largest source of error in the model.

- Finally, the model assumes that the required thrust (from the rotors) is available immediately. Thus, the transition time between different levels of required thrust is not included in the model. Furthermore, the transition time between different attitudes of the rigid kite is also not included in the model. Thus, these system inputs are modelled as finite jumps in the simulation.

6.1.2 Take-off and climb simulation

In order to simulate the take-off and climb phase of the rigid kite, a numerical model was built based on a set of analytic equations of motion. These analytic expressions are derived by using a free body diagram as shown in figure 6.1.

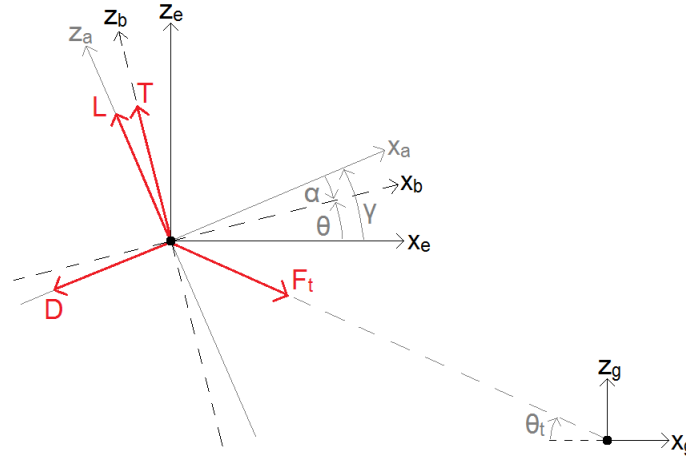


Figure 6.1: Free body diagram for the point mass model of the rigid kite during climb

As figure 6.1 shows, all forces acting on the aircraft act through a single point. Furthermore, four different reference frames are utilised in the simulation. The $X_g Z_g$ reference frame is aligned with the ground station as the X_g axis points opposite the direction of the wind direction based on the wind shear model. The Z_g reference frame completes the right handed reference frame. The reference frame is considered as an inertial reference frame.

The $X_e Z_e$ reference frame is the vehicle carried reference frame that remains aligned with the $X_g Z_g$ reference frame. Thus, the X_e axis points parallel to the X_g axis and the Z_e axis completes the right handed reference frame.

The $X_b Z_b$ reference frame is the body reference frame for the rigid kite. The origin of the reference frame is at the point mass and the X_b axis is aligned pointing to the leading edge of the main wing. The Z_b axis completes the right handed reference frame and the thrust vector from the main rotors is parallel to this axis.

Finally, the $X_a Z_a$ is the aerodynamic reference frame of the rigid kite. The X_a axis points along the apparent aerodynamic velocity and Z_a axis completes the right handed reference frame. Using these reference frames, the different forces acting on the point mass are resolved.

The aerodynamic force can be derived in the $X_a Z_a$ reference frame as following:

$$\vec{F}_A^a = \frac{1}{2} \rho v_{app}^2 S_{proj} \begin{bmatrix} -C_D \\ C_L \end{bmatrix} \quad (6.1)$$

In equation 6.1, C_D and C_L are the system lift and drag coefficients and S_{proj} is the projected area. These coefficients are derived in chapter 5. The density (ρ) is also derived in section 3.7.2. Finally, v_{app} is the magnitude apparent velocity that can be expressed as following:

$$\vec{v}_{\text{app}} = \begin{bmatrix} V_{w,\text{ref}} + v_x \\ v_z \end{bmatrix} \quad (6.2)$$

Equation 6.2 shows the expression for the apparent aerodynamic velocity for the kite. The wind velocity $V_{w,\text{ref}}$ is calculated based on the wind shear model. The v_x and v_z are the rigid kite velocity components in the $X_e Z_e$ reference frame with respect to the ground station. Similarly, the thrust force vector from the main rotors can be resolved in the body reference frame as indicated in equation 6.3. T_{main} is the main rotor thrust magnitude. T_{tail} is the tail rotor thrust that can be directly resolved in the $X_e Z_e$ reference frame because the rotor is tiltable as shown in equation 6.4.

$$\vec{T}_{\text{main}}^b = \begin{bmatrix} 0 \\ T_{\text{main}} \end{bmatrix} \quad (6.3)$$

$$\vec{T}_{\text{tail}}^e = \begin{bmatrix} T_{\text{tail},x} \\ T_{\text{tail},z} \end{bmatrix} \quad (6.4)$$

Furthermore, the weight force can be decomposed along the $X_e Z_e$ reference frame as the following in equation 6.5.

$$\vec{W}^e = \begin{bmatrix} 0 \\ mg \end{bmatrix} \quad (6.5)$$

Finally, the tether force is resolved in the $X_e Z_z$ reference frame as the following 6.6.

$$\vec{F}_t^e = \begin{bmatrix} r\rho_{w,t}g \cos \vartheta_t \\ -r\rho_{w,t}g \sin \vartheta_t \end{bmatrix} \quad (6.6)$$

In equation 6.6, r and $\rho_{w,t} = 0.0274$ kg/m are the tether length and tether density. Moreover, angle ϑ_t is a reference angle used to relate the ground station and respective position of the rigid kite as shown in equation 6.7.

$$\vartheta_t = \pi - \tan \left(\frac{z_g}{x_g} \right)^{-1} \quad (6.7)$$

In equation 6.7, x_g and z_g are the coordinates for the rigid kite position in the $X_g Z_g$ reference frame. Finally, the equations of motion can be derived in the $X_e Z_e$ reference frame as the following equation 6.8.

$$m \begin{bmatrix} \vec{a}_x \\ \vec{a}_z \end{bmatrix} = \vec{W}^e + \vec{F}_t^e + \vec{T}_{\text{tail}}^e + \bar{R}_{b,e}(\vartheta) \vec{T}_{\text{main}}^b + \bar{R}_{a,e}(\gamma) \vec{F}_A^a \quad (6.8)$$

In equation 6.8, $\bar{R}_{b,e}(\vartheta)$ is the clockwise rotation matrix from the $X_b Z_b$ reference frame to $X_e Z_e$ reference frame. Similarly, $\bar{R}_{a,e}(\gamma)$ is the clockwise rotation matrix from the $X_a Z_a$ reference frame to $X_e Z_e$ reference frame. A clockwise rotation matrix about an arbitrary angle χ can be defined using equation 6.9.

$$\bar{R}_\chi = \begin{bmatrix} \cos \chi & -\sin \chi \\ \sin \chi & \cos \chi \end{bmatrix} \quad (6.9)$$

One additional relation was used to formulate the numerical model. Equation 6.10 defines the relation between the flight path angle γ , the pitch angle ϑ and the angle of attack α . The angle α is important in

calculating the lift and drag coefficients used in equation 6.1. Note that the orientation of α as defined in figure 6.1 is negative. Equation 6.11 shows the derivation for angle γ .

$$\vartheta = \alpha + \gamma \quad (6.10)$$

$$\gamma = \tan \left(\frac{v_z}{v_x + V_{w,ref}} \right)^{-1} \quad (6.11)$$

Using equations 6.1 - 6.11, a numerical model is built to solve for the kinetic and kinematic properties of the point mass through the take-off and climb phase. The model was built based on certain requirements, constraints, inputs and objectives. These properties of the numerical model can be best explained using a program logic diagram as shown in figure 6.2.

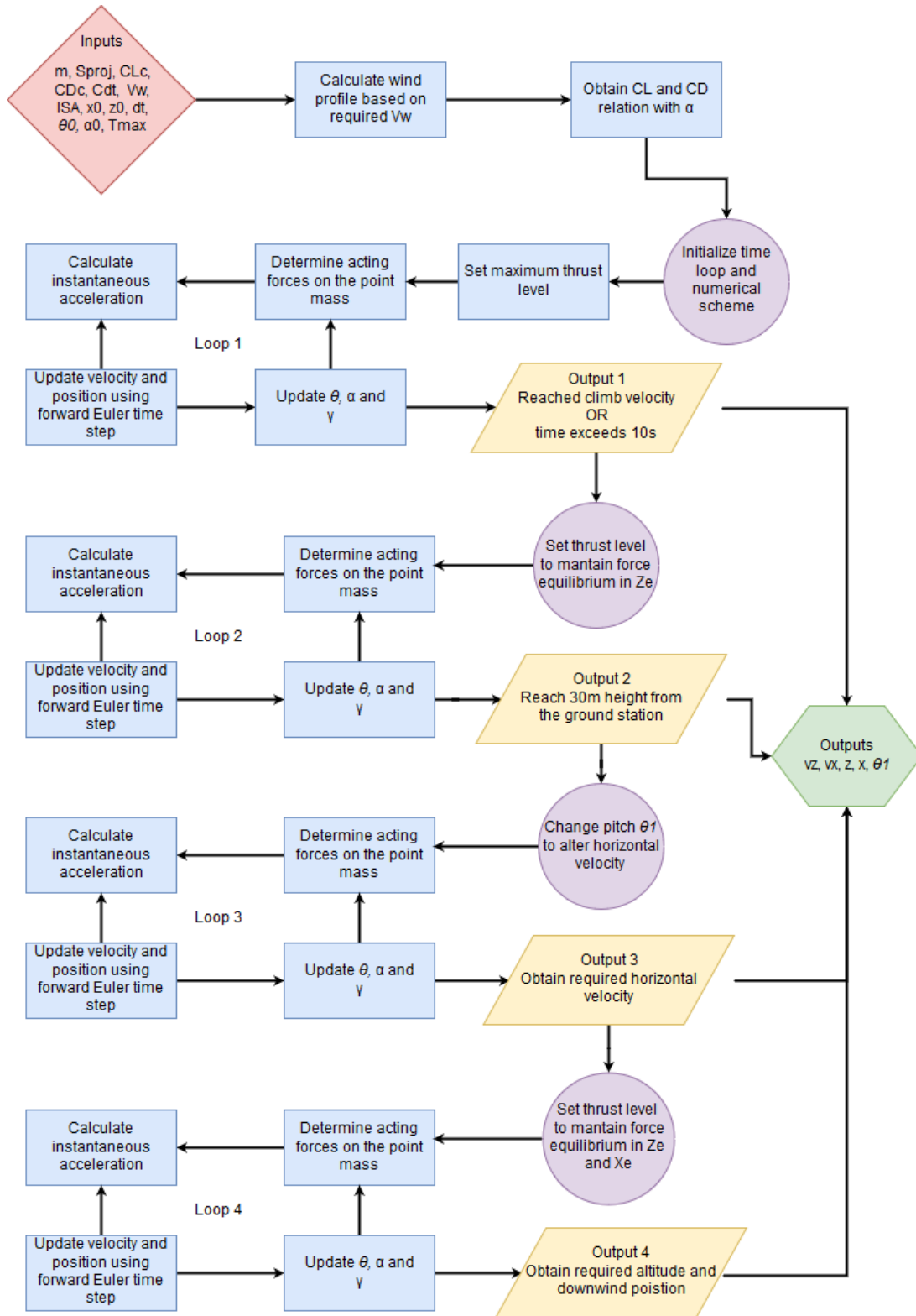


Figure 6.2: Program logic for the take-off and climb numerical scheme

As figure 6.2 shows, the numerical scheme comprises of four main time stepping loops which use the forward Euler technique to solve the derived equations of motion. Each loop is terminated if the desired objectives are met. These objectives are inspired by safety or performance constraints.

In the first time step loop, the thrust from the main rotors is set to a maximum level in order to reach a climb velocity as quickly as possible. The constraint is set to ensure that the rigid kite reaches a minimum safe distance from the ground station as quickly as possible without drifting too far downwind where a safe termination of launching procedure is not possible anymore. A time constraint is also set on the loop such that the numerical scheme can still proceed forward even if the desired climb velocity is not reached.

Thereafter, the numerical scheme enters a second loop where the vertical climb velocity v_z is held constant by using the thrust level to maintain force equilibrium about the Z_e axis. The second loop terminates when the kite exceeds an altitude $z_g = 30$ m. Again this constraint is motivated due to safety and risk concerns as introducing a pitching moment might lead to unstable dynamic moments. The minimum altitude is used to provide a sufficient distance such that the rigid kite can correct its orientation without causing damage.

Next, the program enters loop three where the force equilibrium about the Z_e axis is maintained. However, the pitch angle ϑ of the rigid kite is changed before the loop is initiated. As ϑ is a control input in this numerical scheme, the angle is maintained in further loops of the numerical scheme. The rigid kite is pitched backwards to gain acceleration along the X_e axis such that a desired horizontal climb velocity v_x is achieved. The loop is terminated once the desired climb v_x is achieved. The v_x velocity is constrained by two factors: the flight path angle γ and the ratio between v_z and v_x . The flight path angle is constrained to be between $\gamma = -90/+90$ deg based on equations 6.10 and 6.10, and the limitations of the aerodynamic model as the C_L and C_D coefficients are only calculated till $\alpha = -90/+90$ deg. This constrains the v_x velocity to be lower than $V_{w,ref}$. Furthermore, the ratio between v_z and v_x is also a factor as it relates the downwind position to the altitude of the rigid kite.

Table 6.1: All relevant inputs and outputs for the model presented in figure 6.2

Input	Value	Description
m	75 [kg]	Estimated mass of the kite including contingency
S_{proj}	12.7 [m ²]	Kite projected area
CL_c	—	Lift curve of the rigid kite
CD_c	—	Drag curve of the rigid kite
C_{dt}	1.1 [-]	Tether drag coefficient
$V_{w,ref}$	6.8 - 25 [m/s]	Input for the required wind velocity at 100m altitude
ISA	[kg/m ³]	Density model based on ISA
x_0 z_0	0.0 [m]	Position of the kite with respect to the ground station
dt	0.1 - 0.001 [s]	Time step for the numerical scheme
ϑ_0 α_0	0.0 [deg]	Attitude of the rigid kite
T_{max}	875 [N]	Maximum combined thrust from the main rotors
$T_{max,tail}$	100 [N]	Maximum thrust from the tail rotor
Output	Value	Description
v_z	[m/s]	Vertical climb velocity (optimise)
v_x	[m/s]	Horizontal climb velocity (optimise and constrained)
z_g	150 +/- 10 [m]	Vertical position of the rigid kite (objective)
x_g	-260 +/- 20 [m]	Horizontal position of the rigid kite (constrained and objective)
ϑ_1	[deg]	Pitch angle for gaining X_e acceleration (optimise)

Finally, the program initiates loop four. In the final loop, the thrust level is controlled such that both the v_z and v_x velocity components are held constant. This is done by ensuring force equilibrium about both the X_e and Z_e axes by using thrust from the tail and the main rotors. As the tail rotor is tiltable, thrust can be generated along X_e axis without a significant pitch angle. The loop is terminated once the desired altitude

of $z_g = 150$ m is reached. This altitude refers to the operational altitude of the rigid kite. Furthermore, the nominal operation of the rigid kite also occurs at an elevation angle of 30 deg. This approximates to a downwind position of $x_g = -260$ m from the ground station. These are the final objectives of the take-off system of the rigid kite. Thereafter, the kite can launch into nominal operation by flying crosswind and using tether force during reel-in phase. The main parameters for the numerical scheme are summarised below in table 6.1.

The maximum thrust from the main motors is constrained to be at an extra 10% of the combined weight and download of the rigid kite. This ensures that the weight of the motors is kept at minimum and the influence on nominal operation is not significant. The maximum thrust from the tail rotor is kept at a minimum as well to reduce the influence of rotor drag and influence of tail motor mass on the centre of gravity. This is detailed further in 3.6.

Furthermore, v_z , x_z and ϑ_1 are the main outputs of the numerical scheme that can be optimised. These parameters influence the required thrust and the duration of the entire launch procedure. Thus, using equation 7.17 to derive power and integrating over the launch time, the take-off and climb parameters can be optimised for minimum energy requirement.

Moreover, the required wind velocity at 100 m altitude is set such that the rigid kite can operate under nominal conditions. The $V_{w,ref} = 25$ m/s is derived from the cut-out wind speed requirement. Alternatively, the $V_{w,ref} = 6.8$ m/s comes from the stall speed requirement such that the rigid kite can operate nominally throughout the flight range of 100 – 350 m. This numerical scheme with the identified inputs was used to estimate the climb trajectory for multiple wind speed conditions within the range. The results from the optimised trajectory of the two critical flight conditions are illustrated and discussed below. These are the minimum wind speed of $V_{w,ref} = 6.8$ m/s at 100 m and $V_{w,ref} = 25$ m/s at 100 m.

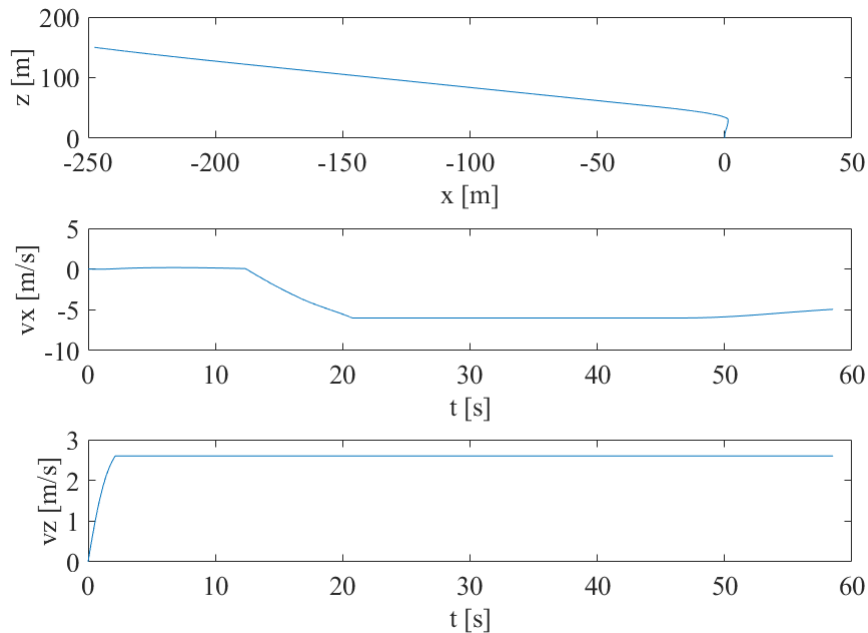


Figure 6.3: Climb trajectory of the rigid kite at $V_{w,ref} = 6.8$ m/s at 100 m

Figure 6.3 shows the climb profile of the rigid kite at $V_{w,ref} = 6.8$ m/s. As the graphs show, the climb phase is divided into four main phases described as time loops in the numerical model. Initially, the rigid kite accelerates to a vertical climb velocity of $v_z = 2.6$ m/s as indicated in graph three. Next, the rigid kite maintains force equilibrium about Z_e till $z_g = 30$ m is reached. Thereafter, the pitch $\vartheta = 5$ deg of the kite is

altered such as to gain acceleration about X_e axis. This is reflected in the second graph of figure 6.3 as the rigid horizontal climb velocity accelerated to $v_x = -6$ m/s.

The final climb phase is the linear phase where force equilibrium is held. As figure 6.3 shows, both v_x and v_z components are held constant through majority of the phase. It is important to identify that the apparent airspeed of the rigid wing does change as indicated in equation 6.2 as well as the flight path angle γ using equation 6.11. Due to relation 6.10, the aircraft experiences high negative post stall angles of attack α . Another feature of the climb phase in the final time period is that force equilibrium around Z_e axis is no longer sustained as the thrust force by the main rotors and the tail rotor is restricted to a single pitch and thus, only forward thrust in the $X_b Z_b$ reference frame. The outputs of the numerical simulation are summarised in table 6.2.

Table 6.2: Outputs of the optimised climb model for the climb model at $V_{w,ref} = 6.8$ m/s

Output	Value	Description
v_z	2.6 [m/s]	Vertical climb velocity
v_x	-6.0 [m/s]	Horizontal climb velocity
z_g	150.0 [m]	Vertical position of the rigid kite
x_g	-247.6 [m]	Horizontal position of the rigid kite
ϑ_1	5 [deg]	Pitch angle for gaining X_e

The outputs derived in table 6.2 are optimised using the level of thrust required from the main and tail rotors at each time instance. This thrust level is converted to power using 7.17 and integrated to calculate energy. The optimisation energy is best illustrated using figure 6.4 showing the thrust level at various combinations of v_z and v_x velocity components.

As figure 6.4 shows, the lower the climb velocity is set, the more time is required to climb to reach the required altitude. For example, climb at $v_z = 2.6$ m/s requires only $t = 68$ s to climb. In comparison, climb at $v_z = 1.0$ m/s requires $t = 151$ s of climb time. However, the level of thrust required from the main rotors is lower for lower vertical climb velocities as angle α and thus, drag coefficient C_D are smaller. In comparison, the level of thrust required by tail rotor is larger to maintain force equilibrium around X_e axis. The v_x is constrained by the relation 6.12. This constraint is derived due to the requirement of reaching a downwind position of -260 m from the ground station.

Moreover, the maximum velocity v_z is constrained such that angle of attack α does not exceed $-80/80$ deg. A 10 deg safety margin is taken for pitching due to wind gusts and other disturbances. The relation between v_z and α is defined by using equations 6.2, 6.10, 6.11 and 6.12. Therefore, the optimisation of the numerical scheme for climb involved simulating the climb trajectory for multiple v_z climb velocities up until a maximum value constrained by maximum thrust available and the above mentioned factors. Note, that an additional 10 s is added to the climb time leading to $t = 69$ s such as to account for transition control inputs that are simulated as step inputs currently.

$$v_x \approx \frac{v_z}{0.45} \quad (6.12)$$

The results of the optimisation technique can also be illustrated using table 6.3a. As shown, the induced energy required for the climb decrease as the v_z is increased because the time required to climb is slower. However, this is restricted by minimum possible α . The final parameter ϑ_1 was also optimised based on energy. In general, the higher the pitch angle, the more energy was required. However, a minimum pitch is required to reach the desired v_x velocity.

Similar to the $V_{w,ref} = 6.8$ m/s simulation, the climb trajectory was also obtained for $V_{w,ref} = 25$ m/s at 100 m altitude. Due to a significant difference in the wind speeds, the climb model was altered to achieve the objectives of climb. The output parameters are tabulated in table 6.3b.

As indicated, the vertical climb velocity is significantly higher than the slower wind speed model. Therefore, a higher thrust force T_{main} is required to reach and sustain the v_z . This increase in thrust requirement

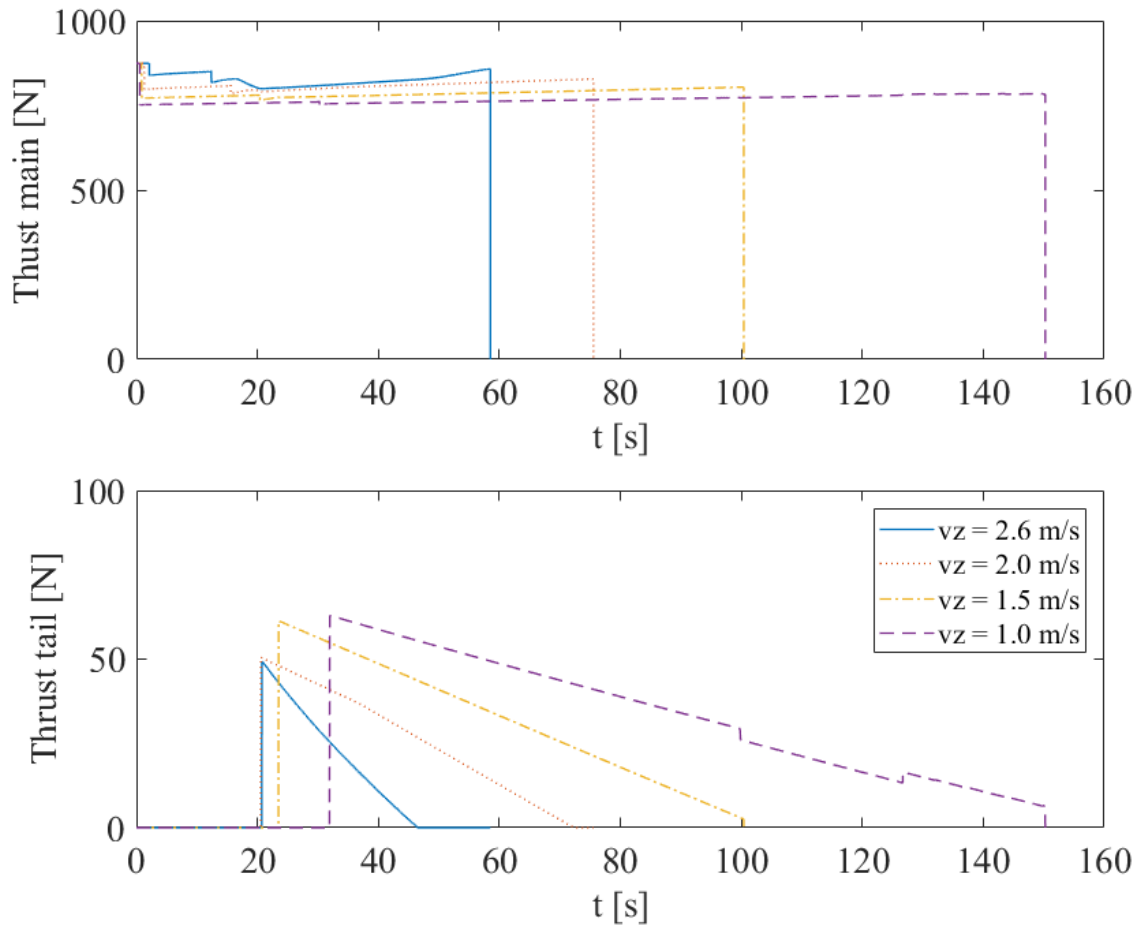


Figure 6.4: Required thrust at various v_z velocities at $V_{w,ref} = 6.8$ m/s

(a) Outputs of the optimised climb model for the climb model at $V_{w,ref} = 6.8$ m/s

v_z [m/s]	v_x [m/s]	t [s]	α [deg]	E [J]
2.6	-6.0	58.5	-80.6	1.66e+6
2.0	-4.6	75.6	-50.7	2.08e+6
1.5	-3.5	100.4	-27.0	2.67e+6
1.0	-2.3	150.3	-18.4	3.86e+6

(b) Outputs of the optimised climb model for the climb model at $V_{w,ref} = 25$ m/s

Output	Value
v_z	3.8 [m/s]
v_x	-7.9 [m/s]
ϑ_1	0 [deg]
T_{max}	1000 [N]
$T_{max,tail}$	100 [N]
z_g	150 [m]
x_g	-271 [m]
E	1.58e+6 [J]
α	-14.4 [deg]

translates to roughly an additional 50 N force which can be sustained by the motors. The motors are currently sized with a 1.5 safety factor and operate lower than the maximum power as explained in section 7.4. Furthermore, the rigid kite does not need to pitch to gain acceleration. Hence, ϑ is sustained at 0 deg.

Finally, the required energy to climb is less than that of the minimum wind speed requirement as the climb is made within 43 s. The thrust profile of the rotors is indicated in figure 6.5.

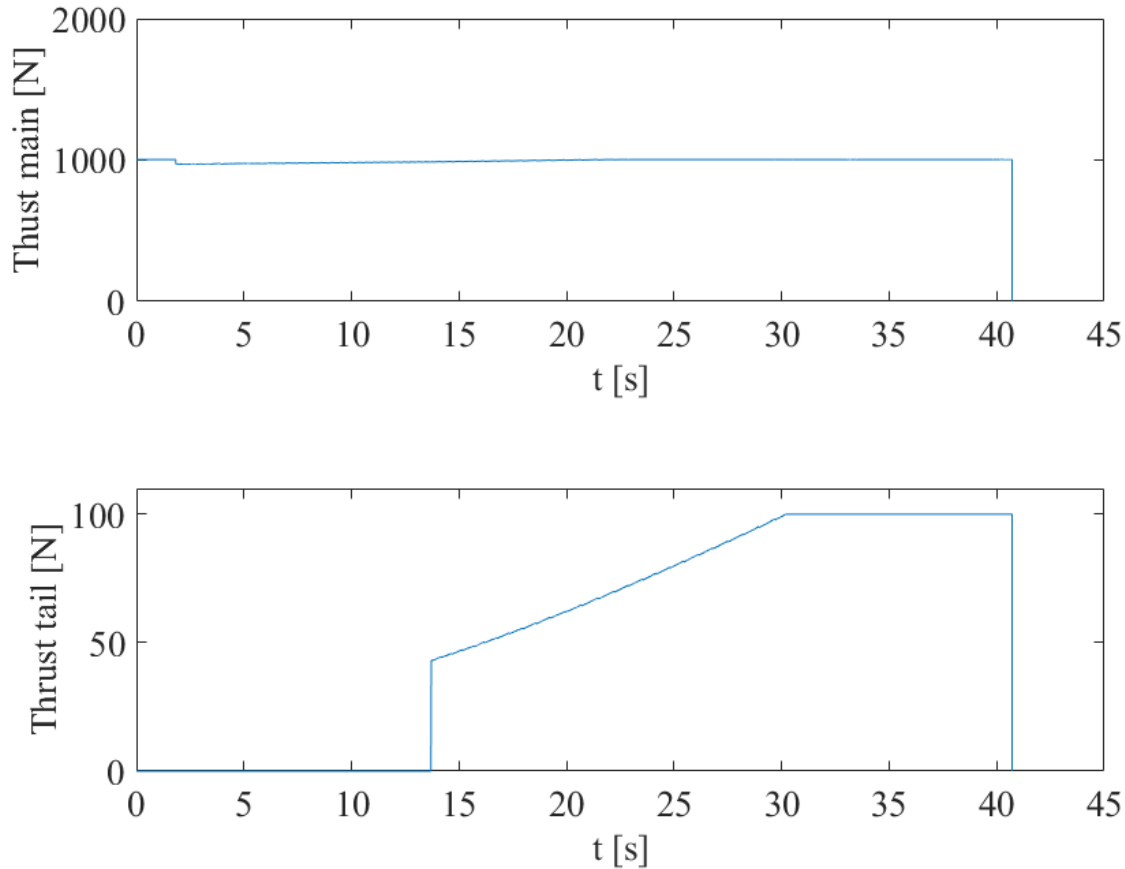


Figure 6.5: Required thrust for optimised climb profile at $V_{w,ref} = 25$ m/s

As figure 6.5 shows, the required thrust profile is different for the climb trajectory at higher wind speed. The constraining factor is not the angle of attack α but rather the thrust from the main and tail rotors. These rotors are used to maintain force equilibrium during climb; however, due to a larger magnitude of v_{app} , the aerodynamic forces become more dominant.

6.1.3 Descent and landing simulation

Similar to the the take-off and climb phase, the descent and landing flight path can be analysed by building a numerical model based on equations 6.1 - 6.11. The numerical model is explained using figure 6.7 as the program logic flow chart. As the figure shows, the numerical model calculates the wind profile based on a prescribed wind speed and the wind shear model. Furthermore, functions for $C_L - \alpha$ curve and $C_D - \alpha$ curve are also interpolated.

Next, the numerical scheme is initiated using a time loop. In the first loop, the tether force is set a desired level such as to reach certain x_g position at $z_g = 50$ m height from the ground station. In this iterative loop,

the forces are computed at each time step and the kinetics of the point mass are updated using forward Euler.

Thereafter, the numerical scheme enters loop 2 where the tether force is reverted back to only the tether weight. The scheme of the loop is similar to loop one. Once the target $z_g = 20$ m is reached, the time-stepping loop two is terminated. Next, the pitch of the aircraft is changed to ϑ_1 such as to decelerate the point mass using the thrust from the main rotors. Again, the loop is terminated when the desired v_x velocity is achieved.

In the final phase of the descent, the rigid kite is pitched back to ϑ_0 and the kite is accelerated about Z_e axis to achieve a touchdown (landing) velocity of $v_z = -0.2$ m/s. There are a number of constraints that are imposed on the landing numerical model. The constraints can be best explained using the landing simulation for the critical condition of $V_{w,ref} = 1$ m/s at 100 m. The significant parameters of the simulation are discussed in table 6.4.

Table 6.4: All relevant inputs and outputs for the model presented in figure 6.7

Input	Value	Description
m	75 [kg]	Estimated mass of the kite including contingency
S_{proj}	12.7 [m ²]	Kite projected area
CLc	[-]	Lift curve of the rigid kite
CDc	[-]	Drag curve of the rigid kite
Cdt	1.1 [-]	Tether drag coefficient
$V_{w,ref}$	1 [m/s]	Input for the required wind velocity at 100m altitude
ISA	[kg/m ³]	Density model based on ISA
x_0 z_0	-260.0 150.0 [m]	Position of the kite with respect to the ground station
dt	0.01 [s]	Time step for the numerical scheme
ϑ_0 α_0	0.0 0.0 [deg]	Attitude of the rigid kite
T_{max}	875 [N]	Maximum combined thrust from the main rotors
$T_{max,tail}$	100 [N]	Maximum thrust from the tail rotor
Output	Value	Description
$x_{g,mid}$	-79.1 [m]	Horizontal position at $z_g = 50$ m
v_z	-0.18 [m/s]	Vertical descent velocity at touchdown
v_x	0.35 [m/s]	Horizontal velocity at touchdown
z_g	0.01 [m]	Vertical position of the rigid kite after landing
x_g	1.2 [m]	Horizontal position of the rigid kite after landing
ϑ_1	20 [deg]	Pitch angle for gaining X_e decelerating using main thrust
T_{max}	980 [N]	Actual maximum thrust required by the main rotors
$T_{max,tail}$	0 [N]	Actual maximum thrust required by the tail rotor
$F_{t,max}$	581 [N]	Maximum tether force used to reel in the tether
$a_{z,1}$	3.2 [m/s ²]	Required deceleration in Z_e axis from 60 to 30 m
E	2.0e+5 [J]	Energy required for descend phase

As table 6.4, a number of parameters are significant for the landing numerical scheme of the rigid kite. These can be best explained using the table and figure 6.6. In the initial landing phase, the rigid kite is reeled back in using an additional tether force of 500 N combined with the tether weight. This phase terminated when the rigid kite reaches an altitude of $z_g = 50$ m and the additional tether force is nulled. Thereafter, the rigid kite is allowed to glide back until an altitude of $z_g = 50$ m is reached.

Next, the rigid kite is pitched to $\vartheta_1 = 20$ deg. The X_e component of the thrust from the main rotors is used to decelerate the kite until a $v_x \approx 0$ m/s is reached. The phase is terminated and the aircraft is pitched back to $\vartheta_0 = 0$ deg. In the final phase, the v_x is more or less constant about 0 m/s as the aerodynamic forces and tether force are minuscule. Simultaneously, the rigid kite is decelerated to $v_z = -0.2$ using the following

equation 6.13.

$$a_{z,\text{des}} = \frac{v_{\text{des}}^2 - v_z^2}{2(z_{\text{des}} - z_g)} \quad (6.13)$$

The thrust force from the main rotors is set such as to achieve an acceleration of $a_{z,1} = 3.2 \text{ m/s}^2$ in the final landing stage to achieve a $v_z > -0.2 \text{ m/s}$. This translates to an impact energy of $E_{\text{impact}} = 6 \text{ J}$ which based on a displacement of $d_{\text{dis}} = 0.01 \text{ m}$ translates to an average impact force of $F_{\text{imp}} \approx 600 \text{ N}$ ¹.

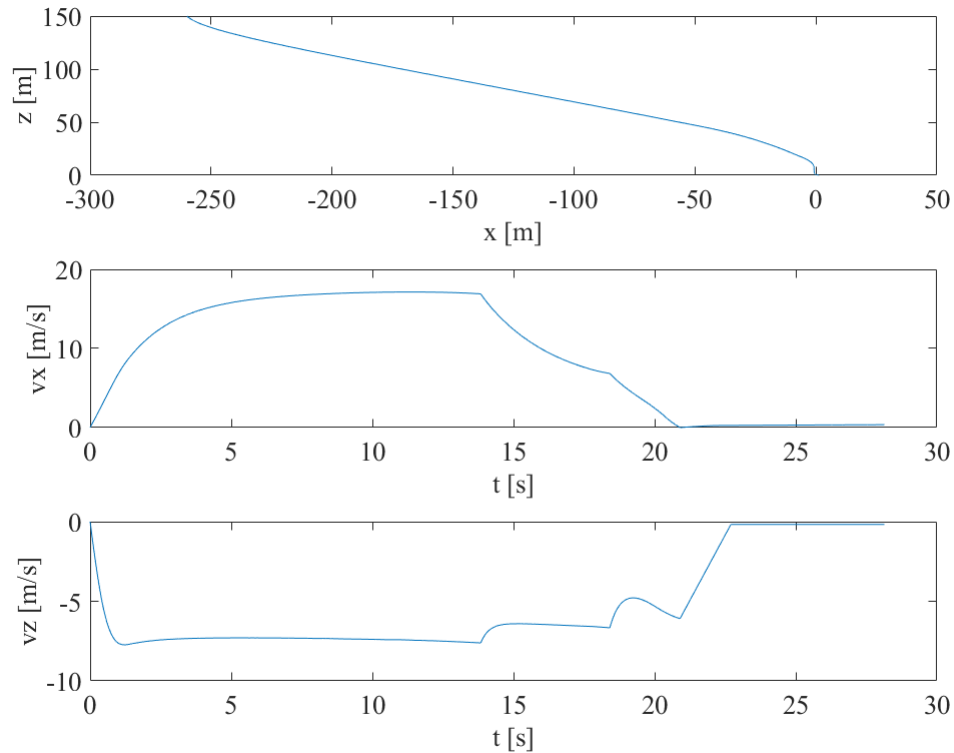


Figure 6.6: Landing simulation for rigid kite at $V_{w,\text{ref}} = 1 \text{ m/s}$

¹Retrieved from: <http://hyperphysics.phy-astr.gsu.edu/hbase/flobi.html> [Accessed on 27-06-2017]

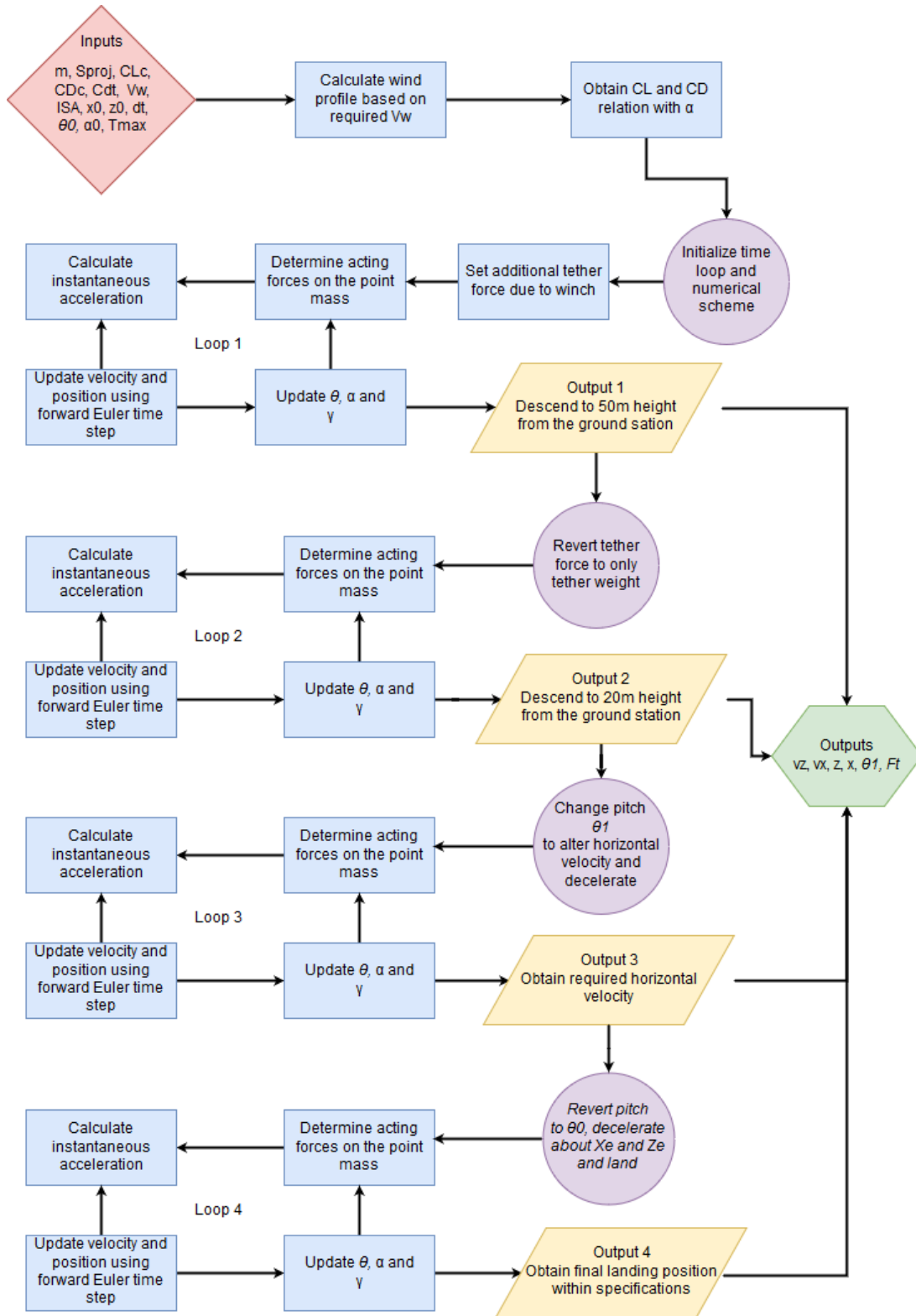


Figure 6.7: Program logic for the descent and landing numerical scheme

6.2 Stability

In this section the kite will be analysed by calculating force and moment equilibrium for hovering flight. Once equilibrium is known, the next step is to calculate the stability, or in other words: whether equilibrium can be maintained.

6.2.1 Equilibrium in climbing flight

Moment equilibrium of the rigid kite is significant during the climb phase. As shown in section 6.1, a list of assumptions are made for the climb phase simulation. One of these assumptions states the pitch of the rigid kite is held constant. Therefore, longitudinal moment equilibrium is important for the results of the simulation to remain valid. Similarly, the rigid kite is considered in symmetric motion during climb. Thus, lateral moment equilibrium is also an important factor. However, these moments are expected to be smaller than the pitching moment. The pitch moment equilibrium during climb is analysed below. However, a number of assumptions are made for this analysis as well.

- All the assumptions from the flight path list of assumption are carried forward excluding the point mass assumption and the two degrees of freedom model assumption.
- The pitching moment is not coupled with lateral dynamics. For example, symmetric flight assumption is used while analysing pitching moment equilibrium.
- The intermediate transition between jumps in thrust and pitch angle are not analysed. Thus, only the motion through the climb phase is considered.
- The drag force from both the wing and the horizontal tail is assumed to be acting through the centre of gravity plane. Therefore, the drag force is considered insignificant in analysis of the longitudinal moment equilibrium.
- The tether force acts through the centre of gravity of the rigid kite throughout the climb phase.
- The \vec{v}_{app} experienced by the empennage is considered to be similar to the main wing. Moreover, the downwash gradient is ignored as during the climb phase, the rigid wing always experiences negative post stall angles of attack. This is a major limitation of the aerodynamic model, and thus the moment equilibrium model.
- The centre of pressure x_{cp} for both the main wing and horizontal is considered to be at 50% of the length of the mean aerodynamic chord (mac) of the lifting surface independent of the angle of attack. This is based on the experimental data from reference paper [24].

The longitudinal moment of equilibrium can be analysed in the $X_e Z_e$ reference frame using the following equation 6.14.

$$\begin{aligned} \sum M_y = & \bar{R}_{a,e}(\gamma) \vec{F}_{A,w}^a \cdot \begin{vmatrix} 0 \\ x_{cg} - x_{cp,w} \end{vmatrix} + \bar{R}_{a,e}(\gamma) \vec{F}_{A,t}^a \cdot \begin{vmatrix} 0 \\ x_{cg} - x_{cp,t} \end{vmatrix} + \\ & + \bar{R}_{b,e} \vec{T}_{main}^b \cdot \begin{vmatrix} z_{cg} - z_{rotor} \\ x_{cg} - x_{rotor} \end{vmatrix} + \vec{T}_{tail}^e \cdot \begin{vmatrix} z_{cg} - z_{rotor,t} \\ x_{cg} - x_{rotor} \end{vmatrix} = 0 \end{aligned} \quad (6.14)$$

Equation 6.14 is used to derive the required tail rotor thrust \vec{T}_{tail}^e to maintain a net zero moment about the Y_e axis. The Y_e axis is a three dimensional extension of the $X_e Z_e$ plane and points outwards to complete the right handed reference frame. Equation 6.14 is coupled into the climb model, and the tail thrust is updated to maintain pitch angle ϑ . However, as \vec{T}_{tail}^e also influences the force equation 6.8, an inner iterative loop is introduced into each time-step loop such as both moment and force sums are maintained as required

from the climb model. Again, the longitudinal equilibrium is shown for the two critical wind conditions $V_{w,ref} = 6.8$ m/s and $V_{w,ref} = 25$ m/s at $z_g = 100$ m. The significant inputs and outputs for the stall wind condition are tabulated in table 6.5. As table 6.5 indicates, the optimised parameters of the climb phase remain unaltered. However, the thrust required of the tail rotor is changed. Particularly, the $T_{tail,z}$ is non-zero for a certain time interval to ensure moment equilibrium. This is illustrated in figure 6.8. As the figure shows, the $T_{tail,z}$ is the driving component of required tail thrust. In contrast to the two degree of freedom climb model, the $T_{tail,z}$ also contributes to the total tail thrust required and energy consumption. The trend in figure 6.8 is as expected. The required $T_{tail,z}$ is higher where acceleration from horizontal $T_{tail,x}$ force is not required. As the $T_{tail,x}$ decreases after peak force requirement, $T_{tail,z}$ rises again to maintain stability.

Table 6.5: All relevant inputs and outputs for pitch moment equilibrium model ($M_y = 0$ Nm) at stall wind speed condition

Input	Value	Description
m	75 [kg]	Estimated mass of the kite including contingency
$S_{proj,w}$	10.8 [m ²]	Main wing projected area
$S_{proj,t}$	1.9 [m ²]	Horizontal tail projected area
CLc,w	[-]	Lift curve of the main wing
CDc,w	[-]	Drag curve of the main wing
CLc,t	[-]	Lift curve of the empennage
CDc,t	[-]	Drag curve of the empennage
Cdt	1.1 [-]	Tether drag coefficient
x_{cg}	0.57 [m]	Centre of gravity location from leading edge in x
z_{cg}	0.30 [m]	Centre of gravity location from leading edge in z
$x_{cp,w}$	0.65 [m]	Centre of pressure of main wing from leading edge in x
$x_{cp,t}$	4.86 [m]	Centre of pressure of horizontal tail from leading edge in x
x_{rotor}	0.50 [m]	Centre of gravity location from leading edge in x
z_{rotor}	1.48 [m]	Centre of gravity location from leading edge in z
$x_{rotor,t}$	4.55 [m]	Centre of gravity location from leading edge in x
$z_{rotor,t}$	1.37 [m]	Centre of gravity location from leading edge in z
T_{max}	875 [N]	Maximum combined thrust from the main rotors
$T_{max,tail}$	100 [N]	Maximum thrust from the tail rotor
Output	Value	Description
v_z	2.6 [m/s]	Vertical climb velocity
v_x	-6.0 [m/s]	Horizontal climb velocity
z_g	150 [m]	Vertical position of the rigid kite
x_g	-251 [m]	Horizontal position of the rigid kite
ϑ_1	5 [deg]	Pitch angle for gaining X_e acceleration
$T_{max,tail,x}$	42 [N]	Maximum tail thrust along X_e axis
$T_{max,tail,z}$	56 [N]	Maximum tail thrust along Z_e axis
t	58 [s]	Take-off and climb time
E	1.61e+6 [J]	Energy required for climb during launch

Similarly, the numerical model for climb at $V_{w,ref} = 25$ m/s with pitching moment equilibrium is also simulated. The results are tabulated in table 6.6. As the table shows, the optimised parameter for v_z remains unaltered. However, the climb trajectory does change for the rigid kite. These changes largely occur due to including the horizontal surface into the calculations. As the rigid kite climbs at post stall negative angles of attack α , the contribution of lift is opposite to the kite motion. Therefore, higher thrust is required to counter the force at high wind speed. Moreover, the tail rotor cannot sustain force equilibrium around the

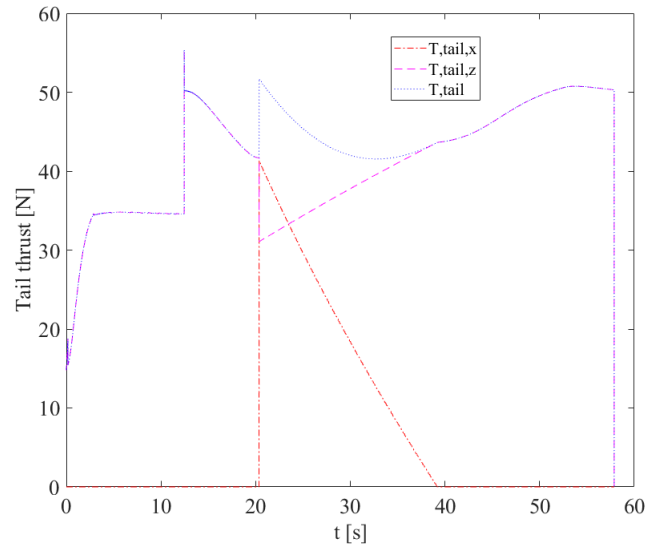


Figure 6.8: Required tail thrust for optimised climb profile at $V_{w,ref} = 6.8$ m/s and moment equilibrium

X_e axis. Therefore, an additional tether force is used (to be applied by the winch) to control the v_x velocity of the rigid kite. This additional tether force also contributes to a Z_e component needed to be overcome by the main rotor thrust. Finally, the maximum force allowed in the tail is restricted to 130 N as the value is still considered within the safety margin and throttle setting of the motor chosen. An additional change is in the level of energy required for climb. However, only a 5% excess energy is required in comparison to the design energy used for the batteries in section 7.5 based on the climb at stall speed condition. This value is considered to be well within the safety factor and thus, the climb can be sustained.

Table 6.6: All relevant outputs for pitch moment equilibrium model ($M_y = 0$ Nm) at cut-out wind speed condition

Output	Value	Description
v_z	3.8 [m/s]	Vertical climb velocity
v_x	0 to -10.8 [m/s]	Horizontal climb velocity
z_g	140 [m]	Vertical position of the rigid kite
x_g	-278 [m]	Horizontal position of the rigid kite
ϑ_1	0 [deg]	Pitch angle for gaining X_e acceleration
$T_{max,tail,x}$	130 [N]	Maximum tail thrust along X_e axis
$T_{max,tail,z}$	99 [N]	Maximum tail thrust along Z_e axis
t	41 [s]	Take-off and climb time
E	1.80e+6 [J]	Energy required for climb during launch

In terms of stability during climb, the rigid kite cannot be considered a stable system. This is because the rigid kite flies at post stall negative angles of attack and thus, both $x_{cp,w}$ and $x_{cp,t}$ are behind the x_{cg} . Moreover, the gradient of the lift curve changes at different angles of attack. Finally, the magnitude of thrust forces is significantly higher at expected lower wind speeds. Thus, an active stabilisation is required by using the tail rotor during climb. However, as shown above, the moment produced by the tail rotor thrust is significant enough to correct the pitch of the aircraft if required.

6.2.2 Equilibrium in hovering flight

The hovering flight is an important part of the kite's flight envelope. Hovering is performed by staying stationary in the air using a combination of the wing and rotors. The FBD for this mode is shown below, after which the the force and moment equations are derived.

Assumptions:

- Tether tension assumed zero during hover. Hence the tether force will consist solely of the tether weight.
- Tether weight is acting in the centre of gravity of the kite. Hence it will not contribute to the moment about the y-axis.
- The tail rotor thrust will only be used for stabilising the kite, not to carry its weight. This will result in a negligible overestimate of the required main tether thrust.
- Horizontal drag is acting through the centre of gravity, and causes no moment about the Y-axis.
- Tail wind speed is not affected by the main wing downwash, hence $V_h = V$

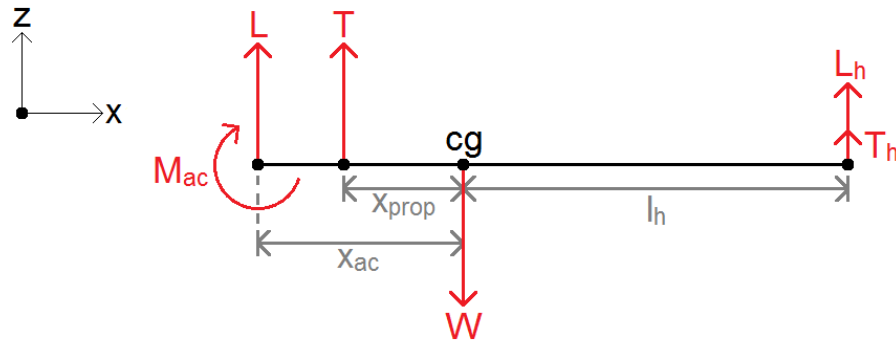


Figure 6.9: Free body diagram for hovering flight

The forces in z-direction can be summed:

$$\sum F_z = L + T + L_h + T_h - W = 0 \quad (6.15)$$

With the following known variables:

$$L = \frac{1}{2} \rho V^2 S C_L$$

$$L_h = \frac{1}{2} \rho V_h^2 S_h C_{L_h}$$

$$W = (m_{\text{kite}} + m_{\text{tether}})g$$

The thrust in the tail rotor will be used for stability only. Hence, the required thrust in the main rotors is dependent only on the difference between the weight and the lift produced:

$$T = W - L - L_h \quad (6.16)$$

Moment equilibrium about the centre of gravity is calculated. Next, a non-dimensionalised equation is found by dividing by $\frac{1}{2}\rho V^2 S \bar{c}$:

$$\sum M_y = M_{ac} + L(x_{cg} - x_{ac}) + T(x_{cg} - x_{prop}) - T_h(x_h - x_{cg}) - L_h(x_h - x_{cg}) \quad (6.17)$$

$$C_m = C_{mac} + C_L \left(\frac{x_{cg} - x_{ac}}{\bar{c}} \right) + \frac{T}{\frac{1}{2}\rho V^2 S \bar{c}} \left(\frac{x_{cg} - x_{prop}}{\bar{c}} \right) - \frac{T_h l_h}{\frac{1}{2}\rho V^2 S \bar{c}} - C_{L_h} \frac{S_h l_h}{S \bar{c}} \quad (6.18)$$

Equilibrium is satisfied for $C_m = 0$. One can see that a trimmed condition can be obtained by adjusting the elevator and obtaining the required tail lift, or otherwise by generating more thrust with the tail propeller.

Required elevator deflection for equilibrium

To determine the required elevator deflection for equilibrium, the moment equation will be linearised:

$$C_m = C_{mac} + \frac{dC_L}{d\alpha} (\alpha - \alpha_0) \left(\frac{x_{cg} - x_{ac}}{\bar{c}} \right) + \frac{T}{\frac{1}{2}\rho V^2 S \bar{c}} \left(\frac{x_{cg} - x_{prop}}{\bar{c}} \right) - \frac{T_h l_h}{\frac{1}{2}\rho V^2 S \bar{c}} - \left(\frac{dC_{L_h}}{d\delta_e} \delta_e + \frac{dC_{L_h}}{d\alpha} (\alpha + i_h) \right) \frac{S_h l_h}{S \bar{c}} \quad (6.19)$$

Next the linearised moment equation will be written such that everything independent of α and δ_e is grouped together in C_{m_0} everything dependent on α is grouped under C_{m_α} , and finally the moment dependent on δ_e is represented by C_{m_δ} :

$$C_{m_0} = C_{mac} + \frac{T}{\frac{1}{2}\rho V^2 S \bar{c}} \left(\frac{x_{cg} - x_{prop}}{\bar{c}} \right) - \frac{T_h l_h}{\frac{1}{2}\rho V^2 S \bar{c}} \quad (6.20)$$

$$C_{m_\alpha} = C_{L_\alpha} (\alpha - \alpha_0) \left(\frac{x_{cg} - x_{ac}}{\bar{c}} \right) - C_{L_{h\alpha}} (\alpha + i_h) \frac{S_h l_h}{S \bar{c}} \quad (6.21)$$

$$C_{m_\delta} = -C_{L_{h\delta}} \delta_e \frac{S_h l_h}{S \bar{c}} \quad (6.22)$$

The tail thrust is set to zero so the elevator can be analysed separately. Rearranging and solving for δ_e :

$$\delta_e = \frac{1}{C_{m_\delta}} (-C_{m_0} - C_{m_\alpha} (\alpha - \alpha_0)) \quad (6.23)$$

Intuitively one can see that an elevator deflection will not be enough to keep the kite in equilibrium. Especially at low wind speeds the tail might not produce enough lift and additional thrust by the tail rotor will be used. The tail thrust in equation 6.19 is now set to nonzero and will be solved for:

$$T_h = \frac{\frac{1}{2}\rho V^2 S c}{l_h} (C_{m_0} + C_{m_\alpha} (\alpha - \alpha_0) + C_{m_\delta} \delta_e) \quad (6.24)$$

The above equations will be used in a MATLAB model to obtain values for the required elevator deflection. The input values are stated in table 6.7 they were obtained verbally during the intermediate design phase. The results can be seen in figure 6.10. The maximal deflection angle for the elevator was set to 20 degrees for mechanical reasons. As expected, a low amount of tail thrust is required to stabilise the kite for wind velocities at which the horizontal stabiliser is not effective. For wind speeds below $V_{w,ref} = 1$ m/s a maximum of about 12 N is needed.

Table 6.7: The input parameters for the required elevator deflection and tail rotor thrust

Parameter	Symbol	Value
Cg position	x_{cg}	0.6 [m]
Ac position	x_{ac}	0.458 [m]
Propeller position	x_{prop}	0.5 [m]
Tail length	l_h	4.1 [m]
Kite mass	m_{kite}	70 [kg]
Wing surface	S	12.7 [m ²]
Chord length	\bar{c}	1.347 [m]
Angle of attack	α	0 [deg]
Lift gradient	$C_{L\alpha}$	0.08827 [1/deg]
Lift coefficient $\alpha = 0$	C_{L0}	0.572 [-]
Moment coefficient ac	C_{mac}	-0.1992 [-]
Angle of incidence	i_h	-3 [deg]
Tail surface	S_h	1.91 [m ²]
Tail lift gradient	$C_{L_h\alpha}$	0.071 [1/deg]
Tail lift coefficient	C_{L_h}	-0.21 [-]
Elevator effectiveness [19]	$C_{L_{h\delta}}$	2.78 [1/deg]

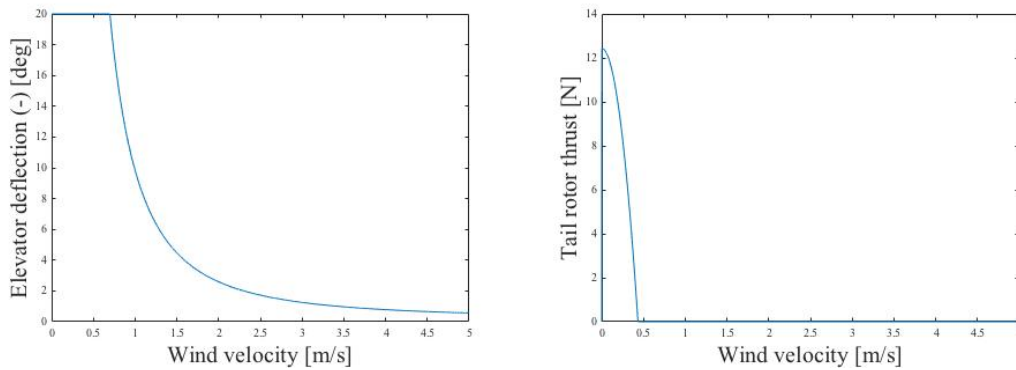


Figure 6.10: Elevator trim curve and required tail rotor thrust for equilibrium

6.2.3 Stability for hover

In the previous section the force and moment equilibrium for the kite modes was calculated. Now the conditions for equilibrium are known, and it has to be investigated whether the equilibrium is stable, i.e. does the kite return to its equilibrium condition for a small disturbance, or does the kite tip over. Hence, stability is defined as the ability to return to an equilibrium. In this subsection, stability for both the longitudinal and lateral directions are analysed.

Longitudinal static stability

For longitudinal stability, it is looked at what the kite behaves like for a small change in pitch. The kite is defined as stable if for an increase in angle of attack, there will be a counteracting pitch moment, i.e.:

$$\frac{dC_m}{d\alpha} < 0 \quad (6.25)$$

And we have the change in moment coefficient for a change in α from equation 6.19, consisting of the main

wing part and the stabiliser part:

$$C_{m_\alpha} = C_{L_\alpha} \left(\frac{x_{cg} - x_{ac}}{\bar{c}} \right) - C_{L_{h_\alpha}} \frac{S_h l_h}{S \bar{c}} \quad (6.26)$$

Combining the above equations results in:

$$\frac{x_{cg} - x_{ac}}{\bar{c}} < \frac{C_{L_{h_\alpha}} S_h l_h}{C_{L_\alpha} S \bar{c}} \quad (6.27)$$

From this equation it can be concluded that one needs a large tail volume, $\frac{S_h l_h}{S \bar{c}}$, or a centre of gravity that is close to the front of the aircraft to have a pitch stable aircraft. The point where c.o.g. and tail volume terms cancel each other out, is called the neutral point. In the neutral point, the kite is neutrally stable and $C_{m_\alpha} = 0$.

Using the values from table 6.7 and filling in in the above equation a negative C_{m_α} is obtained with value -0.0231. Hence it can be concluded that the kite is longitudinally, statically stable.

Lateral stability

According to Mulder et al. [9] the following lateral stability derivatives can be analysed:

- For sideslipping flight:

$$C_{Y_\beta} = \frac{\partial C_Y}{\partial \beta} \quad C_{l_\beta} = \frac{\partial C_l}{\partial \beta} \quad C_{n_\beta} = \frac{\partial C_n}{\partial \beta}$$

- For rolling flight:

$$C_{Y_p} = \frac{\partial C_Y}{\partial \frac{pb}{2V}} \quad C_{l_p} = \frac{\partial C_l}{\partial \frac{pb}{2V}} \quad C_{n_p} = \frac{\partial C_n}{\partial \frac{pb}{2V}}$$

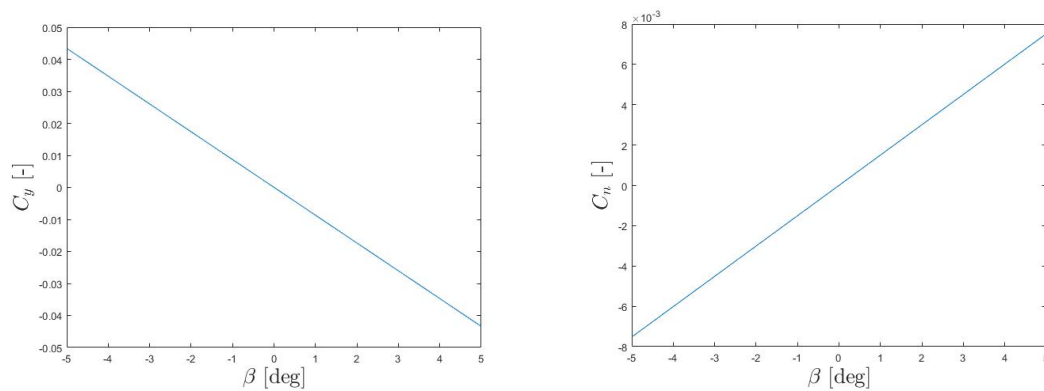
- For yawing flight:

$$C_{Y_r} = \frac{\partial C_Y}{\partial \frac{rb}{2V}} \quad C_{l_r} = \frac{\partial C_l}{\partial \frac{rb}{2V}} \quad C_{n_r} = \frac{\partial C_n}{\partial \frac{rb}{2V}}$$

The aforementioned stability derivatives are of importance for hover, since the kite needs stability for the entire flight envelope. An instability can result in a complete system failure and thus needs to be avoided. Not all stability derivatives are considered as important. Hence, the most critical derivatives need to be selected and analysed. Therefore it is chosen that stability in the roll direction is of secondary importance, due to the fact that the wing rotors can provide the necessary control for stability around the x-axis (roll stability). Hence, stability derivatives w.r.t. p , and also all rolling moment derivatives l are not analysed in this report. The remaining 4 stability derivatives are: C_{Y_β} , C_{n_β} , C_{Y_r} , and C_{n_r} .

- Of these stability derivatives C_{Y_r} signifies the change in lateral aerodynamic force due to yawing motion. However, the effect is usually negligibly small and most of the contribution comes from the vertical tail. According to Mulder et al. [9] it is usually of minor importance, hence it is assumed that this stability derivative does not destabilise the system.
- C_{n_r} is for normal configurations, i.e. the presence of a vertical tail, a measure of damping of the aerodynamic moment around the z-axis for a motion around the same axis. This stability derivative is determined to provide some stability to the yawing motion because the vertical tail provides the damping around the yaw-axis.

- $C_{Y\beta}$ is the measure of change in lateral aerodynamic for a change in β . A numerical calculation of $C_{Y\beta}$ was performed using XFLR5. The results can be seen in figure 6.11a. As expected $C_{Y\beta}$ is negative, this means that when the kite has a sideslip to the right, a force to the left will occur. It should be noted however, that in the numerical calculation the fuselage was not taken into account, hence one can expect a slightly less negative value in the real model.
- $C_{n\beta}$, or the **weather vane stability** is an important stability derivative, and is essentially for the lateral stability what $C_{m\alpha}$ is to longitudinal stability. For good control characteristics it is desirable that $C_{n\beta}$ causes a moment about the top axis that will reduce the sideslip angle, hence $C_{n\beta}$ should be positive. The largest stabilising part of $C_{n\beta}$ is the vertical tail, the fuselage will have a destabilising effect. Numerical values for $C_{n\beta}$ have been calculated using XFLR5 software, the results can be seen in 6.11b. It should be noted that in the calculations with XFLR5 the fuselage is not taken into account. Hence, the presented values are more positive than the expected real values. In conclusion, as far as this rather qualitative analysis goes the kite has lateral static stability.



(a) C_Y as a function of β for the aircraft w/o fuselage (b) C_n as a function of β for the aircraft w/o fuselage

Figure 6.11: The most important lateral stability derivatives, obtained using XFLR5

6.3 Control

The control of the rigid kite is an important area of design of the rigid kite. As the nominal flight trajectory of the kite during the reel-out phase includes flying a figure of eight trajectory, it is desirable that the kite is highly manoeuvrable. This means that the control surfaces of the kite should sustain the prescribed flight trajectory of the kite. Moreover, the rigid kite should also be able to pitch, yaw and roll as desired during climb and descent when the thrust from the main and tail rotors is used. This is desired when a change in pitch is required or to correct any disturbance from gusts. Therefore, the control analysis of the rigid kite is divided into two subsections 6.3.1 and 6.3.2.

6.3.1 Control in nominal flight

The control analysis in nominal flight is done based on the analysis conducted in report [19]. In this report, the control surfaces were sized based on the requirements for manoeuvres during nominal flight. The control characteristics of the rigid kite depend on the aerodynamic characteristics, rigid wing dimensions, control surface dimensions, and the flight conditions. As explained in chapter 5, the aerodynamic coefficients of the rigid kite remain largely unaltered to the DSE 2014 rigid kite. Furthermore, the control surface dimensions

Table 6.8: Difference in inertia properties of the DSE 2014 kite and the current rigid kite

Inertia Parameter	DSE 2014 kite	Current rigid kite	Relative ratio
m [kg]	44	75	1.7
I _{xx} [kg m ²]	76.05	398.58	5.3
I _{yy} [kg m ²]	44.88	162.87	3.6
I _{zz} [kg m ²]	48.49	518.38	10.7

and constraints are also carried forward from the previous design. The largest source of difference in the kite is the inertia properties of the kites. This is shown in table 6.8.

As table 6.8 shows, there is a relatively large difference between the inertia properties of the two rigid kites. The inertia properties of the original rigid kite are obtained from [19]. The inertia properties of the current rigid kite are obtained from the designed CATIA model. Finally, the relative ratio is defined as the ratio of the current inertia parameter over the DSE 2014 rigid kite inertia. Using the relative ratio factor, the effect on the control characteristics can be calculated.

The roll and aileron characteristics can be calculated based on the following equations. The time taken to achieve a desired bank angle is given by equation 6.28.

$$t_{\text{tot}} = t_1 + t_{\text{ss}} \quad (6.28)$$

In this equation, t_{tot} is the total time needed to reach a bank angle. The flight path desires a bank angle $\varphi_{\text{des}} = 90$ deg within 0.6 s. The time period t_1 is the time required to reach a steady roll rate φ_{ss} and t_{ss} is the time period to achieve bank angle in steady state roll. The equation can be further expanded to equation 6.29.

$$t_{\text{tot}} = \frac{\varphi_1}{P_{\text{Rss}}} + \frac{\varphi_{\text{des}}}{P_{\text{Rss}}} \quad (6.29)$$

In this equation, P_{Rss} is the steady state roll rate. Parameter φ_1 is defined by equation 6.30.

$$\varphi_1 = \frac{I_{\text{xx}}}{\rho y_{\text{D}}^3 S_{\text{tot}} C_{\text{DR}}} \ln \left((P_{\text{Rss}})^2 \right) \quad (6.30)$$

In this equation, S_{tot} is the total projected area of the wing planform and the empennage surfaces. Coefficient C_{DR} is the rolling drag coefficient and y_{D} is the distance between y_{cg} and the middle of the aileron surface. As mentioned previously, only the inertia properties of the rigid kite have changed. Thus, the time ratio for the roll between the current rigid kite and the DSE 2014 kite is given by equation 6.31.

$$\frac{t_{\text{tot,new}}}{t_{\text{tot,old}}} = \frac{5.3\varphi_{1,\text{old}} + \frac{\pi}{2}}{\varphi_{1,\text{old}} + \frac{\pi}{2}} \quad (6.31)$$

In report [19], the parameter φ_1 is not specified. Thus, it is difficult to obtain the exact relative ratio between the two time factors. However, it can be derived that to obtain the same t_{tot} required, other aileron characteristics must be changed. However, as the requirement of manoeuvre time is not justified in report [19], the aileron is not altered. Changes will need to be made when the manoeuvre requirements are clearly defined.

For the rudder and aileron design, the required deflections are small throughout the flight range. Therefore, the control surfaces do not need to be redesigned but can be deflected by a larger angle (still within 20 deg). Furthermore, the x_{dg} position has also moved closer to the leading edge and thus, the control surfaces need not be redesigned.

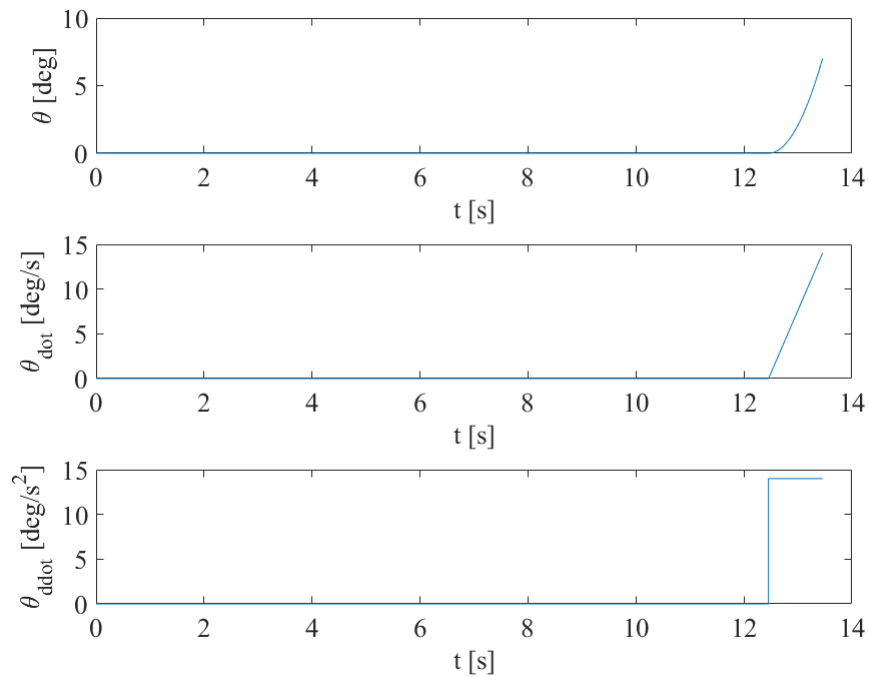


Figure 6.12: Pitch control for $V_{w,\text{ref}} = 6.8$ m/s climb phase

6.3.2 Control in climb

For the control characteristics required during climb, the main control input is the thrust output from the main rotors. In the current design, the thrust output is based on the motor characteristics. The motor can be modelled as a first order linear actuator; however, the required characteristics of the motor are not detailed from the manufacturer. Furthermore, it can be justified that the brushless motors are highly responsive and can be actively controlled using the autopilot system.

Another defined control characteristic during climb is the pitching response of aircraft. For example, the climb at $V_{w,\text{ref}} = 6.8$ m/s requires the aircraft to be pitched to $\vartheta = 5$ deg during a certain phase. In the climb model, the change in pitch is simulated as a jump. However, the change in pitch of the aircraft is not instantaneous. The pitch control of the rigid kite can be analysed based on the response for a change in thrust of the tail motor at different conditions. Figure 6.12, shows the pitch response of the rigid kite for a change in 10 N thrust from the tail rotor. As the figure illustrates, the change in tail rotor thrust causes a pitch angular acceleration $\vartheta_{\text{ddot}} = 14$ deg/s². The response is simulated for $t = 1$ s, and as shown, a pitch angle $\vartheta = 7$ deg is already achieved and the pitch rate ϑ_{dot} continues to increase linearly.

7 | Power & propulsion

This chapter will go over the thrust generation using rotors in order to perform the launching and landing manoeuvres. The chapter starts with the selection of the airfoil of the rotors in section 7.1. The design of the rotors using this airfoil is discussed in section 7.2. After this the motors needed to rotate the rotors at the right rpm and torque level are chosen in section 7.4. This then leads to the battery sizing in section 7.5 and the corresponding wiring required to reach the motors in section 7.6.

7.1 Airfoil selection

The airfoil selection is particularly important since it influences the thrust level that can be reached by the propellers. This is due to the fact that the airfoil characteristics determine the C_L and C_D at all angles of attack. These coefficients influence the magnitude of the lift and drag vector that are generated by moving the rotor through the air. The resultant of these two vector is the thrust vector and that is the one that determines the climb performance of the aircraft. This is clearly illustrated in figure 7.1¹.

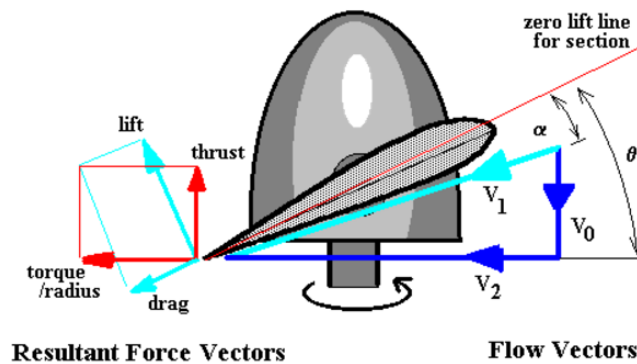


Figure 7.1: Generation of thrust by rotor blade

Three standard airfoils have been chosen to look at their lift and drag coefficient at zero angle of attack, as these are both used for the rotor size estimation. The Reynolds number that is used for comparison is 1,000,000 which is the maximum Reynolds number that can be analysed in the airfoil tool². The three airfoils that are considered as options are NACA 4412, NACA 2412 and Clark Y. The graphs showing the lift and drag coefficient versus the angle of attack are shown in figures 7.2, 7.3 and 7.4. Table 7.1 shows the C_{L_0} and C_{D_0} values for the three airfoils.

Based on the values in table 7.1, the NACA 4412 airfoil is chosen for the rotor. The C_{L_0} value is significantly higher than for the NACA 2412 and Clark Y airfoil, while there is not much difference in the C_{D_0} values.

Table 7.1: Lift and drag coefficients at zero angle of attack

Airfoil	C_{L_0}	C_{D_0}
NACA 4412	0.48	0.075
NACA 2412	0.24	0.06
Clark Y	0.4	0.06

¹Retrieved from: http://www-mdp.eng.cam.ac.uk/web/library/enginfo/aerothermal_dvd_only/aero/propeller/prop1.html [Accessed on 27-06-2017]

²Retrieved from: <http://airfoiltools.com/> [Accessed on 27-06-2017]

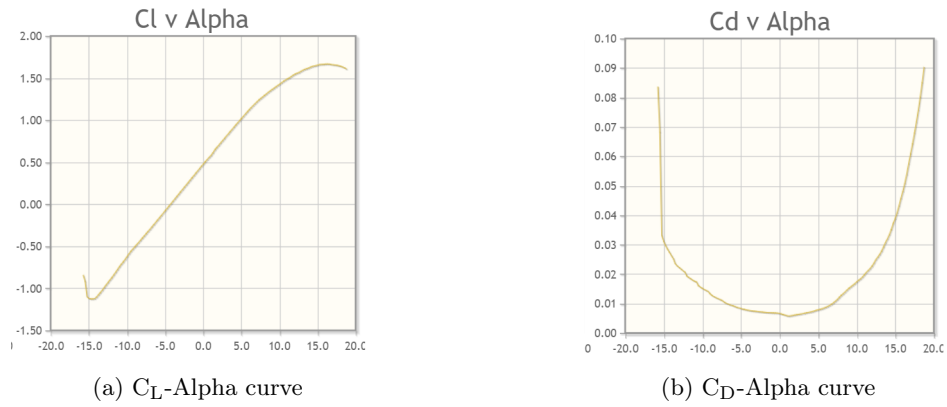


Figure 7.2: NACA 4412 airfoil

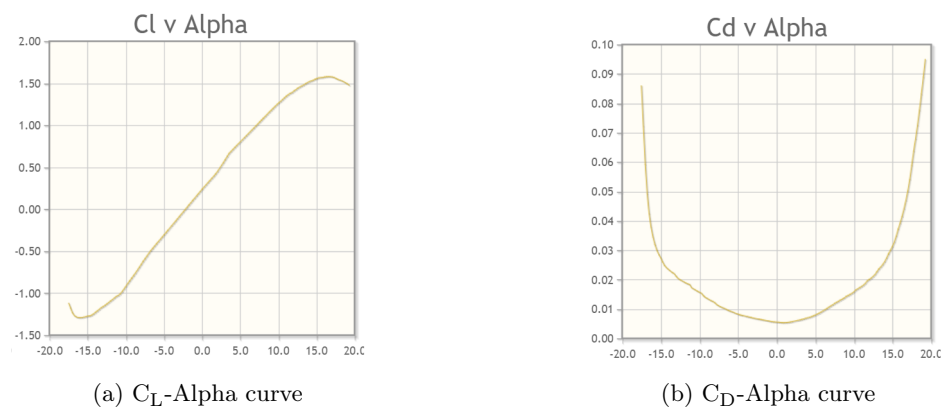


Figure 7.3: NACA 2214 airfoil

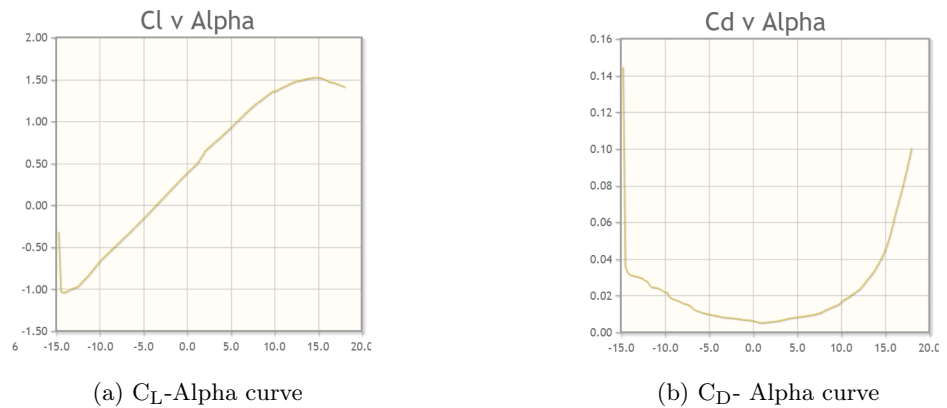


Figure 7.4: Clark Y airfoil

7.2 Main rotor sizing

In this section, the main reasoning behind the rotor sizing and the actual generation of the dimensions are shown. The fundamental equations and the model logic are explained, after which the sizing is performed.

7.2.1 Theory

In order to size the rotors, the Blade Element Theory (BET) [8] will be used. BET divides the rotor along the radius R in small pieces of dr . From momentum theory, also explained by Newman and Seddon [8], we obtain equation 7.1. As the thrust is provided and needs to be sized for, the required induced velocity will be equal to equation 7.2, where the positive solution is to be used. For all further calculations, uniform inflow is assumed.

$$T = 2\rho\pi R^2 V_i (V_c + V_i) \quad (7.1)$$

$$V_i = \frac{-V_c \pm \sqrt{V_c^2 - 2\frac{T}{\rho\pi R^2}}}{2} \quad (7.2)$$

If the blade is rotating with an angular velocity of Ω , each blade segment at location $x = r/R$ will experience two perpendicular velocities, namely the one coming from the incoming air ($V_c + V_i$) and its rotational velocity ($\Omega x R$). The inflow angle φ can now be determined with equation 7.3. For a certain angle of attack α , the corresponding pitch angle ϑ can then be determined with equation 7.4. It is chosen to use a linear twist distribution as shown in equation 7.5. Here, ϑ_0 will be 14° , which is chosen to be close to the stall angle of the NACA-4412 airfoil of 15° . In equation 7.5, k will be equal to $\vartheta_0 - \vartheta(1)$.

$$\varphi(x) = \tan^{-1} \left(\frac{V_c + V_i}{\Omega x R} \right) \quad (7.3)$$

$$\vartheta(x) = \varphi(x) + \alpha \quad (7.4)$$

$$\vartheta(x) = \vartheta_0 - kx \quad (7.5)$$

Similar to the way C_L and L are related, a thrust coefficient C_T can be used to determine thrust as depicted in equation 7.6. This thrust coefficient can be related to the geometry of the airfoil with use of equation 7.7. From Seddon and Newman [8], equation 7.7 can be reduced to equation 7.8. In equation 7.8, α_0 represents the zero lift angle of the airfoil and $\vartheta_{75\%}$ the pitch at $3/4$ of the radius. The inflow factor λ can be expressed, for hovering, with equation 7.9. Hovering can be considered as climbing flight will result in a higher thrust, following from equation 7.1.

$$T = \frac{1}{2} \rho (\Omega R)^2 \pi R^2 C_T \quad (7.6)$$

$$C_T = sa \int_0^1 \left((\vartheta - \alpha_0) x^2 - \lambda x \right) dx \quad (7.7)$$

$$C_T = sa \left(\frac{\vartheta_{75\%} - \alpha_0}{3} - \frac{\lambda}{2} \right) \quad (7.8)$$

$$\lambda = \frac{sa}{16} \left(\sqrt{1 + \frac{64}{3sa} \vartheta_{75\%} - 1} \right) \quad (7.9)$$

As the thrust coefficient can be determined when the thrust is known and the pitch distribution is determined independent of the thrust, equation 7.8 can be used to obtain the solidity factor s . The solidity factor is defined by 7.10. With use of equation 7.10, the chord and radius can be related to each other, when the amount of blades is predetermined.

$$s = \frac{Nc}{\pi R} \quad (7.10)$$

Similar to the C_T , a power coefficient C_P can be determined as well. The definition for C_P is shown in equation 7.11. If a constant profile is assumed, one ends up with equation 7.12. Here, k_i is an empirical factor, accounting for several losses such as tip loss, and usually has a value of 1.15.

$$C_P = \lambda d C_T + s C_D x^3 dx \quad (7.11)$$

$$C_P = k_i \lambda C_T + \frac{s C_{D0}}{4} \quad (7.12)$$

Finally, as $C_P = C_Q$, the Figure of Merit (FoM) M and the required torque Q can be determined using equation 7.13 and equation 7.14.

$$M = \frac{\sqrt{C_T^3}}{2 C_P} \quad (7.13)$$

$$Q = \frac{1}{2} \rho (\Omega R)^2 \pi R^2 C_Q \quad (7.14)$$

7.2.2 Execution

Using the equations presented in subsection 7.2.1, a sizing tool was established. Large arrays of different radii, angular velocities and linear pitch distributions were combined with several inputs, ending up with the FoM for every combination of these three parameters. From all these efficiencies, the combination which resulted in the maximum will be selected and serve as output for the model. A list of in and outputs is shown in table 7.2 and the program logic is shown in figure 7.5 and described below.

When the program is initialised, several arrays are created. These consist of ranges of values for R , Ω and $\vartheta_{75\%}$, as well as a detailed grid in x , ranging from 0 to 1. Using the flight path parameters V_c , T and ρ , the required thrust coefficient can be determined for combinations of R and Ω . With use of ϑ_{75} and α_{stall} , the pitch distributions will be determined. Combined with C_T , Newtons method³ is used to determine s and c subsequently. These chords are filtered to lie within a certain range of aspect ratios to remove unfeasible options, after which the power coefficient is determined. Combining C_P with C_T results in the figure of merit and the torque for each option.

Table 7.2: Input and output parameters for the rotor size model

Inputs	Outputs	Airfoil characteristics
T	M	C_{D0}
ρ	R_{opt}	$C_{L\alpha}$
N	Ω_{opt}	α_0
AR_{min}	$\vartheta(x)$	α_{stall}
AR_{min}	c	–
–	Q	–

7.2.3 Results

Using the sizing tool, presented in subsection 7.2.2, the relevant input parameters were inserted and the program was run. The inputs that were used for the sizing and the ranges for the arrays are presented in tables 7.3a and 7.3b respectively. The thrust for which the sizing is done follows from section 6.1 and was found to be 437 N per rotor.

³Retrieved from: <https://www.math.ubc.ca/~anstee/math104/104newtonmethod.pdf> [Accessed on 27-06-2017]

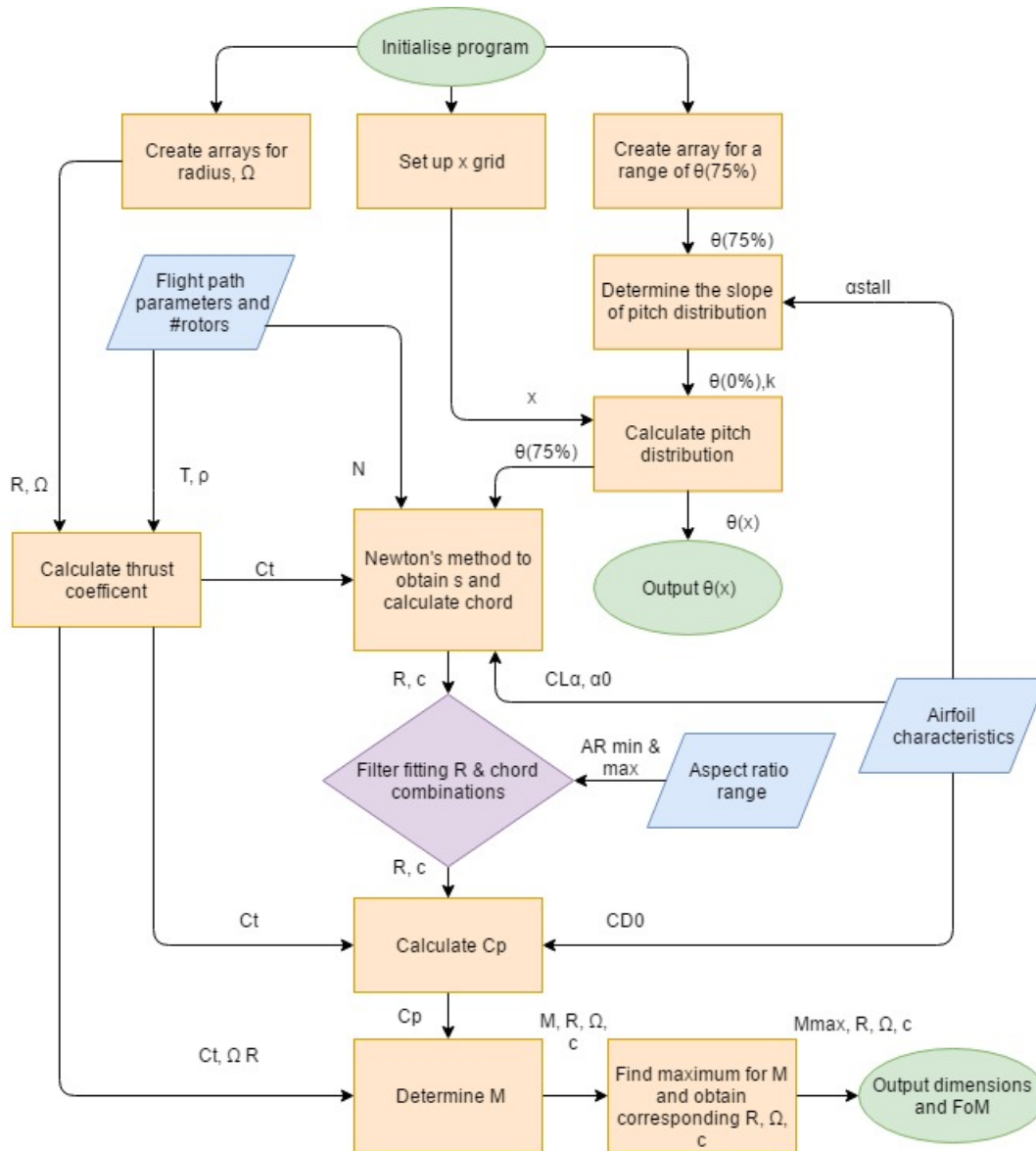


Figure 7.5: Flowchart of the model to size the propellers

Combining these results with the airfoil data for NACA 4412⁴, the geometry and rpm setting resulting the right amount of thrust and highest figure of merit. These airfoil characteristics and corresponding outputs are shown in tables 7.4a and 7.4b respectively.

7.3 Tail rotor sizing

The tail rotor is essential for the stability during lift-off of the kite. On top of that allows the third rotor three axis control of the kite, this is important to correct for disturbances and to manoeuvre the kite into the right position to start nominal operation. On top of providing the lifting thrust and control force the

⁴Retrieved from: <http://airfoiltools.com/airfoil/details?airfoil=naca4412-il> [Accessed on 27-06-2017]

Table 7.3: All relevant inputs for the model presented in figure 7.5

(a) Input values that are used in the model

Input	Value
T	437 [N]
ρ	1.225 [kg/m ³]
N	2 [-]
AR _{min}	5.0 [-]
AR _{max}	15.0 [-]

(b) Arrays that are used in the model. All arrays had a size of 201 datapoints

Quantity	Minimum	Maximum
R	0.4 [m]	1.0 [m]
Ω	2500 [rpm]	5000 [rpm]
$\vartheta_{75\%}$	1.0 [deg]	9.0 [deg]
x	0.0 [-]	1.0 [-]

Table 7.4: Obtained rotor geometry with the NACA 4412 airfoil

(a) Airfoil characteristics for the NACA 4412 airfoil

Quantity	Value
C _{D0}	0.0068 [-]
C _{Lα}	5.7 [1/rad]
α_0	-0.0742 [rad]
α_{stall}	0.2618 [rad]

(b) Output parameters for the rotor geometry and corresponding rpm setting

Output	Value
R	0.538 [m]
c	0.0556 [m]
Ω	4750 [rpm]
$\vartheta(x)$	14 - 6.6667x
M	0.7438 [-]
Q	16.77 [Nm]

tail will be used for on board power generation.

7.3.1 On board power generation

The design of the tail rotor started with sizing it for power production. Equation 7.15 gives the relation between power output P_a and the swept area A of the generator.

$$P_a = \frac{1}{2} \rho A V^3 C_P N \varepsilon \quad (7.15)$$

This relation can be derived from the formula for kinetic energy including efficiency factors [16]. C_P is 0.59 and this factor is the maximum power that can be extracted from a flow, this limit is known as the Betz limit [17]. It is assumed that 75% of the Betz limit can be reached by this propeller given by the factor $N = 0.75$. ε is the efficiency of the full system including the motor that needs to generate the electricity, cable losses and battery losses ε and was estimated to be 0.7. To ensure that enough power is produced in all cases the propellers were sized for a minimum velocity of 6.8 m/s at 100 m altitude. For this wind speed according to the power model in section 3.7 the kite velocity will be no less than 30 m/s. Equation 7.16 is the rewritten version to give the relation for determination of the radius.

$$r_t = \sqrt{\frac{2P_a}{\rho V^3 C_P \pi N \varepsilon}} \quad (7.16)$$

As the power budget was estimated in table 3.4 the needed on board power during nominal operation is 69.89 W. Using all inputs for equation 7.16 the required radius is 6.87 cm. This is far below the required radius that is required to perform take-off and landing. As the power production is not the design driver for the tail rotor the sizing was further determined in section 7.3.2 based on the required thrust.

7.3.2 Tail rotor dimensions

Since the on board power generation requires a small radius as minimum for the tail rotor, the dimensions will be sized for the required thrust based on the stability requirement. The model, as described in section 7.2, will be used. The thrust required by the tail rotor was described in section 6.1, and was equal to 70 N. The input parameters and array dimensions are given in tables 7.5 and 7.5b respectively. With use of the model and the NACA 4412 airfoil, the tail rotor was sized. The airfoil characteristics and the solution to the sizing are shown in table 7.6a and 7.6b respectively.

Table 7.5: All relevant inputs for the model presented in figure 7.5

(a) Input values that are used in the model

Input	Value
T	70 [N]
ρ	1.225 [kg/m ³]
N	2 [-]
AR _{min}	5.0 [-]
AR _{max}	15.0 [-]

(b) Arrays that are used in the model. All arrays had a size of 201 datapoints

Quantity	Minimum	Maximum
R	0.1 [m]	0.6 [m]
Ω	2500 [rpm]	7000 [rpm]
$\vartheta_{75\%}$	1.0 [deg]	9.0 [deg]
x	0.0 [-]	1.0 [-]

Table 7.6: Obtained tail rotor geometry with the NACA 4412 airfoil

(a) Airfoil characteristics for the NACA 4412 airfoil

Quantity	Value
C _{D0}	0.0068 [-]
C _{Lα}	5.7 [1/rad]
α_0	-0.0742 [rad]
α_{stall}	0.2618 [rad]

(b) Output parameters for the tail rotor geometry and corresponding rpm setting

Output	Value
R	0.31 [m]
c	0.0323 [m]
Ω	6825 [rpm]
$\vartheta(x)$	14 - 6.6667x
M	0.7438 [-]
Q	2.1872 [Nm]

7.4 Motor sizing

This section will describe how the electric motors were sized, both the main motors as the tail motor will be covered. First the parameters needed to decide the motor size will be pointed out. Next the choice for the type of motor will be explained and finally the exact specifications of the motor will be given.

7.4.1 Type of motor

Considering the motor will be powered by batteries will be a direct current motor. Long life and low maintenance are important characteristics the motor should have, as well as a high efficiency. This leads to the conclusion that brushless direct current (BLDC) motors will be used for all three rotors.

BLDC's can be distinguished in 'outrunners' and 'inrunners'. In outrunner type motors the outer casing contains the permanent magnets and thus functions as the rotor. For inrunners it is the other way around, the outer casing is the stator. Inrunners can reach very high rpm's but provide limited amounts of torque, outrunners on the other hand have lower rpm's but can provide far greater amounts of torque. The high torque enables the direct drive of a propeller without the use of a gearbox which would decrease efficiency.

The turning of the relatively large propellers will require a large torque so a outrunner type BLDC will be used.

7.4.2 Required power

The power required to drive the rotors consists of four parts: parasite power P_{par} , ancillary power P_{a} , profile power P_{p} and induced power P_{i} .

Parasite power is the power needed to move the airframe through the air. Ancillary power is the power needed to drive any ancillary items like alternators etc. The profile power is the power required to turn the rotors, the power to overcome the profile drag from the rotor blades. The induced power is the power needed to produce the actual lift. Considering the motors only propel the rotors and no other items, P_{a} can be neglected. Parasite power P_{par} is equal to the drag force multiplied by the speed the airframe travels. The speed in this case is the climbing speed which will be small thus P_{par} is neglected. All that remains is profile power P_{p} and induced power P_{i} . The induced power and profile power can be calculated using equation 7.17 and 7.18 respectively, both from [8]. The total required power is calculated using equation 7.19.

$$P_{\text{i}} = \sqrt{\frac{\left(\frac{T}{2}\right)^3}{2\rho A}} \quad (7.17)$$

$$P_{\text{p}} = \frac{1}{8} C_{D0} \rho A V_{\text{tip}}^3 \sigma \quad (7.18)$$

$$P_{\text{total}} = k_{\text{i}} P_{\text{i}} + P_{\text{p}} \quad (7.19)$$

The required power calculated above is equal to the mechanical power that needs to be produced by the motor, a safety factor of 1.5 will be used to ensure the motor does not run at full power when it is operational. If the motor runs at full power for extended periods of time it will heat up excessively which will impact the lifetime of the motor. At 80° C the magnets start losing their magnetism which will impact the power the motor can produce. The safety factor of 1.5 means about 67% of the power will be used during normal operation leaving some margin for an incidental need of more power such as during high wind conditions or aggressive manoeuvring.

The power required for the main motor and the tail motor is shown in tables 7.7a and 7.7b.

Table 7.7: Power required for the tail and the main rotor

(a) Power required for main rotor

Parameter	Watt
P_{p}	1194
P_{i}	6120
Total	8232
Total (incl. S)	12349

(b) Power required for tail rotor

Parameter	Watt
P_{p}	132
P_{i}	1153
Total	1458
Total (incl. S)	2188

7.4.3 Motor selection

It has to be taken into account that the max or peak power advertised by the manufacturers is not the output power, it is the max input or electrical power consumed by the motors. This amount of power can only be consumed for short bursts because of the high amounts of current necessary which will raise the motor temperature to dangerous levels. Most manufacturers advice to run the motors at max power for 15 to 30 seconds.

The amount of power the motor can handle continuously can be approximated by multiplying half of the no load rpm of the motor with half of the stall torque.⁵

These values can be related to the max voltage and max current through the known voltage and torque constants k_v and k_q .

Based on this the R-snake 154 and Hacker Q80-6L V2 were chosen, the R-snake should be able to handle 9kW continuously while the hacker should be able to handle 1.73 kW.

As a check of motor performance the amount of torque produced by the motor will be calculated and compared to the load the propeller puts on the motor. The amount of revolutions per minute the motor can turn under load will also be compared because the propeller will need to reach this speed to produce enough thrust. These characteristics will be calculated next for the selected motors. The torque can be calculated using equations 7.20 and 7.21 from ⁶ where and I_0 is the no-load current.

$$k_q = \frac{30}{\pi k_v} \quad (7.20)$$

$$Q_{\max} = k_q(I_{\max} - I_0) \quad (7.21)$$

The amount of rpm a motor can reach under load is calculated using equation 7.22 where $\text{rpm}_{\text{no load}}$ is the max rpm without a load, Q_{load} is the torque of the load and Q_{max} is the max torque the motor can produce without load.

$$\text{rpm}_{\text{load}} = \frac{Q_{\text{load}}}{Q_{\text{max}}} \text{rpm}_{\text{no load}} \quad (7.22)$$

The results of these calculations can be found in table 7.8. Both the R-snake and the Hacker can produce enough power to spin the propeller at their respective speeds. According to the calculations the R-snake will consume slightly more than recommended continuous power but nowhere near the point where it will consume max current.

Table 7.8: motor stall torque and rpm under load

Motor	Unit	154	80
U	[V]	90	44
I	[A]	400	157
k_v	[rpm/V]	80	180
k_q	[nm/A]	0.1194	0.0530
Q_{stall}	[Nm]	47.75	7.172
rpm_{drop}	[rpm]	2494	1701
rpm_{load}	[rpm]	4706	6219

7.4.4 Motor Specs

The motor chosen as main motor is the R-Snake 154 Series ⁷, data is shown in table 7.9a. The motor chosen as tail motor is the Hacker Q80-6L V2 ⁸, data is shown in 7.9b.

⁵Retrieved from: http://www.microprivod.ru/catalogue/pdf/faulhaber/EN_Technical_Information_Rev3.pdf

⁶Retrieved from: <http://www.micromo.com/technical-library/dc-motor-tutorials/motor-calculations> [Accessed on 27-06-2017]

⁷Retrieved from: <http://www.ebay.com/itm/Outrunner-Brushless-Motor-154Series-35Kw-Paramotor-Electric-Prototypes-Big-Drone-/262633139334?hash=item3d2627ac86:g:62YAAOSw0j9ZP4Mw> [Accessed on 27-06-2017]

⁸Retrieved from: https://www.hacker-motor-shop.com/Brushless-Motors/Hacker-Q80/Q80-6L-V2.htm?shop=hacker_e&a=article&ProdNr=37418019&p=2986 [Accessed on 27-06-2017]

Table 7.9: Motor Data

(a) Main motor data		(b) Tail motor data	
Parameter	Unit	Parameter	Unit
Make	R-Snake	Make	Hacker
Model	154 series	Model	Q80-6L V2
K_v	80 [rpm/V]	KV	180 [rpm/V]
Max power	35 [kW]	Max power	6908 [W]
Max Voltage (# cells)	90 [V] (22 [s])	Max Voltage (# cells)	44 [V] (12 [s])
Max Current	400 [A]	Max Current	157 [A]
Size (d x h)	154 x 69.5 [mm ²]	Size (d x h)	88.5 x 89.3 [mm ²]
Weight	3.200 [kg]	Weight	1.335 [kg]

7.4.5 Electronic Speed Control

The electronic speed control or ESC is a small electronic circuit connected to the motor, its purpose is to vary the motors speed as well as its direction of rotation. The ESC can also function as a dynamic brake. Considering the motor has a max voltage of 90V the ESC has to be compatible with 22 LiPo cells. It is recommended to use an ESC that is rated at a current 20% higher than the max motor current, to prevent the ESC from limiting motor performance when max current is required. The ESC chosen for the main motor is the R-Snake 440A ESC 72-MOSFET, its specs are shown in table 7.10a.⁹ For the tail motor the Hacker MasterSPIN 170 Pro Opto is chosen, specs are shown in table 7.10b.¹⁰

Table 7.10: ESC data

(a) Main motor ESC		(b) Tail motor ESC	
Parameter	Unit	Parameter	Unit
Make	R-Snake	Make	Hacker
Model	440A ESC 72-MOSFET	Model	MasterSPIN 170 ProOpto
Size	160 x 160 x 35 [mm ³]	Size	120 x 63 x 27 [mm ³]
Weight	0.87 [kg]	Weight	0.34 [kg]

7.5 Battery sizing

To be able to use the motors, they need a power source that generates enough power for a certain period of time to perform the climb and the descent. This will be done by a pack of batteries attached to the aircraft. The battery does not have to provide power for the nominal flight phase since this is delivered by the tail rotor (section 7.3). The batteries are charged at the ground station every time it lands due to wind conditions or required maintenance.

⁹Retrieved from: http://www.ebay.com/itm/440A-ESC-AIR-22S-90V-R-Snake-72-Mosfet-Version-to-Airplane-or-Paramotor/262946069822?_trksid=p2047675.c100009.m1982&_trkparms=aid%3D888007%26algo%3DDISC.MBE%26ao%3D1%26asc%3D44732%26meid%3Daba0088fded549c5b3b4024ed820ea77%26pid%3D100009%26rk%3D1%26rkt%3D1%26sd%3D262942664548 [Accessed on 27-06-2017]

¹⁰Retrieved from: https://www.hacker-motor-shop.com/Speed-controller/MasterSpin-Pro/MasterSPIN-170-Pro-OPTO.htm?shop=hacker_e&SessionId=&a=article&ProdNr=52007010&p=5583&rdeocl=1&rdeopl=productpage&rdebox=b ox1 [Accessed on 27-06-2017]

7.5.1 Energy

The energy that the batteries need to be able to provide should be enough to rotate the rotor blades at the required rotational speed. If they do, the rotors create the lift that is needed during launch and hovering. To get the total energy that the battery has to be able to provide, the time the different manoeuvres take has to be known. This has to be multiplied with the power required for the different stages to arrive at the total energy needed. This can be split up into climbing and descending, which both have their own corresponding manoeuvres. The climbing phase takes 68 seconds and the descent takes 60 seconds. To counteract the rotor drag during climb, the two main motors operate at 8.2 kW each for 68 seconds, which is a total power of 16.5 kW. The tail will need to provide stability for the first 30 m upwards while the aircraft is only climbing vertically.

After this the third rotor starts producing more lift at a power of 1.56 kW, in a different direction, to be able to perform the manoeuvre that also covers horizontal distance, eventually reaching the desired final position. This manoeuvre takes much longer than the first 30 m; therefore the tail rotor is assumed to produce 1.56 kW for the full 68 seconds. For the hovering descent the main rotors need to produce practically the same amount of power as for the climb, 16.5 kW for 60 seconds. The tail rotor also needs a similar amount of power to be able to guide the aircraft to the landing spot, 1.56 kW for 60 seconds. Figure 7.6 shows the relatively straightforward energy load profile of the climb and descent. Calculating the surfaces of the two parts gives a total required energy of 2.31 MJ.

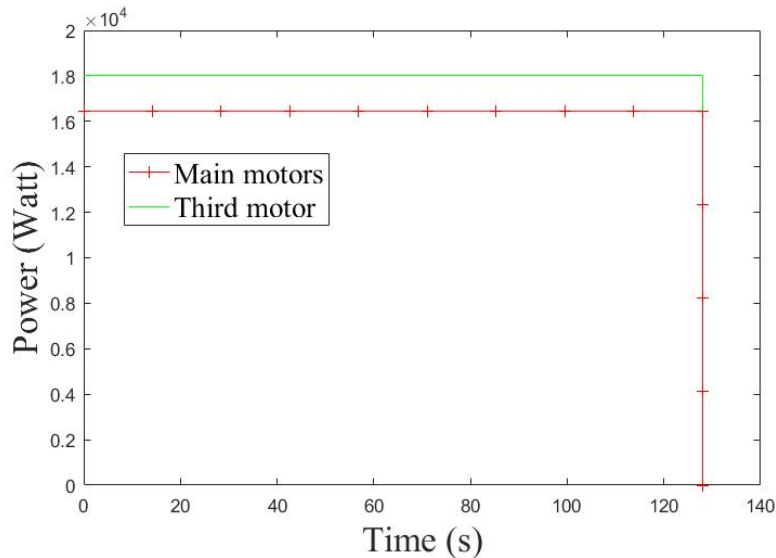


Figure 7.6: Energy load profile

Another aspect that needs to be taken into account is that the batteries have some factors that compromise their performance. These factors are the depth of discharge, the ageing factor and the high discharge rate at which it is performing. The lower the energy levels to which batteries are discharged, the shorter their lifetime. To ensure a lifetime that fits the system, a depth of discharge of 80 % is chosen; this leads to a lifetime of at least 400 cycles.¹¹ Assuming that the aircraft needs to be taken down once every two days, the battery lasts about two years. The ageing factor in the conditions in which it will operate is 0.96 for one year¹⁰, which leads to an ageing factor of 0.92 for two years. Last but not least, the high discharge rate at which the battery will be performing has a large impact on the capacity it will be able to deliver. This

¹¹ Retrieved from: http://batteryuniversity.com/learn/article/how_to_prolong_lithium_based_batteries [Accessed on 27-06-2017]

capacity is halved ¹² at very high discharge rates and therefore another factor of 2.0 needs to be added to the required energy the battery can store. Multiplying these three correction factors with the total energy and power gives the values shown in table 7.11.

7.5.2 Battery specifications

After the power and energy have been determined, these can be linked to certain battery specifications. The chemical aspects of designing a battery lie outside the scope of this research, but the specifications that are needed for choosing a commercial battery are of interest.

$$C\text{-rate} = \frac{3600}{t_{\text{discharge}}} \quad (7.23)$$

$$Q = \frac{E}{U_{\text{total}}} \quad (7.24)$$

$$\text{No. of cells} = \frac{U_{\text{total}}}{U_{\text{cell}}} \quad (7.25)$$

The material of the battery is of utmost importance to its performance. The most state-of-the-art battery technology focuses on Lithium-Ion and Lithium-Polymer batteries. These have the highest specific density, which is the power per kilogram of battery. Since the aircraft is extremely light-weight and every added kilogram has a relatively large impact, reaching a low weight of the battery is the most important requirement. Therefore, Lithium-Ion or Lithium-Polymer batteries will be used. From the motor requirements, it is taken that the total voltage of the batteries should be equal to 90 V (section 7.4). Lithium batteries have a standard nominal voltage of 3.7 V per cell ⁵. Using this information as inputs, the list of simple equations 7.23, 7.24 and 7.25 is used to arrive at the values shown in table 7.11. The C-rate is the rate at which the battery discharges. A C-rate of 1 discharges the battery in an hour, while a C-rate of 2 discharges the battery in 30 minutes.

Table 7.11: Battery parameters

Parameter	Value
Total energy	6.27 [MJ] or 1.74 [kWh]
Voltage	90 [V]
Power	46.1 [kW]
C-rate	28
Capacity	19.35 [Ah]
No. of cells	24

7.5.3 Choice of battery

The choice of battery mainly depends on the voltage that is needed for the motors and its corresponding amount of battery cells needed and the total energy required to perform all manoeuvres. It is possible to choose a combination of off-the-shelf battery packs or assemble one based on the requirements. The latter one is the preferred option, since that gives more freedom in designing a battery that fits precisely to the system needs.

The battery material that is used for the battery is Lithium Manganese Oxide (LMO)¹³. This type of Lithium Ion has as advantages that it has a relatively high specific energy, 125 Wh/kg, and can also reach discharge

¹²Retrieved from: http://www.engineersedge.com/battery/discharge_rate_temperature_effects_battery.htm [Accessed on 27-06-2017]

¹³Retrieved from: http://batteryuniversity.com/learn/article/types_of_lithium_ion [Accessed on 27-06-2017]

rates that are high enough. Compared to Lithium-Polymers it is known to have a lower risk of causing fires, which is essential for an autonomous system. Also, there is much more literature and experience available on Lithium-Ion batteries which makes self-production more convenient.

Most of the requirements for the batteries are specified in table 7.11. If one takes 2 battery packs of 12 LMO cells and places those in series, the total amount of cells and voltage is reached. LMO has a maximum discharge rate of 30C and therefore meets the 28C requirement. Each battery pack will be made of 6.96 kg of LMO; this results in a total amount of watt hours per pack of 871 Wh, resulting in the required total amount of 1.74 kWh. Another aspect that has to be taken into account is that the motors need 450 A for maximum power output, which might be needed during wind gusts. Dividing the amount of watt hours by the voltage, gives a capacity of 19.62 Ah. Multiplying this with the maximum discharge rate of 30C gives 589 A, which is enough for maximum power output of the motors if needed. The mass of the material of the LMO itself will not be enough to assemble a working battery; therefore, an extra 30% is taken for the wiring, attachments and coatings.

The costs of the battery are determined based on the price of LMO, which is equal to 12.5 €/kg¹⁴. This leads to a battery material price of €174. The electronics and coatings needed to assemble the battery is assumed to add an extra 40 % on top of the material costs. This leads to a total price of €243.6. The properties of the battery are summarised in table 7.12; some of the values overlap with the values in table 7.11.

Table 7.12: Battery specifications assembled battery

Parameter	Value
Total energy	6.27 [MJ] or 1.6051 [kWh]
Voltage	88.8 [V]
Max. Current	589 [A]
Power	49 [kW]
Max. C-rate	30
Capacity	19.62 [Ah]
No. of cells per pack	12
No. of packs	2
Total battery mass	17.98 [kg]
Costs	€243.6

7.6 Wire sizing

The electric current needs to be directed from the batteries to the motors using wires. It is important to keep them as small and light as possible, since they need to cover distance along the entire span and length of the kite to reach the motors.

7.6.1 Wire specifications

The material used for the wires needs to be a very good conductor; the two main options for this are copper and aluminium. There are materials that are better conductors. However, due to their relatively low cost and abundance, copper and aluminium are the common choices. Copper is the most widely used option for wires and has the advantages that it is easy to produce and has a high tensile strength. Aluminium is less widely used due to the fact that it expands and contracts while warming up and cooling down. This may cause loosening of the connections if not installed properly, potentially leading to fire outbreak.¹⁵ However,

¹⁴Retrieved from: https://www.alibaba.com/product-detail/Ideal-Battery-Cathode-Material-Lithium-Manganese_60576706732.html?s=p [Accessed on 27-06-2017]

¹⁵Retrieved from: <http://www.edisontechcenter.org/wires.html> [Accessed on 27-06-2017]

aluminium has a much lower density than copper, which can lead to wires with 60 % less mass. Furthermore, the Airbus A380 uses aluminium wires in the entire aircraft, which shows that the safety risk is negligible when installed correctly.¹⁶ Another advantage is that aluminium is much less costly than copper. Taking all of these arguments into account, aluminium will be used as material of the wire.

The next step is sizing the wires; this is done according to the American Wire Gauge (AWG) system. The value of the current that the wire is going to conduct is the leading factor that determines the size. If the current is higher than the wire gauge can handle, there is a danger of fire. However, it is possible for a wire gauge to handle currents that are lower than the maximum value for which it is defined.¹⁷ The AWG value is based on the requirements specified by the ESC manufacturer, since the wires need to run from the batteries to the ESCs located at the motors. The value for the ESC at the main motors is 8 AWG¹⁸. For the tail ESC this data is not available; however, since it requires a lower current than the main motor ESCs a conservative estimate of 8 AWG wire size is deemed more than sufficient. Equation 7.26 shows how this is converted to wire diameter. The 'n' in the equation is in this case equal to 8.

$$d = 0.127 \cdot 92^{\frac{36-n}{39}} \quad (7.26)$$

The three motors are parallel, which means that the current each wire needs to be able to handle is one third of the total current. This gives a diameter of 3.26 mm.

Table 7.13: Wire characteristics

Parameter	Value
Material	Aluminium
Diameter	3.26 [mm]
Area	8.37 [mm ²]
Volume	258,466 [mm ³]
Total Mass	0.7 [kg]
Price	€2.28 ¹⁹

The length of the cable depends on the distance it has to cover. The battery will be installed at the nose of the aircraft, the two main motors at the wingtips and the tail rotor at the front of the vertical tail. The distance from the nose to the main rotors is equal to half the wing span: 5 m. The wire will run through the wing, in the space between the wingbox and the leading edge. Due to the taper of the wing, the length of the wire to reach one motor is estimated to be 5.5 m. The distance between the nose of the aircraft and the tail rotor is equal to 4.44 m. The ESCs and motors need to be connected with a positive and negative wire. This means that the total length of the wires is equal to 30.88 m. Using this length, the wire diameter and an aluminium density of 2712 kg/m³²⁰ gives the wire characteristics shown in table 7.13.

¹⁶Retrieved from: http://www.helukabel.com/publication/us/technical_articles/aluminum-vs-copper-8-11-15.pdf [Accessed on 27-06-2017]

¹⁷Retrieved from: <https://www.thespruce.com/what-size-electrical-wire-is-needed-1152865> [Accessed on 27-06-2017]

¹⁸Retrieved from: <http://www.ebay.com/itm/440A-ESC-CAR-16S-R-Snake-72-Mosfets-to-1-5-Brushless-Motor-FG-5ive-Baja-/262946131586> [Accessed on 27-06-2017]

²⁰Retrieved from: http://www.engineeringtoolbox.com/metal-alloys-densities-d_50.html [Accessed on 27-06-2017]

8 | Structures

This chapter describes the main structural components of the system. First, the main elements of the ground station that are specific for each different AWES are discussed in section 8.1. Secondly, the five main structural components of the kite are analysed and (re)designed in section 8.2.

8.1 Ground station

The ground station exists out of multiple elements. The main elements that need further research are the tether and drum; these two elements are highly correlated. Chapter 33 of [22] describes a method to come up with values for the diameters of the tether and drum. However, for this method an initial value for the tether diameter is chosen. In this section it is chosen to start with a desired life time and come up with corresponding values for the tether and drum diameters. The characteristics shown in table 8.1 are used for the calculations. The AWE system characteristics (table 8.1a) are calculated with the power model described in chapter 3. The multiplication factors (table 8.1b) are taken from [22].

Table 8.1: Relevant values for tether and drum calculations

(a) AWE system characteristics		(b) Multiplication factors	
Description	Value	Factors	Value
Reel-out force	16462 [N]	Design factor	3
Tether length	700 [m]	Coating content	0.1
Cycle time	151.6 [s]	Loading factor	1.72
Reel-in time	18.6 [s]	Day/night (temperature) factor	1.50
Reel-out time	123 [s]	Seasonal (temperature) factor	1.51
Transition time	10 [s]	Improvement SK75 to SK78	3
		Improved tether construction	2

Note that since it concerns the determination of fatigue and therefore the impact of daily use, the average reel-out force is taken. By rewriting equation 33.7 from [22] and deciding on a Safe Service Life (SSL) the Cycles To Failure (CTF) can be calculated with equation 8.2. However, keeping in mind that the life time can be increased by a factor 2 (improved tether construction) and 3 (improvement from SK75 to SK78) the desired life time need to be divided by these two factors in order to get the Safe Service Life.

$$SSL = \frac{\frac{CTF}{1.33} \cdot \text{cycle time}}{\text{number of sheaves}} \quad (8.1)$$

$$CTF = \frac{SSL \cdot \text{number of sheaves} \cdot 1.33}{\text{cycle time}} \quad (8.2)$$

After calculating the CTF a relation can be shown (figure 8.1a) between the drum/tether diameter ratio D/d and the stress experienced by the tether. This relation is composed out of data of figure 33.17 and the corresponding table 33.5 from [22].

For each stress, and corresponding D/d ratio, the tether diameter can be calculated by knowing the Minimum Breaking Load (MBL, equation 8.3) and by rewriting the equation for the area of a circle (8.4 - 8.6).

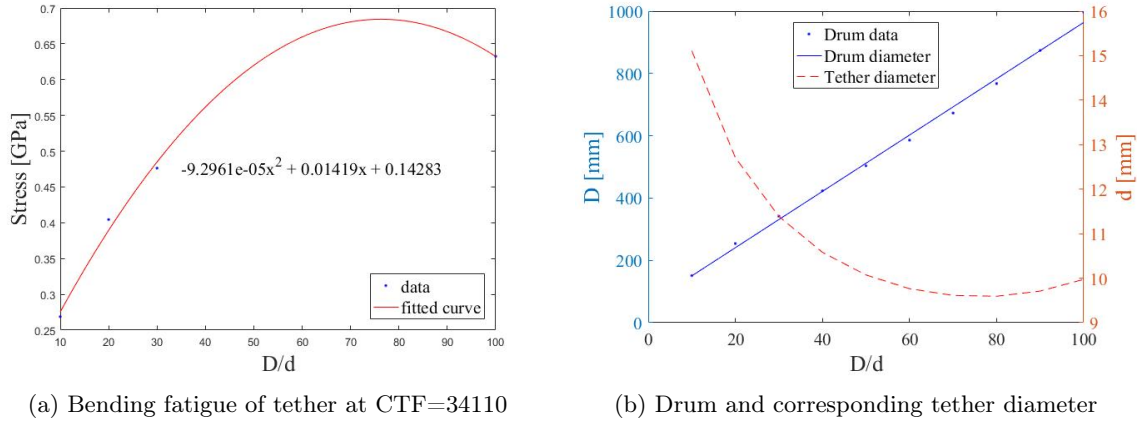


Figure 8.1: D/d ratio

$$\text{MBL} = \text{Design factor} \cdot \text{Reel-out force} \quad (8.3)$$

$$\text{Force} = \text{Area} \cdot \text{Stress} \quad (8.4)$$

$$\text{MBL} = \frac{\pi}{4} \cdot d^2 \cdot \text{Stress} \quad (8.5)$$

$$d = \sqrt{\frac{\text{MBL}}{\text{Stress}} \cdot \frac{4}{\pi}} \quad (8.6)$$

Now by rewriting the D/d ratio and filling in equation 8.6 the final graph can be composed (figure 8.1b). From this graph a desired ratio, and therefore tether and drum diameter, can be picked. Once these values are chosen it must be checked with creep lifetime performance (figure 33.16 from [22]) and tension failure but since bending fatigue is often the most limiting factor this is almost always satisfied. By using the relation in figure 8.2, which is constructed with use of [22], the worked-in tether diameter can be calculated. Since bending fatigue is dictated by the smallest sheave diameter the pulley diameter(s) must have at least the diameter of the drum.

It is chosen to fit the whole system in a 10 feet standard sea container. Because of this design three sheaves are needed. One pulley is needed to guide the tether systematically on the drum and another, pivoting, pulley is needed to guide the tether out of the sea container. To prevent possible twisting of the tether, since the upwind direction can change, a swivelling connection is introduced just before the start of the bridle. The load bearing part of this swivelling connection can be designed to fail when the tension force becomes too high by for example an unanticipated wind gust. Using such a failure mechanism contributes to the lifetime and risk mitigation of the tether and ground station systems. With use of the values stated in table 8.1 and the method described above the ground station parameters in table 8.2b are calculated.

There is no data available about the effective operational time of AWE system yet so the lifetime will probably be longer than 90 days since it is assumed, in the calculations, that the system is operational 24/7. Another possibility to extend the lifetime of the tether with almost a factor 2 is by inverting the tether such that the airborne part is now mainly at the drum and vice versa. However, since this method is not tested yet it is not taken into account in the model. Another improvement for the model would be to take the inertia of the drum into account. When this is realised one can find an upper (design) limit for the drum size and therefore an optimum for the D/d ratio.

Table 8.2: Ground station parameters

(a) Decided parameters		(b) Calculated parameters	
Description	Value	Description	Value
Number of sheaves	3 [-]	Tether diameter (nominal)	9.59 [mm]
Desired lifetime	90 [days]	Tether diameter (worked-in)	8.15 [mm]
Winding layers	1 [-]	Drum diameter	768 [mm]
Fibre type	Dyneema SK78 XBO	Drum length	2.37 [m]
Fibre density	970 [kg/m ³]	Pulley diameter(s)	768 [mm]

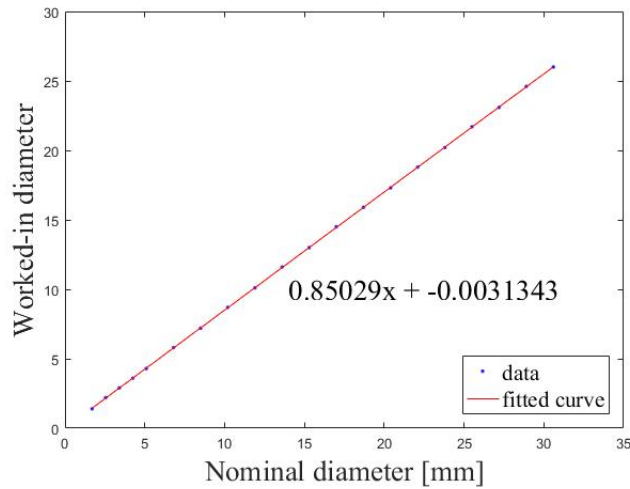


Figure 8.2: Relation between the nominal and worked-in diameter of the tether

8.2 Kite

The kite consists of five main structural components; the wingbox, the tail beam, the empennage, the winglets and the tail beam attachment as shown in figure 8.3. According to the theory presented in section 8.2.1, a stress analysis is performed on the wingbox, the tail beam and the empennage as described in sections 8.2.2, 8.2.3 and 8.2.4 respectively. The winglets and the tail beam attachment are designed qualitatively in section 8.2.5. It should be noted that all of these components are designed for an apparent kite velocity of 35 m/s with a safety factor for wind gusts, because the kite of the 2014 DSE group has been used as a base. This apparent kite velocity is a limiting factor on the output power. More information on this can be found in the recommendations.

8.2.1 Stress analysis theory

This section shows which equations are used in the stress analysis as described in the next three sections. All of the equations used in the remainder of the chapter are taken from Megson [14], unless stated otherwise. The **neutral axis** is calculated using equation 8.7 [18], in which the subscripts can be interchanged.

$$\bar{z} = \frac{\int_A \tilde{z} dA}{\int_A dA} \quad (8.7)$$

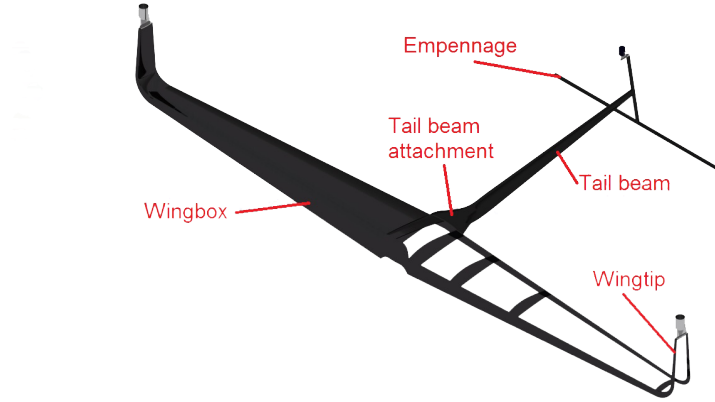


Figure 8.3: Internal structure of the kite

The **area moment of inertia** is given by equation 8.8 [18], in which the subscripts can be interchanged.

$$I_{xx} = \iint y^2 \, dx \, dy \quad (8.8)$$

The **normal stress due to an axial load** is calculated using equation 8.9 [7].

$$\sigma = \frac{F}{A} \quad (8.9)$$

The **normal stress due to bending** is calculated using the flexure formula, given by equation 8.10, in which the subscripts can be interchanged.

$$\sigma_z = \frac{M_y I_{xx} - M_x I_{xy}}{I_{xx} I_{yy} - I_{xy}^2} x + \frac{M_x I_{yy} - M_y I_{xy}}{I_{xx} I_{yy} - I_{xy}^2} y \quad (8.10)$$

The **shear stress** is calculated by using the shear of closed section beams theory from Megson. A cut is made to set the basic shear flow at this point to zero. The actual shear flow at the cut is then calculated by equating the moments of all shear flows to the moments of the internal forces around an arbitrary point. This shear flow is added to the basic shear flow to obtain the total shear flow as shown in equation 8.11.

$$q_s = q_b + q_{s,0} \quad (8.11)$$

The basic shear flow is given by equation 8.12.

$$q_b = -\frac{S_x I_{xx} - S_y I_{xy}}{I_{xx} I_{yy} - I_{xy}^2} \int_0^s t_x \, ds - \frac{S_y I_{yy} - S_x I_{xy}}{I_{xx} I_{yy} - I_{xy}^2} \int_0^s t_y \, ds \quad (8.12)$$

The moment equilibrium of the internal forces and the shear flows is given by equation 8.13.

$$S_x \eta_0 - S_z \xi_0 = \oint p q_b \, ds + 2A q_{s,0} \quad (8.13)$$

The shear stress is then calculated by dividing the total shear flow by the local skin thickness, as shown by equation 8.14.

$$\tau = \frac{q_s}{t_s} \quad (8.14)$$

The **von Mises stress** is then calculated to estimate if the structure will fail under the given loading conditions. It is given by equation 8.15, which uses the previously calculated normal stress and shear stress.

$$\sigma_v = \sqrt{\frac{1}{2} \left[(\sigma_x - \sigma_y)^2 + (\sigma_y - \sigma_z)^2 + (\sigma_z - \sigma_x)^2 + 6(\tau_{xy}^2 + \tau_{yz}^2 + \tau_{zx}^2) \right]} \quad (8.15)$$

8.2.2 Wingbox

The wingbox of the original kite has been designed for the load case during nominal operation. During reel-out, the kite generates enough lift to put a tension of 20 kN on the tether. [19] This tension is multiplied by a safety factor of 1.44 squared to account for wind gusts.¹ The wingbox configuration has been optimised for this load case. However, the wingtip rotors introduce a different loading into the wingbox during vertical take-off. These rotors deliver a maximum thrust of only 637 N in total, but since this loading is so different from the wing loading during nominal flight, a stress analysis is performed for the wingbox under vertical take-off conditions.

Wingbox configuration

The main wing has a wingspan of $b = 10$ m, a root chord of $c_r = 1.813$ m and tip chord $c_t = 0.726$ m. It consists of sandwich panels and carbon skin as shown in figure 8.4. The sandwich panels are made of a 10 mm thick foam, with a $t_s = 0.5$ mm thick layer of high strength carbon fibres named T700S on both sides, which can carry 375 MPa. [19] The front and aft spars are located at $0.1c$ and $0.6c$ respectively. The width of the simplified rectangular wingbox decreases linearly from $w_r = 0.91$ m at the root to $w_t = 0.36$ m at the tip. Its height decreases linearly from $h_r = 0.19$ m at the root to $h_t = 0.075$ m at the tip.

Wingbox assumptions

These five simplifying assumptions are made on the configuration of the wingbox to get rid of the asymmetries and curvatures, and on the load case:

- The wingbox is assumed to have a rectangular cross-section. As the Steiner terms of the panels are almost unaffected by this assumption, the area moment of inertia is underestimated by a maximum of 10% based on experience.
- The sweep of the centre of the wingbox is assumed to be 0 deg. This increases the rotor offset by 0.11 m. As a result, the maximum shear stress is overestimated by roughly 30%.
- The dihedral of the wing is assumed to be 0 deg instead of 2 deg. The effects of this assumption on the results are negligible.

¹Retrieved from: <http://www.radome.net/rsa.html> [Accessed on 26-06-2017]

- The leading and trailing edge skins, and the foam in the sandwich panels are assumed to be non-load-carrying components. This leads to an over-estimation of the stresses in the wingbox.
- Aerodynamic forces are neglected. During vertical climb, the vertical velocity would cause wing bending relief, which means that the stresses in the wingbox are again over-estimated.
- The mass of the wing is assumed to be distributed linearly in spanwise direction. A more detailed analysis on the mass can be performed after the final design to judge the effects of this assumption.

Wingbox load case

The load case considered for the wingbox occurs during vertical take-off. Figure 8.5 shows the forces on the right wing. The force at the wingtip is given by equation 8.16, in which $T_{\text{rotor}} = 437 \text{ N}$, $g = 9.81 \text{ m/s}^2$, $m_{\text{rotor}} = 0.04 \text{ kg}$, $m_{\text{motor}} = 3.2 \text{ kg}$, $m_{\text{hub}} = 0.13 \text{ kg}$ and $m_{\text{winglet}} = 1.1 \text{ kg}$. The distributed load is given by equation 8.17. This equation was obtained by assuming that p varies with the same ratio as the chord, and that integrating over the wingspan should yield the total wing mass $m_w = 22.6 \text{ kg}$. [19] This gives $p_r = 31.7 \text{ N/m}$ and $p_t = 12.7 \text{ N/m}$. From the free body diagram, shown in figure 8.11, the internal shear force and internal moment at any y -position can be derived to equations 8.18 and 8.19 respectively. The distributed load p is divided into a constant distributed load and a variable distributed load such that the equations can be found analytically.

$$F = T_{\text{rotor}} - g(m_{\text{rotor}} + m_{\text{motor}} + m_{\text{hub}} + m_{\text{winglet}}) \quad (8.16)$$

$$p = p_r - \frac{p_r - p_t}{b/2} y \quad (8.17)$$

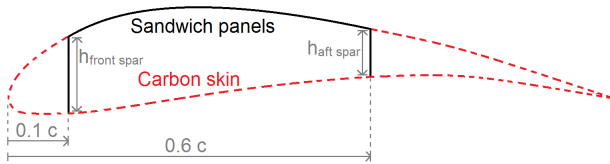


Figure 8.4: Configuration of a longitudinal cross-section of the wingbox

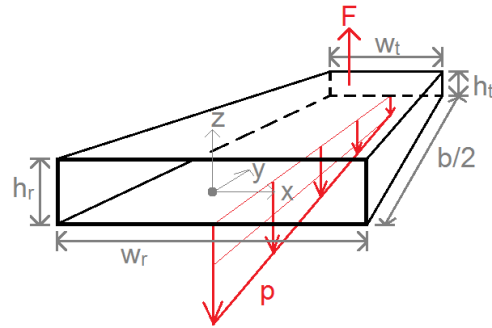


Figure 8.5: Load case of the wingbox during vertical take-off

$$S_z = F - p_t \left(\frac{b}{2} - y \right) - p \frac{1}{2} \left(\frac{b}{2} - y \right) \quad (8.18)$$

$$M_{xx} = F(b/2 - y) - p_t \frac{1}{2} (b/2 - y)^2 - p \frac{1}{6} (b/2 - y)^2 \quad (8.19)$$

Wingbox stress analysis

With the previously described assumptions and load case, the stress analysis of the wingbox is performed. The **enclosed area** and the **cross-sectional area** of a cross-section of the wingbox in the xz plane are given by equations 8.20 and 8.21 respectively.

$$A_{\text{encl}} = wh \quad (8.20)$$

$$A_c = 3wt_s + 4ht_s \quad (8.21)$$

The z location of the horizontal **neutral axis** in the xz plane follows from equation 8.7. The neutral axis lies just above the centre of the wingbox, as shown by equation 8.22.

$$\bar{z} = \frac{\frac{h}{2}(wt_s)}{A_c} \quad (8.22)$$

The **area moment of inertia** follows from equation 8.8. For the top and bottom panels only the Steiner terms are included, which yields equation 8.23.

$$I_{xx} = \frac{t_s h^3}{3} + 4ht_s(-\bar{z})^2 + 2t_s w \left(\frac{h}{2} - \bar{z}\right)^2 + t_s w \left(-\frac{h}{2} - \bar{z}\right)^2 \quad (8.23)$$

The **normal stress** follows from equation 8.10. With the chosen sign convention and the given load case this equation reduces to equation 8.24.

$$\sigma_y = -\frac{M_x}{I_{xx}} z \quad (8.24)$$

The **shear stress** in the wingbox is calculated using the sign conventions and variables as defined in figure 8.7. The cut is made at point 1, from which the basic shear flow is calculated in clockwise direction.

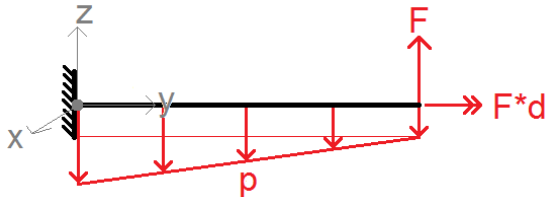


Figure 8.6: Free body diagram of the wingbox during vertical take-off

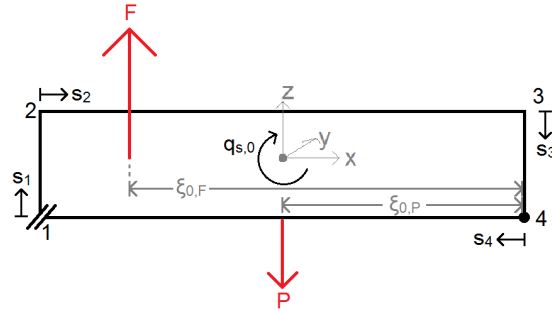


Figure 8.7: Definition of the shear flows in the wingbox

The basic shear flow follows from equation 8.12. Since $S_x = 0$ and $I_{xz} = 0$ due to the vertical line of symmetry, this equation simplifies to equation 8.25.

$$q_b = -\frac{S_z}{I_{xx}} \int_0^s tz \, ds \quad (8.25)$$

The basic shear flows in the front spar, top panel rear spar and bottom panel are then given by equations 8.26, 8.27, 8.28 and 8.29 respectively. In these equations the shear flows at points 2, 3, 4 and 1 in the wingbox can be obtained using $q_{b,2} = q_{b,12}(s_1 = h)$, $q_{b,3} = q_{b,23}(s_2 = w)$, $q_{b,4} = q_{b,34}(s_3 = h)$ and $q_{b,1} = q_{b,41}(s_4 = w)$.

$$q_{b,12} = -\frac{S_z}{I_{xx}} 2t_s \left[\frac{1}{2} s_1^2 + \left(-\frac{h}{2} - \bar{z} \right) s_1 \right] \quad \text{with } s_1 = z + \frac{h}{2} \quad (8.26)$$

$$q_{b,23} = q_{b,2} - \frac{S_z}{I_{xx}} 2t_s \left[\left(\frac{h}{2} - \bar{z} \right) s_2 \right] \quad \text{with } s_2 = x + \frac{w}{2} \quad (8.27)$$

$$q_{b,34} = q_{b,3} - \frac{S_z}{I_{xx}} 2t_s \left[-\frac{1}{2} s_3^2 + \left(\frac{h}{2} - \bar{z} \right) s_3 \right] \quad \text{with } s_3 = -z + \frac{h}{2} \quad (8.28)$$

$$q_{b,41} = q_{b,4} - \frac{S_z}{I_{xx}} t_s \left[\left(-\frac{h}{2} - \bar{z} \right) s_4 \right] \quad \text{with } s_4 = -x + \frac{h}{2} \quad (8.29)$$

Applying equation 8.13 around point 4 yields equation 8.30, in which $\xi_{0,F} = \frac{w}{2} + d$ and $\xi_{0,P} = \frac{w}{2}$. The rotor offset equals $d = 0.32$ m.

$$F\xi_{0,F} - P\xi_{0,P} = w \int_0^h q_{b,12} ds_1 + h \int_0^w q_{b,23} ds_2 + 2A_{\text{encl}} q_{s,0} \quad (8.30)$$

Expanding and rewriting this equation gives equation 8.31, which is used to calculate $q_{s,0}$.

$$q_{s,0} = \frac{F\xi_{0,F} - P\xi_{0,P} - w \left(-\frac{S_z}{I_{xx}} 2t_s \left[\frac{1}{6} h^3 + \frac{1}{2} \left(-\frac{h}{2} - \bar{z} \right) h^2 \right] \right) - h \left(q_{b,2} w - \frac{S_z}{I_{xx}} 2t_s \left[\frac{1}{2} \left(\frac{h}{2} - \bar{z} \right) w^2 \right] \right)}{2A_{\text{encl}}} \quad (8.31)$$

The **von Mises** stress follows from equation 8.15, which can be simplified to equation 8.32.

$$\sigma_v = \sqrt{\sigma_y^2 + 3\tau_{zx}^2} \quad (8.32)$$

Wingbox results

The aim of this stress analysis is to confirm that the wingbox does not fail under the described load case. Figure 8.8 shows the von Mises stress in the wingbox during vertical take-off. It shows that the maximum von Mises stress of 19.9 MPa stays well below the allowable 375 MPa, even with the conservative assumptions. This makes sense, because the loads on the wingbox during nominal flight, for which the wingbox has been optimised, are much higher than the loads during vertical take-off. Additionally the internal moment around the x-axis during vertical take-off does not exceed the internal moment around around the x-axis during nominal flight at any y-position in the wingbox. This means that skin buckling is not likely to occur.

8.2.3 Tail beam

The tail beam of the original kite has been designed for the load case during nominal operation. The new load case does not have to be analysed, because the force from the tail rotor during vertical take-off is much smaller than the forces from the empennage during nominal flight. However, since the mass of the tail beam significantly reduces the stability of the kite, a new, more elaborate stress analysis is required. This helps to further optimise the tail beam, such that the centre of mass of the kite shifts forward.

Tail beam configuration

The tail beam has the shape of an ellipse, of which the height equals twice the width. The semi-major axis equals half the height $a = h/2$, and the semi-minor axis equals half the width $b = w/2$. Figure 8.9 defines

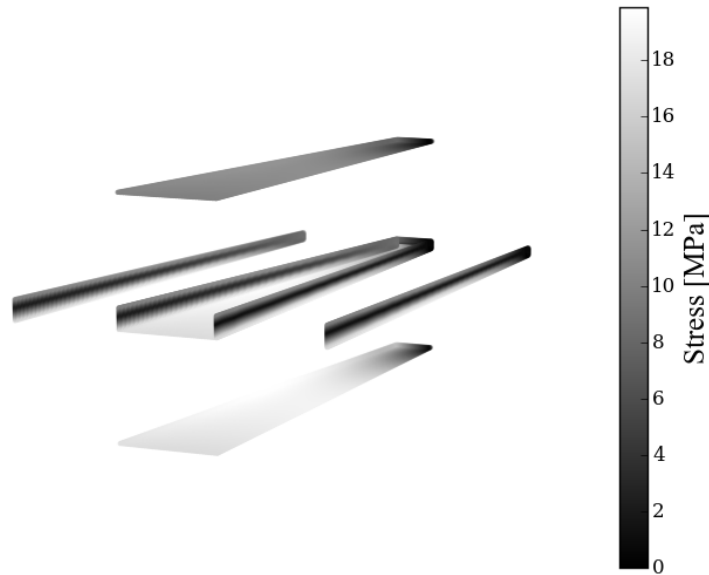


Figure 8.8: Von Mises stress in the wingbox during take-off (exploded view)

the basic parameters which describe the configuration of the tail beam. These parameters include the length $l_t = 4$ m, the height and width at the wing $h_w = 0.28$ m $w_w = 0.14$ m, and the height and width at the empennage $h_{emp} = 0.10$ m $w_{emp} = 0.05$ m of the tail beam. The skin has a thickness of $t_s = 1$ mm, and is made of a high strength carbon fibre named T700S, which can carry 375 MPa.

Tail beam assumptions

These three simplifying assumptions are made on the configuration and the load case of the tail beam:

- As it is analytically impossible to integrate over the periphery of an ellipse, the skin of the tail beam is modelled as a series of booms. The skins panels between those booms are then assumed to be straight, to have a thickness of zero and not to carry direct stresses. This means that the shear flow is assumed to be constant along such a skin panel. The effect of this assumption should go to zero as the number of booms goes to infinity.
- The moment caused by the drag of the horizontal tail is neglected. This leads to an under-estimation of the normal stress of less than 1% at $x=0$.
- The angle of sideslip is assumed to be equal to the angle of attack of the horizontal tail during reel-out, namely 6 deg. The flight dynamics of the kite should be studied to verify this assumption, but this left for further research.

Tail beam load case

The load case considered for the tail beam occurs during nominal flight while reeling out. Figure 8.10 shows the forces from the empennage on the tail beam. The lifting forces result from the angle of attack and the angle of sideslip when flying the figure-eights. Their magnitudes are given by equations 8.33 and 8.34 respectively. The total drag force is given by equation 8.35. In these equations, the lift and drag coefficients

of the NACA 0010 airfoil are $C_L = 0.66$ and $C_D = 0.01$.² The maximum apparent kite velocity comes from the power model $V_a = 35$ m/s which is multiplied by a safety factor for wind gusts $SF_{gust} = 1.44$. The surface areas of the horizontal and vertical tails are $S_h = 1.90$ m² and $S_v = 0.73$ m². Additionally, the air density at sea level is used $\rho = 1.225$ kg/m³.

$$L_h = C_L \frac{1}{2} \rho (V_a SF_{gust})^2 S_h \quad (8.33)$$

$$L_v = C_L \frac{1}{2} \rho (V_a SF_{gust})^2 S_v \quad (8.34)$$

$$D_{emp} = C_D \frac{1}{2} \rho (V_a SF_{gust})^2 (S_h + S_v) \quad (8.35)$$

From the free body diagram, shown in figure 8.11, the internal shear forces and internal moments can be derived to equations 8.36 and 8.37 respectively. The internal moments can be derived to equations 8.38 and 8.39 respectively.



Figure 8.9: Configuration of the tail beam

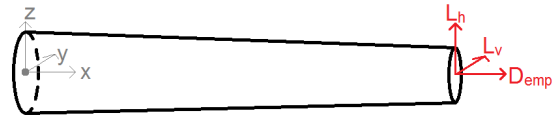


Figure 8.10: Load case of the tail beam during nominal flight

$$S_y = L_v \quad (8.36)$$

$$S_z = L_h \quad (8.37)$$

$$M_y = -L_v (l_t - x) \quad (8.38)$$

$$M_z = L_h (l_t - x) \quad (8.39)$$

Tail beam stress analysis

With the previously described assumptions and load case, the stress analysis of the tail beam is performed. The **enclosed area** and the **cross-sectional area** of a cross-section of the tail beam in the yz plane are given by equations 8.40 and 8.41 respectively.

$$A_{encl} = \pi ab \quad (8.40)$$

$$A_c = \pi \left[\left(a + \frac{t_s}{2} \right) \left(b + \frac{t_s}{2} \right) - \left(a - \frac{t_s}{2} \right) \left(b - \frac{t_s}{2} \right) \right] \quad (8.41)$$

The locations of the **neutral axes** in the yz plane follow from equation 8.7. Due to symmetry the neutral axes coincide with the y -axis and z -axis. The **area moments of inertia** follow from equation 8.8. They are calculated by subtracting the contribution of the outer enclosed area from the contribution of the inner enclosed area, which yields equations 8.42 and 8.43.

²Retrieved from: <http://airfoiltools.com/airfoil/details?airfoil=naca0010-il> [Accessed on 26-06-2017]

$$I_{yy} = \frac{\pi}{4} \left[\left(b + \frac{t_s}{2} \right) \left(a + \frac{t_s}{2} \right)^3 - \left(b - \frac{t_s}{2} \right) \left(a - \frac{t_s}{2} \right)^3 \right] \quad (8.42)$$

$$I_{zz} = \frac{\pi}{4} \left[\left(a + \frac{t_s}{2} \right) \left(b + \frac{t_s}{2} \right)^3 - \left(a - \frac{t_s}{2} \right) \left(b - \frac{t_s}{2} \right)^3 \right] \quad (8.43)$$

The **normal stress** follows from equations 8.9 and 8.10. With the chosen sign convention and the given load case this equation reduces to equation 8.44. In this equation A is the cross-sectional area.

$$\sigma_x = \left(\frac{M_z}{I_{zz}} \right) y + \left(\frac{M_y}{I_{yy}} \right) z + \frac{D_{emp}}{A_c} \quad (8.44)$$

The **shear stress** in the tail beam is determined using the sign conventions and variables as defined in figure 8.12. The cut is made in the skin panel left of the top boom. The basic shear flow is determined in clockwise direction.



Figure 8.11: Free body diagram of the tail beam during nominal flight

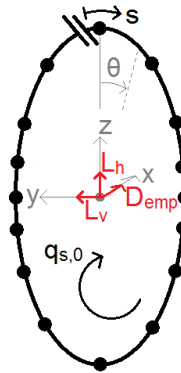


Figure 8.12: Definition of the shear flows in the tail beam

As mentioned before, the shear flow is determined by idealising the skin as booms. For this analysis, the booms are spawned at a constant angle spacing of ϑ , measured in clockwise direction from the positive z-axis. The Cartesian coordinates of the booms are then calculated by firstly calculating its distance to the origin using equation 8.45.³

$$R = \frac{ab}{\sqrt{(b \cos(\vartheta))^2 + (a \sin(\vartheta))^2}} \quad (8.45)$$

Next, the polar coordinates of the booms are transformed to Cartesian coordinates using equations 8.46 and 8.47.

$$y = -R \sin(\vartheta) \quad (8.46)$$

$$z = R \cos(\vartheta) \quad (8.47)$$

The areas of the booms are given by equation 8.48, which is obtained by equating the direct stresses and moments in the actual skin panels to those in the idealised skin panels. In this equation, b_r is the distance to the next boom.

³Retrieved from: https://en.wikipedia.org/wiki/Ellipse#Polar_form_relative_to_center [Accessed on 14-06-2017]

$$B_r = B_{r-1} + \frac{t_s b_{r-1}}{6} \left(2 + \frac{\sigma_{r-1}}{\sigma_r} \right) + \frac{t_s b_r}{6} \left(2 + \frac{\sigma_{r+1}}{\sigma_r} \right) \quad (8.48)$$

The basic shear flow in skin panel r then follows from equation 8.12. An extra term is added to account for the shear flow through the boom areas, which is shown by equation 8.49.

$$q_{b,r} = -\frac{S_y I_{yy} - S_z I_{yz}}{I_{yy} I_{zz} - I_{yz}^2} \left(\int_0^s t_{Dy} ds + \sum_{r=1}^n B_r y_r \right) - \frac{S_z I_{zz} - S_y I_{yz}}{I_{yy} I_{zz} - I_{yz}^2} \left(\int_0^s t_{Dz} ds + \sum_{r=1}^n B_r z_r \right) \quad (8.49)$$

Since $t_D = 0$ and $I_{yz} = 0$ due to the vertical line of symmetry, this equation simplifies to equation 8.50.

$$q_{b,r} = -\frac{S_y}{I_{zz}} \sum_{r=1}^n B_r y_r - \frac{S_z}{I_{zz}} \sum_{r=1}^n B_r z_r \quad (8.50)$$

Applying equation 8.13 around the origin of the chosen coordinate system yields equation 8.51. $q_{s,0}$ is determined by rewriting this equation.

$$0 = \sum_{r=1}^n b_r q_{b,r} p_r + 2A_{encl} q_{s,0} \quad (8.51)$$

In equation 8.51, b_r is length of the skin panel after boom r given by equation 8.52, and p_r is the moment arm of the skin panel after boom r to the origin given by equation 8.53.⁴

$$b_r = \sqrt{(y_{r+1} - y_r)^2 + (z_{r+1} - z_r)^2} \quad (8.52)$$

$$p_r = \frac{|(y_{r+1} - y_r)z_r - y_r(z_{r+1} - z_r)|}{\sqrt{(y_{r+1} - y_r)^2 + (z_{r+1} - z_r)^2}} \quad (8.53)$$

The **von Mises** stress follows from equation 8.15, which can be simplified to equation 8.54.

$$\sigma_v = \sqrt{\sigma_x^2 + 3\tau_{yz}^2} \quad (8.54)$$

Tail beam results

The aim of this stress analysis is to reduce the mass of the tail beam. Figure 8.13 shows the von Mises stress in the tail beam during nominal flight. With a skin thickness reduced from $t_s = 1.4$ mm of the original kite to $t_s = 1$ mm, the maximum von Mises stress of 261 MPa exceeds the 220 MPa which was the allowable stress in the original design. [19] The tail beam will therefore be made of the high strength carbon fibre T700S instead of regular carbon fibre.

8.2.4 Empennage

The internal structure of the empennage of the original kite has only been designed qualitatively. It was described that a circular beam of carbon fibre runs through the empennage. As the mass of the empennage is driving the static longitudinal stability of the kite, the structure of the empennage should be highly optimised. Therefore a stress analysis of the empennage is performed for static loading in nominal flight conditions.

⁴Retrieved from: <http://mathworld.wolfram.com/Point-LineDistance2-Dimensional.html> [Accessed on 14-06-2017]

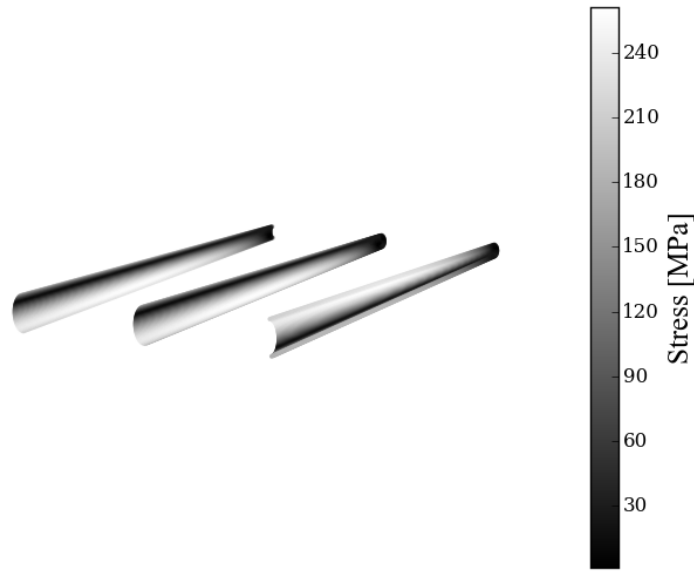


Figure 8.13: Von Mises stress in the tail beam during nominal flight (exploded view)

Empennage configuration

The empennage consists of a vertical tail with a span of $b_v = 1.19$ m and a horizontal tail with a span of $b_h = 3.07$ m, of which the parameters are defined by figure 8.14. They both have a NACA 0010 profile with a constant chord of $c = 0.62$ m, and a maximum thickness of $t = 0.062$ m. [19] The skin has a thickness of $t_s = 0.4$ mm, and is made from regular carbon fibre which can carry 220 MPa. A circular tube, made of the same material but with a thickness of 0.5 mm runs through the profiles at 25% of the chord.

Empennage assumptions

These four simplifying assumptions are made on the configuration and the load case of the empennage:

- The maximum stresses in the empennage are assumed to occur at the root of the horizontal tail. A Finite Element Method (FEM) analysis is required to investigate the stress concentrations in the vertical tail near the attachment to the tail beam, but this is left for further research.
- The drag force on the horizontal tail is neglected. This sets the internal moment around the z-axis to zero, instead of at 1.5% of the moment around the x-axis. However, since the area moment of inertia around the z-axis is larger than the area moment of inertia around the x-axis, the under-estimation of the von Mises stress can be neglected.
- The lift of the horizontal tail is assumed to be a point load at a quarter of the wingspan, and 25% of the chord. This results in an over-estimation of the normal stress, and an under-estimation of the shear stress of maximum 25%.
- The horizontal tail is assumed to have a configuration as shown in figure 8.15. This means that the circular shaft is neglected in this analysis, and that the moment of inertia is slightly under-estimated.

Empennage load case

The load case considered for the empennage occurs during nominal flight while reeling out. Figure 8.15 shows the force on the right section of the horizontal tail. This lifting force equals half of the lift of the horizontal tail L_h as defined in section 8.2.3. From the free body diagram, shown in figure 8.16, the internal shear force and internal moment at the root can easily be derived to equations 8.55 and 8.56 respectively.

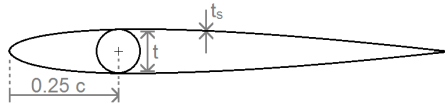


Figure 8.14: Configuration of the horizontal tail

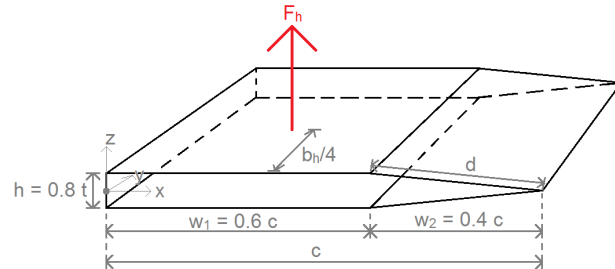


Figure 8.15: Load case of the horizontal tail during nominal flight

$$S_z = F_h \quad (8.55)$$

$$M_{xx} = F_h \frac{b}{4} \quad (8.56)$$

Empennage stress analysis

With the previously described assumptions and load case, the stress analysis of the empennage is performed. The **enclosed area** of a cross-section of the horizontal tail in the xz plane is given by equation 8.57.

$$A_{\text{encl}} = (hw_1 + \frac{h}{2}w_2) \quad (8.57)$$

The horizontal **neutral axis** in the xz plane follows from equation 8.7. Due to symmetry the neutral axis coincides with the x -axis. The **area moment of inertia** follows from equation 8.8. For the horizontal panels with length w_1 and the panels with horizontal length w_2 only the Steiner terms are included. Additionally, the panels with horizontal length w_2 are assumed to have a length of w_2 , which yields equation 8.58.

$$I_{xx} = \frac{t_s h^3}{12} + 2(w_1 t_s) \left(\frac{h}{2}\right)^2 + 2(w_2 t_s) \left(\frac{h}{4}\right)^2 \quad (8.58)$$

The **normal stress** follows from equation 8.10. With the chosen sign convention and the given load case this equation again reduces to equation 8.24. The **shear stress** in the horizontal tail is calculated using the sign conventions and variables as defined in figure 8.17. The cut is made at point 1, from which the basic shear flow is calculated in clockwise direction.

The basic shear flow follows from equation 8.12. Since $S_x = 0$ and $I_{xz} = 0$ due to the horizontal line of symmetry, this equation again simplifies to equation 8.25. The lengths of panels 45 and 51 are given by $d = \sqrt{(h/2)^2 + (w_2)^2}$. The basic shear flows in panels 12, 23, 34, 45 and 51 are then given by equations 8.59, 8.60, 8.61, 8.62 and 8.63 respectively. The shear flows at points 2, 3, 4, 5 and 1 in the wingbox can be obtained using $q_{b,2} = q_{b,12}(s_1 = w_1)$, $q_{b,3} = q_{b,23}(s_2 = h)$, $q_{b,4} = q_{b,34}(s_3 = w_1)$, $q_{b,5} = q_{b,45}(s_4 = d)$, $q_{b,1} = q_{b,51}(s_5 = d)$.

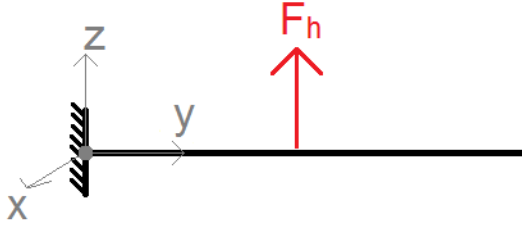


Figure 8.16: Free body diagram of the horizontal tail during nominal flight

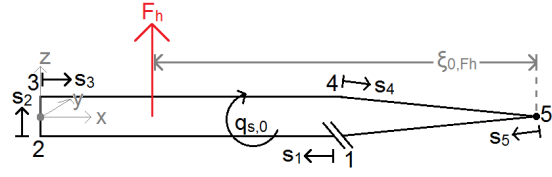


Figure 8.17: Definition of the shear flows in the horizontal tail

$$q_{b,12} = \frac{S_z}{I_{xx}} t_s \left[\frac{h}{2} s_1 \right] \quad \text{with } s_1 = w_1 - x \quad (8.59)$$

$$q_{b,23} = q_{b,2} - \frac{S_z}{I_{xx}} t_s \left[\frac{1}{2} s_2^2 - \frac{h}{2} s_2 \right] \quad \text{with } s_2 = z + \frac{h}{2} \quad (8.60)$$

$$q_{b,34} = q_{b,3} - \frac{S_z}{I_{xx}} t_s \left[\frac{h}{2} s_3 \right] \quad \text{with } s_3 = x \quad (8.61)$$

$$q_{b,45} = q_{b,4} - \frac{S_z}{I_{xx}} t_s \left[\frac{h}{2} s_4 - \frac{1}{2} \frac{h/2}{d} s_4^2 \right] \quad \text{with } s_4 = -\frac{d}{h/2} z + \sqrt{(h/2)^2 + (w_2)^2} \quad (8.62)$$

$$q_{b,51} = q_{b,5} + \frac{S_z}{I_{xx}} t_s \left[\frac{1}{2} \frac{h/2}{d} s_5^2 \right] \quad \text{with } s_5 = -\frac{d}{h/2} z \quad (8.63)$$

Applying equation 8.13 around point 5 yields equation 8.64, in which $\xi_{0,Fh} = 0.75c$.

$$F_h \xi_{0,Fh} = \frac{h}{2} \int_0^{w_1} q_{b,12} ds_1 + c \int_0^w q_{b,23} ds_2 + \frac{h}{2} \int_0^w q_{b,34} ds_3 + 2A_{encl} q_{s,0} \quad (8.64)$$

Expanding and rewriting this equation gives equation 8.65, which is used to calculate $q_{s,0}$.

$$q_{s,0} = \frac{F_h \xi_{0,F} - \frac{h}{2} \left(\frac{S_z}{I_{xx}} t_s \left[\frac{hw_1^2}{4} \right] \right) - c \left(q_{b,2} h + \frac{S_z}{I_{xx}} t_s \left[\frac{1}{12} h^3 \right] \right) - \frac{h}{2} \left(q_{b,3} w_1 - \frac{S_z}{I_{xx}} t_s \left[\frac{hw_1^2}{4} \right] \right)}{2A_{encl}} \quad (8.65)$$

The **von Mises** stress follows from equation 8.15, which can again be simplified to equation 8.32.

Empennage results

The aim of this stress analysis is to determine the required thicknesses of the skin and circular beam. Figure 8.18 shows the von Mises stress in the empennage during nominal flight, with a skin thickness of $t_s = 0.4$ mm. As the maximum von Mises stress of 100 MPa is well below the allowable 220 MPa including the safety factors from the assumptions, it is not necessary to add a circular beam for structural purposes. However, a circular beam with a thickness of $t_c = 0.5$ mm is included to serve as an attachment point for the skins, and to prevent trailing edge cracking.

8.2.5 Winglets and tail beam attachment

The final structural components left to analyse are the winglets and the tail beam attachment. For now, these components are designed without doing a stress analysis. For future research though, it is recommended to perform a FEM analysis on these components under their limit loads.

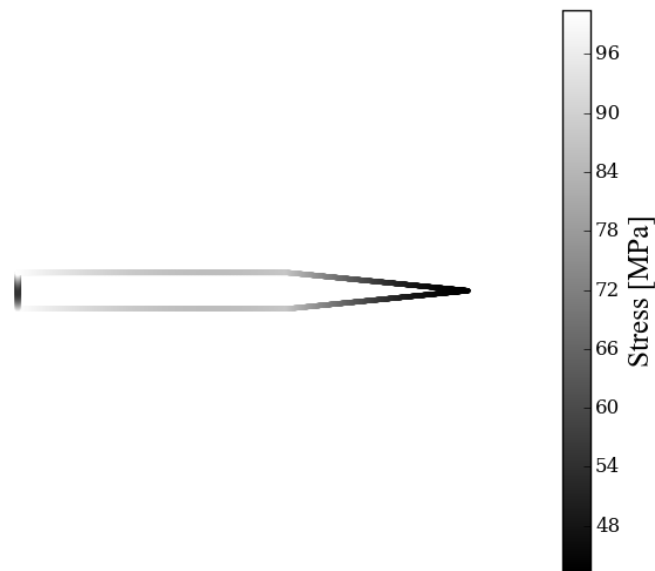


Figure 8.18: Von Mises stress in the empennage during nominal flight

The mass of the internal structure of the **winglets** is preferably kept low, as they highly affect the mass moment of inertia of the kite around its longitudinal and vertical axes. The structure is therefore kept simple, by extending the spars straight up to the wingtips. Additionally, an extra rib is added to close the wingbox, and to serve as an attachment point for the motor hub.

The purpose of the **tail beam attachment** is to transfer the loads from the tail beam gradually into the wingbox. To accomplish this, two extra ribs are added to the original design at a distance of 0.25 m from the root, which will transfer the sideforces from the empennage. Four embedded fasteners are used to attach the tail beam attachment to the wingbox, because of their capability to carry tensile loads. The tail beam is attached to the tail beam attachment by using the tail beam as a tapering collar. The tail beam is slid stuck over the tail beam attachment, and fixed using bolts to allow for easy detachment of the tail.

9 | Verification & validation

The verification and validation (V&V) procedure is an important guideline that needs to be defined to ensure that all the numerical models built and used during the project are coherent and credible. In this chapter, the V&V procedure is discussed in section 9.1. In the following sections, the V&V of the different numerical models: rotor model, power model, structural model, aerodynamic model and the stability and control model are analysed.

9.1 Guidelines & procedure

Based on a systems engineering approach, the verification procedure is defined to be carried out concurrently through each phase of the project and for each subsystem. The verification of any computational model built during the project should consist both of code verification and of calculation verification. In code verification, syntax errors and singular pieces of code should be checked and corrected. This is possible by conducting a unit test check on smaller pieces of code such as individual defined functions, condition statements or loops. For addressing calculation errors in the computational model, the results of the model should be verified against analytic solutions. The results from the unit test can be verified against hand calculation when possible. Furthermore, the complete integrated model should also be verified against possible analytic solutions. In this test, the effects of the assumptions made in the model should be identified and if possible, quantified. Finally, convergence of solutions should also be tested in the verification stage. This can either be done by testing multiple cases and verifying the expected trend of the multiple cases. On the other hand, the convergence of solution can also be tested by using a finer mesh for discretisation in the numerical model. If external computational programmes are used, the calculation verification of the model still needs to be performed. Again, the results should be verified against simpler analytic hand calculations. Furthermore, the convergence test should also be performed for the external programmes as well.

The model validation procedure should be used to justify the real world validity of the model. The computational models can be validated by either using comparison, analysis or experience. The hierarchy of reliability of these techniques for this project is identified as the following: comparison, experience and analysis. In the comparison validation method, results from external proven models or test data should be compared against results from the built computational model for the particular case. In the experience method, results from similar models in similar circumstances available in literature should be used to justify the results of the computational model. Finally, the analysis method includes validating elements of the computational model and also validating their integration. The analysis method largely depends on justifying that the model is correctly implemented (verified) and the assumptions made can be justified either qualitatively or quantitatively.

9.2 Rotor sizing model

The model and relevant equations to be verified are as shown in section 7.2. Since the models consists mostly of analytical equations that are programmed in MATLAB, manual calculations are compared to the generated data. Since arrays for R , Ω and $\vartheta_{75\%}$ are used, this comparison is done for several different indices within these lists to check if the calculations are correct for all options. Although combinations between the different array indices are possible, the same indices will be used for clarity. The starting values for R , Ω and $\vartheta_{75\%}$ are presented in table 9.1a.

No comparison is made for the solidity factor as this number is approximated by Newtons method, but will be used to check the equations. In order to check whether the approximation works, it is checked whether the amount of iterations will increase when the criterion for convergence decreases. Convergence is achieved when the difference between two iterations is smaller than a certain criterion. This analysis is presented in table 9.1b. The results of the comparisons are displayed in table 9.2 respectively.

Table 9.1: Values used for comparison that are labeled by their index, which were randomly chosen from the arrays from section 7.2

(a) Values used for comparison that are labeled by their index, which were randomly chosen from the arrays from section 7.2

Index	R[m]	Ω [rad/s]	$\vartheta_{75\%}$ [rad]
3	0.406	264.4174	0.0188
51	0.550	327.2492	0.0524
124	0.769	422.8060	0.1033
177	0.928	492.1828	0.1403

(b) Amount of iterations for s to converge using Newton's method

Index	crit = 10^{-3}	crit = 10^{-5}	crit = 10^{-7}
3	1000	10^5	10^7
51	1000	1687	1687
124	5	6	7
177	5	6	7

Table 9.2: Comparison between manual calculations and MATLAB output, where the number in the top row corresponds to the indices in table 9.1a and for a thrust of 100 N

Symbol	Manual 3	M3	Manual 51	M51	Manual 124	M124	Manual 177	M177
k[rad]	0.3007	0.3007	0.2559	0.2560	0.1881	0.1880	0.1387	0.1387
$C_T[-]$	0.0274	0.0274	0.0053	0.0053	0.0008	0.0008	2.9e-4	0.0003
s[-]	-	0.0000	-	NaN	-	0.0048	-	0.0011
c[m]	0.0	0.0000	-	NaN	0.0058	0.0058	0.0016	0.0016
$C_P[-]$	0.0052	0.0052	-	NaN	4.23e-5	0.0000	8.94e-6	0.0000
M[-]	0.8722	0.8696	-	NaN	0.5399	0.5468	0.5381	0.5300
Q[Nm]	3.8595	3.8612	-	NaN	2.0725	2.0275	1.4791	1.4891

From table 9.1b, it is noted that for options 124 and 177, convergence is achieved fast and with an increased amount of iterations. For index 3, it can be seen that no convergence is achieved since the maximum amount of iterations is defined as $1/\text{crit}$. This results in the solidity factor being 0. For index 51, it looks like convergence was obtained for $\text{crit} = 10^5$ and 10^7 . However, also referring to table 9.2, it can be seen that a NaN (Not a Number) is passed on. This is due to an present asymptote which gives no solution for s. Both of these options means no solution can be found, but feasible solutions will converge.

Looking at table 9.2, it can be seen that both the manual and MATLAB calculations are mostly within <1% difference. Some rounding errors are present, which are carried on and results in slightly bigger errors. NaN options, which result from unfeasible options, will not give a M and are thus also discarded. When the maximum amount of iterations are encountered, s will be 0 and result in a high M. For these options however, the chord will be 0 and will also be filtered out by the aspect ratio requirement.

It is concluded that the model is verified and usable, although some limitations are still present. For example, the assumption of uniform inflow may have a big influence and needs further research. It is also recommendable that when actual production starts, several prototypes should be built and be tested against the numerical results to ensure proper results.

9.3 Power model

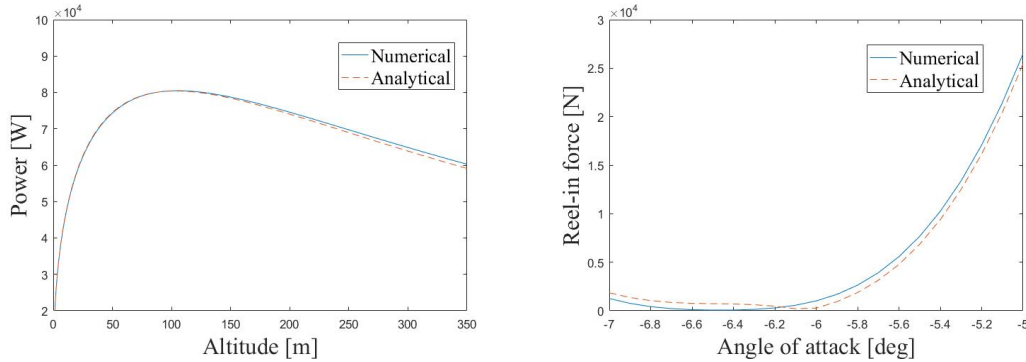
To verify and validate the power model, the code is split up in three units that correspond with subsections 3.7.3, 3.7.4 and 3.7.5. However, first the simple inputs such as density and wind shear model are verified. The lift and drag equations are also verified. These checks make sure that no unfeasible inputs are used for the model.

9.3.1 Verification

To verify the model for the output power, the numerical equation 3.10 is compared to an analytical equation 9.1 found in chapter 3 of the Airborne Wind Energy book. [22]

$$P_{\text{out,analytic}} = \frac{1}{1.11} \frac{2}{27} \rho S_{\text{proj}} \frac{C_L^3}{C_D^2} V_w^3 \cos^3(\vartheta) \quad (9.1)$$

The outcome of both equations for $V_{w,\text{ref}} = 7$ m/s at $h_{\text{ref}} = 10$ m and altitude h as input can be found in figure 9.1a. As can be seen, the numerical model slightly overestimates the power. The difference occurs due to differences in assumptions.



(a) The output power plotted for different heights using an analytical equation and a numerical equation for $V_{w,\text{ref}} = 7$ m/s
 (b) The reel-in force plotted for different angle of attacks using an analytical equation and a numerical equation for $V_{w,\text{ref}} = 7$ m/s and $V_{r,\text{in}} = 15$ m/s

Figure 9.1: Plots used for verification of the output power and the reel-in force.

Another verification is performed by constantly doing a hand calculation for a certain altitude and compare it with the value found with MATLAB. Only then the equations are used for every altitude.

For the reel-in phase, two different derived equations, a numerical and an analytical one, are used to calculate the reel-in force. The numerical equation is 3.13 and the analytical equation is 9.2 which are derived in the DSE 2014 report. [19]

$$F_{r,\text{analytical}} = \sqrt{(L - W_{\text{kite}} \cos(\varphi))^2 + (D - W_{\text{kite}} \sin(\varphi))^2} \quad (9.2)$$

$$\varphi = \arctan\left(\frac{V_{r,\text{in}} \sin(\vartheta)}{V_{r,\text{in}} \cos(\vartheta) + V_w}\right) \quad (9.3)$$

As can be seen in figure 9.1b the reel-in force is plotted against different angle of attacks with a reference velocity $V_{w,\text{ref}} = 7$ m/s and the reel-in velocity set at $V_{r,\text{in}} = 15$ m/s. Both curves follow the same trend and have more or less the same values. The small difference that occurs is due to the different assumptions used for the derivation of the equation. The reel-in force is afterwards only multiplied by the reel-in velocity which is a constant and therefore the input power is considered to be verified.

The final part that needs to be verified is whether the model applies equation 3.15 correctly. This was done by checking the components, found in equations 3.16-3.20 individually. For example, E_{out} was verified using equation 3.16 and by simply taking the average of P_{out} and multiplying by t_{out} , the outcome of both methods showed similar results. Also the time step $\Delta t_{\text{out},i}$ was checked by performing hand calculations as well as t_{in} and afterwards E_{in} . No significant errors occur and thus, the model is considered verified.

9.3.2 Validation

The validation of this power model is rather hard to perform. This is because there is no specific experimental data for rigid kites. There are; however, multiple start-ups like Kitepower working with a similar concept. Experts that work in these start-ups have performed a few tests and have developed, over time, a feeling for the values of different parameters. The opinions of these people is considered as a sanity check for validating the power model. The different phenomena that could be seen on the graphs were discussed and reasoned to make sense. The values found were also considered to be in the right magnitude. Therefore this model is considered to be validated as much as is possible as of yet. Further validation is required when experimental data is available.

9.4 Structural model

To verify and validate the models used for the stress analyses as described in chapter 8 section 8.2, the model for the tail beam is taken as an example. The reason why this model is taken as an example specifically, is because this model includes a discretisation which the other models do not have. However, the verification and validation methods described in this section can be, and are applied to the stress models for the wingbox and empennage as well.

9.4.1 Verification

The verification methods used to verify the basic properties of the tail beam and the external loads is done by re-doing the calculations by hand, and doing sanity checks. Such a sanity check is for example checking if the area moments of inertia have sensible magnitudes. Next, the internal load calculations are verified by plotting the internal shear force and moments, such that the signs and magnitudes can be checked. The last steps are to see if the normal and shear stresses have been computed correctly. The normal stress calculation is verified by checking the signs, and checking if the magnitudes vary linearly with distance from the neutral axis. Figure 9.2 shows that this is indeed the case. The shear stress is verified by checking if the basic shear flow goes back to zero at the cut ($q_{b,1}$), and by checking if the magnitude of $q_{s,0}$ makes sense. The signs are then verified by plotting the results in figure 9.3.

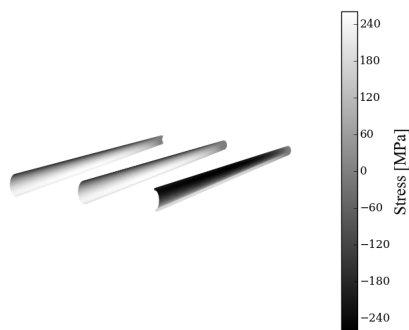


Figure 9.2: Normal stress in the tail beam during nominal flight (exploded view)

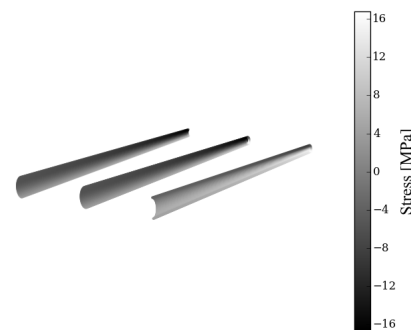


Figure 9.3: Shear stress in the tail beam during nominal flight (exploded view)

9.4.2 Validation

Similar to the power model, the structural model is difficult to validate without actual test data being available. Therefore, the fact that the theory described in section 8.2.1 is well-used in the industry is used

Table 9.3: Conversion of C_L and C_D and 18deg angle of attack with increasing mesh size.

Number of panels in x and y direction	C_L	Residual	C_D	Residual
4	2.068	-	0.199	-
8	2.120	0.052	0.182	0.017
16	2.125	0.005	0.176	0.006

as a model validation method for now. Alternatively, a FEM analysis could be performed as a validation method, but this is left for further research.

9.5 Aerodynamic model

The verification and validation of the aerodynamic models proved to be difficult. A limited amount of data is available and finding relevant sources is difficult. Section 9.5.1 explains the verification of the created aerodynamic model and section 9.5.2 verifies the assumptions made during the analysis of the wing download. These are the two significant areas of the aerodynamic model identified to be verified.

9.5.1 XFLR5 model

Multiple verification steps were taken to ensure valid output of the XFLR5 models. Before analysing full model, all individual airfoils were analysed. The output values of the airfoil XFLR5 analysis was checked with windtunnel data in reference sources¹. The output values reflected small errors between reference data and the XFLR5 data. The first verification of the XFLR5 kite model was done by recreating the model of the 2014 group and checking the results. As this test provided the same values as the 2014 report, the created model was deemed verified. The second verification method used was done by studying convergence by increasing the mesh size. As the mesh size increases, the model outputs should converge. When this was the case the newly created model was deemed valid. This procedure is shown in table 9.3.

During all stages of creating new aerodynamic models sanity checks were performed. XFLR5 shows the flow, down wash and pressure distributions. These outputs were monitored closely and checked for irregularities. To further validate the outcomes of the created models, a CFD analysis could be performed. This was considered to complicated and outside of the scope of this project. Further validation requires wind tunnel testing.

9.5.2 Wing download

Due to the complex nature of the rotor-wing interaction, validation of the estimated download is very difficult. With regards to the time and resources available, simulation of the interaction is not achievable. Instead, experts have been asked for sanity check on the estimated value. Both Leo Veldhuis (chairholder of Flight Performance department at Delft University of Technology Aerospace Engineering faculty) and Rolf Luchsinger (CEO of Twingtec) have confirmed that the method used to estimate seemed reasonable, and that the estimation of 8 % sounds feasible.

Further investigation is required to get a better estimation of the wing download. To begin with, it is suggested that more basic literature is used to expand the basis of the method of sizing. [23] is suggested as it may provide a clear and complete overview of the theory involved. Simulation of the phenomena is difficult as well due to the complex nature of the physics involved. It is likely that unsteady CFD simulation will be required that required significant resources. Instead, it is recommended to build a test setup similar to the one used by [6], to test for the wing download with all characteristics matching that of the design. After this, a prototype can be built to validate the results found.

¹Retrieved from: http://m-selig.ae.illinois.edu/ads/coord_atabase.html [Accessed on 27-06-2017]

9.6 Stability & control

In this section, the verification and validation of the numerical climb and descent numerical model is discussed. Similar technique is used for the longitudinal equilibrium model and thus, is not extensively discussed.

9.6.1 Numerical climb and descent model verification

The verification of of the numerical climb and descent model included both code and calculation verification. For code verification, the output of each function or loop was analysed independently in a unit test. For example, the wind shear model function was verified by plotting the results and verifying the output against [19]. For the major numerical loop, each sub-loop was analysed as it was added to the model. Therefore, integration of smaller pieces of code was also verified. The calculation verification was either carried out by checking expected trends in plots or comparing against hand calculations. For example, in the climb phase where force equilibrium is considered, the velocity should be held at a constant. Through this technique, it is verified that force equilibrium is indeed held. Alternatively, hand calculations were made at particular regions of the code where plot visualisation technique was no longer valid. Overall, the numerical model was extensively verified for the implemented equations derived in 6.1. Finally, the stability of the numerical model (forward Euler time stepping) was also tested by implementing different time steps $dt = 0.1 - 0.001$ s. Indeed, the model reflected good convergence as the residual decreased with smaller time step. The result of this analysis is reflected in table 9.4.

Table 9.4: Convergence of energy required for climb at $V_w = 25$ m/s for smaller time steps

dt [s]	Energy [MJ]	Residual [kJ]
0.1	1.5703	–
0.01	1.5724	2.1
0.001	1.5727	0.3
0.0001	1.5727	0.0

9.6.2 Numerical climb & descent model validation

For the model validation, the applicability of the assumptions made in section 6.1 is analysed. The point mass model assumed is a significant assumption that leads to an underestimation of the thrust required during the climb phase. For example, the climb model estimated the energy for $V_w = 25$ m/s at only 1.58 MJ. However, when the longitudinal equilibrium equation is introduced in the climb model, the energy required during climb increases to 1.80 MJ. In contrast, the trajectory of the climb model does not change as the velocity components v_x and v_z are more or less similar in the two simulations. Another source of error in the climb and descend numerical model is the aerodynamic model of the rigid kite. In the climb phase, the rigid kite is simulated to have a large phase of climb in the post stall region. Moreover, the aerodynamics of the rigid kite becomes quite significant at high wind speeds. Therefore, errors in the aerodynamic model directly translate into significant errors in the climb and descent model. A method of analysing the error induced in the simulation of the climb model due to error in aerodynamics is through a sensitivity analysis. For instance, an increase in 10% drag coefficient at each α increased the energy required during to 1.59 MJ. This translates to a relative error of only 1.0% in the energy required for climb at $V_w = 25$ m/s. In contrast, an increase in 10% lift coefficient at each α translates to a relative error of 3.6% in the energy required for climb. Another source of error in the climb model is the estimation of changes in control input as jumps. In reality, the change in thrust and pitch will be gradual over a time duration. This phenomena is likely to cause an increase in climb time and energy required. Similarly, the kinetics of the kite will also be affected due to dynamic movement during climb and landing. Furthermore, the model assumes that the thrust available exactly matches the thrust required for the climb. However, there is likely to be an error between required

thrust and the actual thrust. This error can be considered to have a low impact on the model as the response of brushless motors can be monitored actively and quickly through the autopilot system and the sensors. Finally, the asymmetric forces and moments are not considered in the model. The level of error that occurs in the model depends on the wind speed and orientation. The impact of asymmetric forces and moments will be larger in the landing simulation as the significance of the aerodynamic forces is more dominant.

10 | Sensitivity analysis

This chapter will present a sensitivity analysis of the final concept, a short analysis will be provided of the qualitative changes to the design when certain parameters are altered. First the effects on cost, maintenance, reliability and take-off and landing due to up-scaling will be investigated. Next the effects of changing wind speeds will be analysed, followed by changes in mass.

10.1 Scalability

In this section a rough estimation of the key parameters of the aircraft will be made if it were scaled up. The list of requirements gives a scalability requirement for a 2 MW system; therefore, all parameters calculated will be for a 2 MW rated power.

10.1.1 Scaled system parameters

First of all, the power model has been used to produce an expected projected area, wing span, annual energy production, maximum tether tension and eventually a tether diameter. This is then used to scale the chord and span of the horizontal and vertical tail. This led to an estimate of the total mass, including batteries. The lift and drag coefficient stayed the same since the the same airfoil is used for the larger wing. All these values are then used to calculate the thrust needed for the launching and landing manoeuvre and the required power and energy to produce the lift and overcome the rotor blade drag. These values result in a total amount of rotors and rotor blades, including their size. The next step is calculating the battery mass needed for energy supply, which takes up a large part of the total mass. This results in the values given in table 10.1. An important remark that has to be made is that these numbers give an extremely rough estimation of the values for a 2 MW system. They should be used to give an idea of the order of magnitude of the components of the system at this rated power and not as an accurate representation of such a 2 MW system.

Table 10.1: System parameters scaled 2 MW system

Parameter	Value	Parameter	Value
Rated power	2 [MW]	C_{L0}	0.572 [-]
Annual power production	1,900,000 [kWh]	C_{D0}	0.024 [-]
Wing span	40.7 [m]	Max. thrust main rotor	18.3 [kN]
Projected surface area	210 [m ²]	Max. power main motor	337.8 [kW]
Max. tether force	338 [N]	Energy for lift	386 [MJ]
Vertical tail wing span	4.8 [m]	No. of rotors	4
Horizontal tail wing span	12.5 [m]	No. of blades	4
Vertical tail wing chord	2.5 [m]	Rotors diameter	1.275 [m]
Horizontal tail wing chord	2.5 [m]	Battery mass	447 [kg]
Total mass (without motors)	1523.6 [kg]		

10.1.2 Discussion

In table 10.1, there is one aspect that is missing; these are the motor characteristics. The peak power that needs to be delivered by each of the four motors is 337.8 kW. Currently, there are no suitable motors on the market that can deliver such high output powers. There are industrial motors that can provide power up to more than 1 MW, but there masses drastically overshoot the mass acceptable for this system.¹

¹Retrieved from: <http://www.baldor.com/mvc/DownloadCenter/Files/BR600> [Accessed on 27-06-2017]

The best power-mass combination motor that was found is currently used in the system. This motor has a mass of 3.2 kg and can work constantly at a power of about 15 kW without overheating, for more information see section 7.4. This means that there are not much possibilities for scaling up the VTOL concept. An option would be to increase the amount of rotors, with each their own motor, to increase the lifting capabilities of the aircraft. The current configuration has rotors placed on the wingtips, which does not allow for a multiple rotor set-up as placing extensions comparable to wingtips is not an option. The only reasonable solution would be to integrate the extra rotors in the wing, which would require a completely different analysis. It would change the flow across the wings drastically due to the air that is sucked into the propeller and accelerated downwards. Therefore, this is an option for further research.

10.1.3 Alternative solutions

The limitation of the available motors means that to be able to scale the system to 2 MW, other options need to be considered. One promising option is to combine the vertical launch that is used now with the horizontal launch concept. This would mean that the first part of the launching manoeuvre will be performed by horizontally launching the kite and after a while the on-board propellers take over and provide the thrust to climb to operational altitude. For landing, the rotors are used again. This will save a lot of required power and energy, since launch currently demands the highest power and energy levels.

Another option is to decrease the weight of the aircraft to decrease required motor power by powering the launch using an electric wire. This electric wire would run along the tether towards the aircraft. The wires could then be connected to the motors to provide them with enough energy to perform the launch. When the aircraft reaches the desired position, it could then detach from the aircraft and move to the ground station. To avoid a hard landing of the wire and to make sure that it lands at the ground station, the wire could be guided down by small propellers or a parachute system while reeling in. This, however, might pose a problem while autonomously reconnecting the wire to the kite since this requires high accuracy and a compressive force.

10.2 Mass & centre of gravity

In traditional aircraft design, mass is often one of the most important parameters. While this is not so much the case for the VTOL AWE system considered, the influence of mass and centre of gravity is still present, as is discussed in the sections below.

10.2.1 Mass

During the design, it has been observed that a change in mass *can* introduce a further increase or decrease in mass, but not necessarily. For a VTOL aircraft, all mass needs to be lifted by thrust alone. This is different from the classical snowball effect for powered, regular aircraft. For this type of aircraft, an increase in mass the wing's lift must be increased, resulting in higher lift induced drag. This extra drag is to be countered with increased engine thrust, requiring more powerful, but also heavier engines. This adds again to the mass, starting this loop again.

For the VTOL glider, however, off-the-shelf electric motors were considered. This meant that an engine may have a small bit of excess power, as a slightly smaller variant could not be found. A small increase in mass does not necessarily require a different, heavier engine to be chosen because of this.

An increase in mass, however, does directly affect the energy required, and with that, the batteries' mass. A higher mass means hovering, the take-off manoeuvre, and the landing manoeuvre all cost more energy, requiring a larger battery, as has been shown in section 7.5. Mass also directly influences the rotor sizing, as these are optimised for a certain thrust, as described in section 7.2.

10.2.2 Centre of gravity

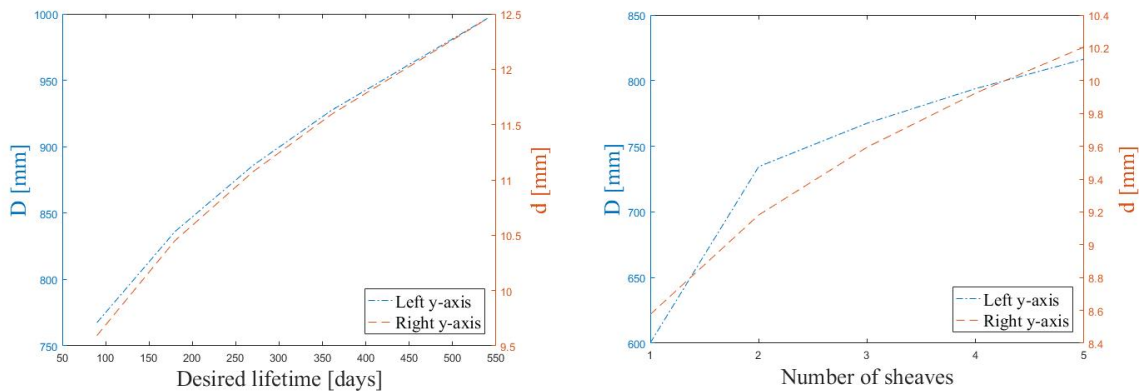
As discussed in section 3.6, the centre of gravity is to be within a narrow range of x-coordinates. As can be seen in table F.1, there are several components driving the centre of gravity location.

All components at the main wing, while making up most of the kite's mass, do not affect the centre of gravity location with respect to the neutral point by much, as the difference in x-coordinates is very small. This results in a small arm, and thus a small moment around the neutral point. The tail boom and all parts located further aft, however, all contribute significantly to the centre of gravity location, due to the large arm. The tail rotor sizing has proven to be crucial here, as it is the second heaviest component in the empennage, after the horizontal tail's surfaces, with a very long arm.

The only components that significantly move the centre of gravity forward are the batteries and the flight electronics, mounted in the nose of the body. These components are used to position the centre of gravity. An increase of mass in the empennage is managed by either enlarging the body, moving the batteries and electronics forward, or by increasing the battery size. Care is to be taken, however, that this method does not increase the overall mass too much. An increase of mass in the empennage requires significant lengthening of the body, or significant increase of the battery mass. Both solutions increase the total mass since a larger body means more material, which may introduce the need for larger main motors, as described in section 10.2.1.

10.3 Tether & drum diameter

To analyse the sensitivity of the tether and drum diameter the two variables that are decided for the final design (table 8.2a), the desired lifetime and number of sheaves, are chosen as variables to perform a sensitivity analysis. These variables can be analysed for the specific load case of the system described in this report by keeping all inputs the same except this variable. Figure 10.1 shows the results of the sensitivity analysis. These results can be used to deduce other choices within the final design. However, iteration with the power model should be taken into consideration because of drag changes concerning the projected area of the tether.



(a) Relation between the desired lifetime, drum diameter D and tether diameter d

(b) Relation between the number of sheaves, drum diameter D and tether diameter d

Figure 10.1: Sensitivity relations

11 | Financial projection

Money is a crucial factor for the system to succeed and become a meaningful product. Therefore, an estimation for the cost is made first in section 11.1, after which the return on investment is calculated in section 11.2. With the financial aspects of the designed system at hand, its position among competitors and within the future market is explored in section 11.3

11.1 Cost breakdown structure

With the entire system known, a first estimate for the cost can be made. A detailed cost breakdown is presented in appendix C, which is summarised in table 11.1. The production costs can be divided in three main categories, namely the development costs and the production costs for both the kite and the ground station. An important distinction is to be made, as the production costs for the kite and ground station are relevant per system, whereas the development costs for the design are a one-time expense. This means that the total development costs can be divided over the amount of systems sold; adding this to the production expenses results in an estimate for the total price per system. All costs, depicted in appendix C, are estimated based upon reference materials, products or services. Assuming that 150 AWE systems are sold, the price per system will approximately be €66,494.

Table 11.1: Summarised cost breakdown

Description	Value
Expected #systems sold	150
Total Development cost	€930,262
Production cost ground station	€21,070
Production cost kite	€38,103
Total cost per system	€65,374

It can be seen that a large fraction from the costs comes from the kite itself. As the launching and landing system is integrated within the previous design of the kite, a rise in production costs is to be expected. The kite costs are again divided in three categories. An estimation is made for the material and production costs separately, which together with the component costs make up for the total kite price. Referring to appendix C, carbon fibre, salaries for production and the price for the main motors seem to dominate the costs of their respective category.

For development costs, the salaries make up for a large fraction. These are estimated under the assumption that 6 full-timers will work on development, for 8 hours a day, 250 days a year, for 2.5 years. The prototype production costs are also significant, as they were estimated to be equal to 70% of the final ground station and kite production costs.

The ground station costs also have, similar to the other categories, salaries as a main contributor. The electronics and generator are also relatively expensive, but are also vital to the success of the mission.

11.2 Return on investment

In order to financially sustain the system, a positive Return on Investment (RoI) is required. Since the designed system will approximately cost €65,374 when 150 systems are expected to be sold, a certain price per kWh, which is called Levelised Cost of Energy (LCOE), is required to ensure profit is made. The lifetime of the system is required to be at least 20 years, which means that within this time span, enough money needs to be made. A Minimum Acceptable Rate of Return (MARR) was estimated, to obtain a minimum

return for which the system becomes interesting and competitive within the AWE market. An excel sheet was created to determine the the RoI. An overview of this calculation is given in table 11.2.

Table 11.2: RoI calculation summary

Description	Unit
Expected systems sold	150
System costs	€65,374
Annual energy production	248,000 kWh
Replacement costs	€4,161.32/y
General maintenance	€1,800.00/y
Insurance	€1,000.00/y
Tax rate	52%
Annual inflation	2%
Annual discount	8%
MARR	10%
RoI for 80 €/MWh	9 %
RoI for 95 €/MWh	12%

With use of a certain LCOE, the annual revenues can be determined. By subtracting the yearly replacement costs (as depicted in appendix D), insurance, and maintenance cost, the taxable income can be determined. Maintenance costs were based on a salary of €30 an hour, with 60 working hours in a year. From this taxable income, 8% of subsidies are deducted, after which the annual taxes are determined. Using this analysis, inflation can be used to calculate the Net Present Worth (NPW) over the lifetime of the system, which is then used to obtain the RoI. It can be seen that using 80 €/MWh is sufficient to make a profit, but not enough to meet the MARR requirement. By taking 95 €/MWh as LCOE, investing in the system becomes viable and profitable, whilst exceeding the MARR.

11.3 Market analysis

The objective of the market analysis is to establish the competitive cost and volume of the market for the AWE system. With this project there were two different markets that could be focused on: selling a launching and landing system for companies that produce kites or selling an off-the-shelf product to the companies in the energy market. It is chosen to produce an off-the-shelf product for the companies in the energy market such as Eneco and Nuon. The main stakeholders of the AWE system are Delft University of Technology, KitePower and Ampyx Power. Most of the requirements for the design come from these main stakeholders and they are important partners in getting the AWE system on the market. This section first goes into detail about the current market by looking at the LCOE as well as the Society's Cost of Energy (SCOE) of comparable products, so different energy sources. Then similar projects are analysed and the added value of the designed AWE system for the market is described. Finally, the future market is discussed by making a forecast and looking at the establishment of a new market.

11.3.1 Current market

In this subsection the current market opportunities will be analysed. This is done by looking at comparable products, similar projects and the added value of the AWE system.

Comparable products

There are different ways to produce electricity. Some ways use non-renewable energy sources such as coal, gas or petroleum. However, there are also ways to generate electricity with renewable sources such as solar power, wind energy and hydro power. Found was that about 65% of all energy produced in the United States is from fossil fuels, about 20% from nuclear energy and about 15% is from renewable sources. This data is obtained from the U.S. Energy Information Administration.¹ This means that there is still a big market share for fossil fuels, although this source will eventually run out. Next to that, the social pressure for energy companies to produce electricity using renewable sources increases because of the increased customer awareness of global warming. Therefore, there is a lot of growth possible in the renewable energy market. The International Energy Agency expects renewables by 2035 to generate more than 25 percent of the world's electricity consumption, with a quarter of this coming from wind. [1]

To see how much potential there is for this AWE system to grow and replace the non-renewable energy market share, the LCOE is considered. The lower the LCOE the more attractive the prices for the consumer can be, which can increase the growth rate of the wind energy market share. The LCOE calculation does not include the total actual economic costs of individual primary energy sources. This is why another calculation model is used, namely the SCOE. [1] It takes besides the standard things for LCOE also other things into account such as social impacts, environmental impacts and subsidies. According to the calculations performed by Siemens for the United Kingdom this results in the SCOE per energy source as in figure 11.1. As can be seen,



Figure 11.1: Estimated SCOE of different energy generation products for 2025 obtained from a paper of Siemens [1]

in the long term renewable sources will have a lower SCOE than the non-renewable energy sources, especially the wind energy source. This shows that besides a lot of room for growth for the wind energy market, the growth rate can also be high due to the low SCOE. For now the focus will be on onshore wind energy with an estimated SCOE in 2025 of 60 €/MWh, but once the technology is more developed the offshore wind energy is also very promising with an estimated SCOE in 2025 of 61 €/MWh.

¹Retrieved from: https://www.eia.gov/outlooks/aeo/electricity_generation.cfm [Accessed on 27-06-2017]

Similar projects

Now that the comparable energy products have been discussed, similar projects to the AWE system described in this report will be briefly mentioned and elaborated upon. Most of these projects are still in the conceptual phase and the people involved are working hard on producing the prototypes.

Kitepower - The system of Kitepower uses a flexible kite with a surface area of about 70 m² attached to a 400 m tether with a rated power production aim of 100 kW. The tether is attached to a drum on the ground station. This drum is connected to two generators that transform the reel-out of the tether into electricity. The operational altitude of the kite is above 100 m to make use of the more steady and stronger winds at that altitude. The aim is to reach a capacity factor of about 60%, while the conventional wind turbine only achieves about 35%.²

Ampyxpower - The AP3 system of Ampyxpower uses a rigid kite with a surface area of 12 m² attached to a tether with a maximum length of 900 m. The rated power production is 250 kW with a goal of scaling this eventually to a 2 MW system in the future. The tether is attached to a drum on the ground station which in turn is connected to one big generator. The operational altitude is in between 100 m and 465 m. The capacity factor for this system is unknown.³

Kitemill - The system of Kitemill uses a rigid kite with an unknown surface area and span and a tether with an unknown maximum length. The rated power production for 2017 is 30 kW with an upscale in 2018 to 100 kW and later even to 500 kW. The aim is to use the wind in between 500 m altitude and 1500 m altitude. For this system the tether is connected to a drum on the ground station which drives a generator to produce electricity. The capacity factor for this system is unknown.⁴

Twingtec - The system of Twingtec uses a rigid kite with 15 m span and a tether with a maximum length of 500 m. The rated power production for 2017 is 100 kW. The operational altitude of this system is under the 300 m. For this system the tether is connected to a drum on the ground station which drives a generator to produce electricity. The capacity factor for this system is unknown.⁵

Makani - The system of Makani uses a rigid kite with an unknown surface area and span and also the maximum tether length is not known. However, the operational altitude is known and is from 100 m altitude to 450 m, this would have to result in a rated power production of 600 kW. For this system a conductive tether is connected to the ground structure and transfers the electricity generated due to the rotating rotors on the kite. So the power is generated on the kite and not on the ground structure, as is done in the projects mentioned before. The capacity factor for this system is unknown.⁶

E-kite - The system of E-kite uses a rigid kite with an unknown surface area and span. Also the maximum tether length and operational altitude are unknown for this system. The rated power production right now is 100 kW with future upscaling to first 500 kW and eventually to 2 MW. For this system the tether is connected to a drum on the ground station which drives a generator to produce electricity. The capacity factor for this system is unknown.⁷

Added value

As mentioned in the beginning of this section, 15% of the energy produced in the United States comes from renewable sources. About 5.6% of the energy generated comes from using wind energy systems, mainly wind turbines. Also mentioned before is that there is an opportunity to increase the market share of renewable sources and in particular the source wind energy.

²Retrieved from: <http://www.kitepower.eu/> [Accessed on 27-06-2017]

³Retrieved from: <https://www.ampyxpower.com/nl/> [Accessed on 27-06-2017]

⁴Retrieved from: <http://www.kitemill.com/page/38/Home> [Accessed on 27-06-2017]

⁵Retrieved from: <http://www.twingtec.ch/> [Accessed on 27-06-2017]

⁶Retrieved from: <https://x.company/makani/> [Accessed on 27-06-2017]

⁷Retrieved from: <http://www.e-kite.com/> [Accessed on 27-06-2017]

The LCOE in 2013 for onshore wind energy is about 81 \$/MWh, see figure 11.1. In section 11.2 is calculated that with our current system the estimated LCOE is 95 €/MWh, note that the LCOE is here expressed in euros instead of dollars. This is slightly higher than the current LCOE but an upscaled version of this AWE system is considered to have a lower LCOE and be competitive to the wind turbines. Another way of getting the LCOE down is by creating wind energy farms, where multiple AWE systems will generate energy next to each other. The costs go down because multiple AWE systems can use the same facilities, for example the system that makes sure that the electricity produced is getting on the grid.

A weakness of the system however is that it can only operate in certain sparsely populated areas where large ground areas are available. This is mainly due to safety reasons and to give the public a safe feeling. Since the AWE systems are relatively new, not many regulations are made for it yet. Currently the system can be considered either an extension of a building or it can be classified as an aircraft. The choice is made by considering the altitude on which the kites operates and how rigid or flexible the kite is. If the choice is made to classify the kite as an aircraft a lot of extra regulations are applied to it and a complete redesign might be needed. Important is to have a safe system to make sure that it cannot only operate in uninhabited areas. Right now the public is in favour of renewable energy, but if there is uncertainty about the safety of the system, the public opinion might become negative towards AWE systems which will be fatal for the potential growth.

Under the assumption that the AWE system is safe and meets all the regulations. With a rated output power of 116 kW, a capacity factor of 38% and a RoI of 11% for a LCOE of 95 €/MWh, the system can be considered to compete in the current market and with the similar projects mentioned before. To be favourable over other wind energy systems the LCOE should be brought down towards 50 €/MWh. Note that the LCOE is now expressed in euros instead of dollars. If the design requirements are met and the LCOE is brought down enough, there is a future for this AWE system.

11.3.2 Future market

In this subsection the AWE system will be analysed with respect to the market in five to ten years, this specific market has yet to be established. This means a prediction of the future market must be made, which is already partly done to make figure 11.1.

Establish new market

From the data sheet 'Primary Energy Production by Source' from the U.S. Energy Information Administration ⁸ figure 11.2 is created. From this graph can be seen that the market share of fossil fuels is decreasing the past ten years while the renewable energy market share increases. This trend occurs since the resources for fossil fuels are shrinking and the public opinion leans more towards green energy. Assumed is that this trend will continue as it goes now. Furthermore, it was already concluded that the LCOE of renewable energy decreases, making it a more attractive way of producing energy. Therefore the production scale can probably grow.

The establishment of a new market for AWE system seems to be possible if the public keeps on supporting green energy. This will result in an increasing demand of green energy and more financial support for research to alternative ways of harvesting energy, such as the AWE systems. The forecast is that the AWE systems will go to 250–300 kW by improving the kite technologies, improving the trajectory and using even stronger winds at higher altitudes. A consequence is that the LCOE decreases which was also predicted in figure 11.1, making AWE systems more and more attractive.

Forecast

The forecast for the market in ten years is that a lot more research is done and a lot more data is available to improve designs. Different companies will be competing to have the most efficient and elegant system. This natural competition drives companies to keep innovating and improving their designs. This will eventually

⁸Retrieved from: https://www.eia.gov/totalenergy/data/monthly/pdf/sec1_5.pdf [Accessed on 27-06-2017]

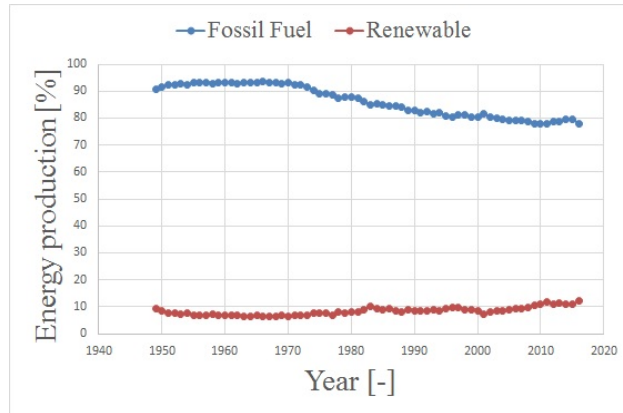


Figure 11.2: The percentage produced by fossil fuels and renewable sources of the total energy production.

lead to systems that can operate off-shore. Once this point is reached a turning point is expected in the wind energy sector, since the power density off-shore is much higher than on-shore. Also when the AWE systems are ready to go off-shore the noise and sight problems do not matter anymore.

Another thing that will naturally change with the years is the production scale. Expected is that in ten years the AWE systems can go into mass production, reducing the production costs significantly. A weakness may however be that in ten years it is decided to classify AWE systems as aircraft, giving it much more restrictions in design. Overall the forecast for the market is that there is a lot of potential for AWE systems.

12 | Sustainable development strategy

Wind energy is worldwide contributing to decrease the fossil fuel consumption and lower carbon dioxide emissions. The research in this report will further contribute to this trend of green energy production.

As sustainable energy production is the goal of the project the production evaluated for influence according to 'design for sustainability' (D4S) method taught at Delft University of Technology by Dr. M. Crul and Dr. ir. Diehl.¹ This is done by assessing the sustainability of the final product based on its impact on the environment, its influence on local society and the profitability for the industry.

Up until the midterm report the sustainability officer monitored if the selected concepts were in line with the stated sustainability objectives. This was a recurring process which steered the brainstorm sessions towards sustainable solutions and later on influenced the trade-off between the different concepts. This process has ensured that for the final trade-off only sustainable concepts were considered. An example of this process is that the LTA concepts performed adequately in the trade-off, but did not meet the guidelines for sustainability. The reason for this is that the helium needed for the LTA concept is a scarce resource and use should be avoided for a sustainable design. After selection of the final VTOL concept a more in dept view on the sustainability could be developed. Section 12.1 describes the approach to select sustainable materials. Section 12.2 describes how the system integrates into its surrounding in a sustainable manner. Lastly, section 12.3 describes economical sustainability in the future.

12.1 Sustainable use of materials

The environmental impact of the kite is mainly determined by its production and the used materials. The objective during the design of the subsystems was to minimise the used materials. This not only improved the sustainability of the design but was also of high importance for the feasibility, as a higher mass makes it difficult to launch the kite. To increase the sustainability of the kite, the aim is to create a circular product. All materials need to be recycled into new products.

Research into carbon fibre composites showed that production requires high temperatures and therefore is not energy efficient. On top of that carbon fibre is hard to recycle and often ends up in landfills. As the market is just realising this problem solutions are in the early stage of development and will become better in the near future. As carbon fibre composites are in general difficult to recycle, different materials like metals were considered. However, the sustainable benefits do not weigh up to the weight increase by not using carbon fibre composites. As carbon fibres were considered the only option due to their high strength-to-weight ratio, recycling of the material after use was investigated. Currently methods exist for recycling carbon fibres: pyrolysis, burning away the resin and retrieving the fibres. After this process the fibres have the same properties as original fibre. The downside of this method that high temperatures are required and a lot of energy is needed. A second way of recycling fibres is grinding. The fibres are ground into smaller fibres. Lower energy is required for this method but the final product loses part of its strength. A decision between the two recycling options will need to be made based on the market. As the recycling of the fibres is costly, a trade-off between revenue and sustainability will need to be made.

Secondly the used resin was checked for toxicity and impact on the environment. The 2014 design did not specify the used resin yet. Therefore a new selection was done, of which the considered options are shown in table 12.1. It was concluded to use the 1070 ECO + 1074 ECO as it provides enough strength and is more sustainable than the Epoxy resin + hardener.

The tether is the part most influenced by wear. To optimise its lifespan the tether will be turned around at half of its lifetime. The tether section closest to the kite experiences the most wear due to the repetitive bending. By turning the tether around the full tether can be used up to its limit. Another option could be to give the tether a variable thickness. The tether section that experiences the most wear should be given a larger thickness. At the end of the tether lifetime a second purpose could be given to the fibres. Dyneema

¹Retrieved from: <http://www.thesustainabilitysociety.org.nz/conference/2010/presentations/Crul-Diehl.pdf> [Accessed on 27-04-2017]

Table 12.1: Resin data table

	Epoxy Resin L + Hardener GL 1	1070 ECO + 1074 ECO	BD4015
Density [g/cm ³]	1.171	1.11	1.30
Module [GPa]	3.49	3.24	0.0186
Bio-degradable	No	No, but 37% bio-sourced	100% biodegradable

states that the thread could also be used to produce clothes and protective wear. Further research to the profitability and quality of the tether after use should be done to work out this option further.

Finally a solution for the recycling of the batteries was investigated. Lithium-ion batteries contain toxic chemicals and should be disposed of properly. The batteries can be recycled but retrieving the valuable materials does not pay-off. Recycling is mainly done to prevent the toxins from ending up in the environment.² Different batteries were considered to improve the sustainability, but all have the same problem of being difficult to recycle and being harmful to the environment if not disposed of correctly.

During production the amount of waste is minimised following the lean manufacturing philosophy. This method considers all non value adding processes as waste. This approach should be taken into account when creating the production plan.

12.2 Sustainable integration into the surroundings

Furthermore the system must be integrated into its surroundings in a sustainable manner. This airborne wind energy method is already improving the effects on the surrounding compared to conventional wind turbines. Because of the high altitudes flown and the limited ground structure that is needed (no tower required). The blockage of the view or disruption of the landscape is almost negligible. To further limit the visibility of the system the ground station will be painted in a colour that suits its surroundings. To limit the impact of the system on the surroundings the produced noise was limited to a minimum. Again this airborne system proves a big improvement compared to conventional wind turbines. The maximum noise production will occur during take-off and landing, but since this is only for a short amount of time no actions were taken to limit this noise. A constant noise will be produced by the fans cooling the motor during reel in. A housing around these fans could bring this noise further down. Finally the effects of the product on local wildlife must be limited. Analysis showed that the ground station does not negatively influence the wildlife but the kite might. Birds might be struck by the kite, which is not only damaging the wildlife but is also a high safety risk for the kite. In section 3.8 the possible use of lasers to guide birds around the trajectory of the kite was discussed as a solution for this problem.

12.3 Economical sustainable future

The designed system will bridge the gap between the energy market and airborne wind energy. Creating a fully autonomous system allows for safer and cheaper operation. In the future the aim will be to further lower the costs by scaling up the production and the size of the kite. As the price of the technology will go down the amount of systems in use will go up, increasing the share of green energy on the electricity market. For further optimisation and cost decrease of the technology, part of the profit from this sector will need to be put into research for improvements of the system. When offshore wind turbines have lost their value, the bases of their towers could be re-used. The autonomous launching and landing system enables AWE to be used offshore. This will increase the amount of available locations for this system and increase profitability, due to the more constant and higher wind speeds at sea.

²Retrieved from: http://batteryuniversity.com/learn/article/recycling_batteries [Accessed on 27-06-2017]

13 | Project design & development logic

This chapter will cover the future development of the proposed design. The activities necessary for further development of the 2017 design into a commercially viable product will be outlined. A production plan will be presented which will outline the usage of resources, both personnel and material.

13.1 Design & development

The post DSE work will be divided in the six phases pictured in figure 13.1: design, manufacturing, assembly, testing, operations and disposal. These phases are executed parallel to each other, for a more chronologically correct depiction of the activities see the Gantt chart in figure 13.2.

Because of the general nature of the planning, at this point it is impossible to go into detail of each individual activity so they have been grouped in these general tasks. The task durations in the Gantt chart are rough estimates. The design, manufacturing and assembly tasks can be divided in multiple smaller tasks that take place somewhat simultaneously so interrelations and dependencies between the tasks have been left out.

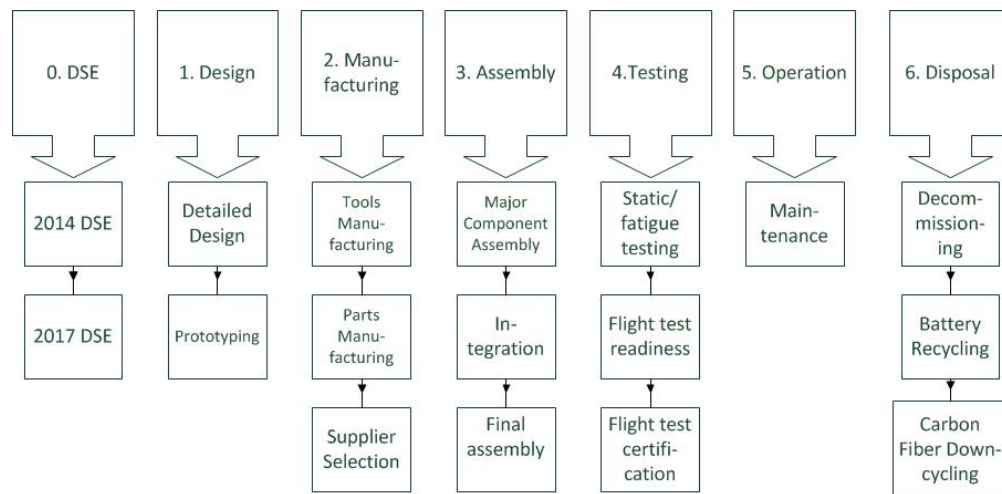


Figure 13.1: schematic view of future activities

The design phase will focus on finalising the design proposed in this report. The design presented is still preliminary, there are plenty of specifics of the design which need more analysis or that have simply not been performed because of time restrictions. A more detailed CFD and structural analysis will have to be done for the wing as well as the propeller that was chosen. The software that will control the autopilot was not covered in this report so this will also need to be designed in this phase. In this phase scaled-down prototypes of the basic design will be built which will be tested in a windtunnel.

The manufacturing phase will focus mainly on the manufacturing of the components but also on tooling manufacturing. This is the manufacturing of specialised tools and rigging that are required to manufacture and assemble the product. This phase will also cover selection of the suppliers who will deliver components that are too expensive or need specialised knowledge to produce; components such as the motors, the tether, the batteries, the generator in the ground station and most of the electronic circuitry.

During the assembly phase the components will be assembled into the final product. The assembly is split up in the major component assembly, integration and the final assembly. Major component assembly covers the assembly of the wing and the tail of the kite. This constitutes all the parts that need to be tested during the fatigue test. Integration is also part of the assembly, this is testing whether the different hardware and software sub-components or units work together as intended or not. It is recommended to do this in an early

stage to find any incompatible hard or software and reduce the possibility of any potential delays. During final assembly the construction of the complete, functioning aircraft, which started in the major component assembly, will be finalised.

During testing, the partially assembled main structures will undergo static and fatigue testing. Next is the flight test readiness which determines if all flight and ground hardware, software, personnel, and procedures are operationally ready for testing and data acquisition. During the certification process the manufacturer has to demonstrate to the authority that the aircraft meets all the safety requirements. Considering the kite is in essence a UAV and a power generator combined, the authority in question is both the aircraft authority and government authority in charge of sustainable energy. When the project is mature enough it will be presented to the respective authorities and rules that apply for certification will be set. Then means to demonstrate compliance have to be defined and agreed upon. Next, compliance has to be demonstrated. Finally if the authority is satisfied the certificate will be issued.

During the lifetime of the kite and ground station maintenance has to take place every 90 days or whenever a component fails. When the planned lifetime has passed, the kite and ground station need to be decommissioned. Considering the nature of the design this will not take as long as with a conventional wind turbine. Most components of the kite and ground station can be recycled. The battery recycling will be taken care off by a third party, rare earth metals will be extracted and reused. The lithium can also be reused but at the moment it is not done due to high costs compared to lithium mining but in the future it will definitely be necessary. Carbon fiber can be reused but not for similar purposes, the carbon fiber resulting from this recycling process will not be as strong as 'new' carbon fiber so it will be used in applications where strength requirements are not as high as in aerospace.

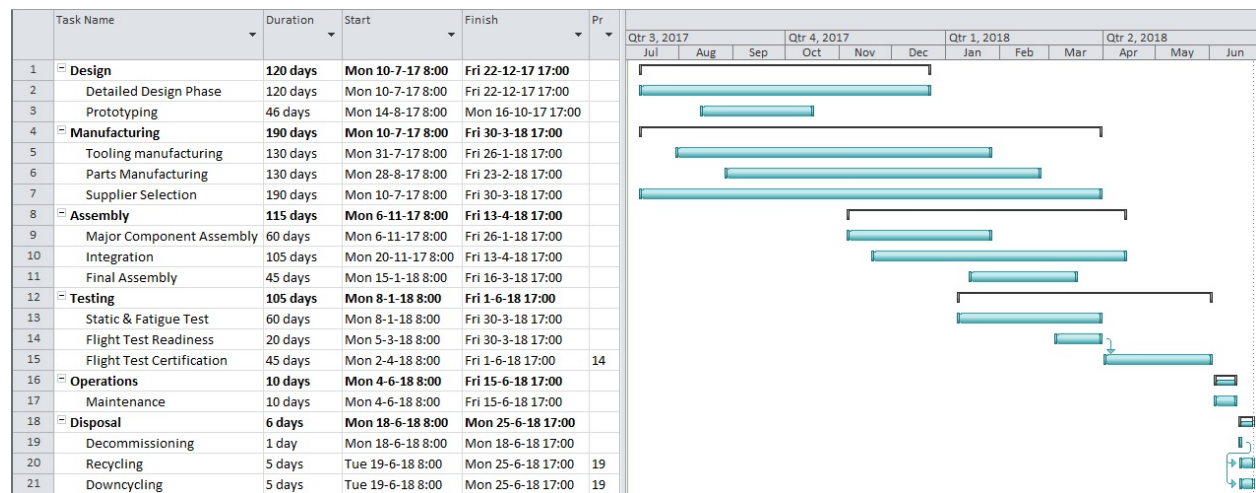


Figure 13.2: Gantt chart of future development

13.2 Operations & logistics

This section describes the operations and logistics concept. The complete operations and logistics diagram is presented in appendix E. In this flowchart, the support and maintenance is shown for one system, from system implementation to end-of-life.

New system The diagram is initiated by the introduction of a complete, new system, consisting of a kite and ground station. After production, post-production checks and transportation, this system is placed at a certain location to start generating power. After placement, the operational cycle is started at the point of pre-flight inspection.

Pre-flight operations Before nominal power producing flight is initiated, several final checks are performed by the operator, to ensure the system is in flight worthy condition. If an error or defect is encountered, the nominal flight is not initiated. Instead, the unscheduled maintenance section of the diagram is run through to fix the issues. If there are no issues, the aircraft and operator's workspots are cleaned, and nominal flight is started.

Nominal flight The nominal flight phase contains all operations performed autonomously by the system during power production, these are shown in more detail in appendix 3.1. Nominal flight is terminated by the occurrence of either of the following three events: the interval for scheduled maintenance has been reached, a system failure is detected, or degraded performance is observed with respect to predicted performance. For all three cases, the system is landed, and an operator is dispatched, who starts by performing an overall inspection of the system.

Scheduled maintenance In case of no unforeseen or unscheduled defects, regular maintenance is performed as prescribed. Required components and materials are brought over from inventory. After the maintenance, the system is checked again before initiating flight, to ensure correct performance. In the rare case the inspection yields no defects, and no maintenance is planned, the system is moved into pre-flight checks directly.

Unscheduled maintenance If the inspection does reveal unforeseen defects, three cases are proposed: a repairable defect, a defect solvable by replacing a component, or an unrestorable failure. A repairable defect is solved by taking the correct materials from inventory, and performing the required repairs on the system. In case a component cannot be repaired, it is attempted to replace the component with a new part from inventory. The old component is recycled as much as possible, the remainder is disposed of. In the extreme case where either the ground station or the kite are totaled, or both, end-of-life of the system has been reached. Each unexpected failure or service is to be carefully documented and evaluated, to ensure the design does not hold any major flaws, impairing the system's performance.

End-of-life In case the complete system is totaled, it is recycled as much as possible, and the remainder is disposed of. A new system can then be implemented again. If either the kite or ground station has survived, the other sub-system is introduced, completing the system again.

14 | Requirements compliance

This chapter shows the requirements compliance matrices in section 14.1, indicating which requirements are met and which are not met. Section 14.2 elaborates on the requirements that have not been met, by discussing the reasons and if appropriate, actions that are to be taken to fulfil those requirements.

14.1 Requirements compliance matrix

The requirements compliance matrices show all requirements, as stated in the baseline report [20]. The requirements compliance matrix has been split up in an operational part, shown in table 14.1, and a technical part, found in table 14.2. A partially met requirement indicates that at least one of the sub-requirements has not been met. Where appropriate, values for the final design have been included.

Table 14.1: Operational requirements compliance matrix

ID	Requirement	Value	Compliant
2	The system shall perform the mission within constraints	-	Partially
2.1	The system shall conform to sustainability constraints	-	Yes
2.1.1	The system shall be designed with a low environmental footprint	-	Yes
2.1.1.1	The system shall not introduce any materials or fluids to the environment	-	Yes
2.2	The system shall conform to financial budget constraints	-	Partially
2.2.1	The system, including R&D costs, shall have a cost price of no more than €40,000, excluding taxes, for one complete system	€ 66,500	No
2.3	The system shall conform to regulations	-	Yes
2.3.1	The system shall meet all regulations as stated by ICAO	-	Yes
2.4	The system shall conform to the schedule	-	Yes
2.4.1	The system shall be designed by a 10 FTE team within 11 weeks	-	Yes
2.4.2	The system shall have a functional lifetime of 20 years	-	Yes
2.4.3	The system shall require maintenance no more than once every three months	-	Yes
2.5	The system shall conform to structural constraints	-	Partially
2.5.1	The system shall not fail due to ground wind speeds up to 32.7 m/s	-	Yes
2.5.2	The system shall have a ground equipment mass of no more than 300 kg	3,000 kg	No
2.5.3	The system shall use no more ground space than a circle with a 10 m radius	10 m	Yes
2.5.4	The system shall be transportable in a space of 6.1x2.44x2.59 m	6.1x2.44x2.59 m	Yes
2.5.5	The system shall be scalable to a 2MW AWE system	92 kW	No
2.5.5.1	The system shall be scalable to launch an aircraft with a mass of 3,000 kg	75 kg	No
2.5.5.2	The system shall be scalable to launch an aircraft with a wingspan of 40 m	10 m	No

Table 14.2: Technical requirements compliance matrix

ID	Requirement	Value	Compliant
0	The system shall perform the mission	-	Partially
1	The system shall perform the mission technically	-	Partially
1.1	The system shall conform to the 2014 DSE AWE system	-	Yes
1.2	The system shall perform all flight operations	-	Yes
1.2.1	The system shall launch the aircraft	-	Yes
1.2.1.2	The system shall reach nominal flight state	-	Yes
1.2.1.3	The system shall calculate the required launch trajectory	-	Yes
1.2.1.4	The system shall perform a launch manoeuvre at a minimum ground wind speed of 0 m/s	0 m/s	Yes
1.1.1	The system shall launch an aircraft with a mass of no less than 42 kg	75 kg	Yes
1.1.2	The system shall add no more than 10 kg to the airborne clean aircraft mass	34 kg	No
1.2.1.6	The system shall have a maximum cable tension during launch of 4 kN for a 6 mm diameter cable	<40 N	Yes
1.2.1.7	The system shall perform a launch manoeuvre at a maximum wind speed of 25 m/s at 10 m altitude	25 m/s at 100 m	No
1.2.1.8	The system shall give the aircraft an altitude of no less than 30 m within a radius of 100 m of the ground station	-	Yes
1.2.1.9	The system shall give the aircraft an altitude of no less than 50 m within a radius of 150 m of the ground station	-	Yes
1.1.3	The system shall induce a drag addition of no more than 10% of the clean aircraft drag	15%	No
1.1.4	The system shall not hinder the aircraft's nominal operations	-	Yes
1.2.4	The system shall determine when nominal flight must be aborted	-	Yes
1.2.3	The system shall land the aircraft	-	Yes
1.2.3.1	The system shall perform a landing manoeuvre at a minimum ground wind speed of 0 m/s	0 m/s	Yes
1.2.3.2	The system shall perform a landing manoeuvre at a maximum wind speed of 25 m/s at 10 m altitude	-	Yes
1.2.3.3	The system shall perform a landing in a maximum 10 deg of cross-wind	-	Yes
1.2.3.4	The system shall perform a landing with a vertical positioning error of no more than 1 m	-	Yes
1.2.3.5	The system shall calculate the required approach trajectory	-	Yes
1.2.3.6	The system shall correct for a missed approach	-	Yes
1.2.3.6.1	The system shall detect a missed approach	-	Yes
1.2.3.6.2	The system shall perform an alternative landing	-	Yes
1.2.3.7	The system shall perform a landing with a horizontal positioning error of no more than 2 m	-	Yes
1.2.3.8	The system shall not fail due to the crash of a single aircraft	-	Yes
1.2.3.9	The system shall land the aircraft within 6 minutes of nominal flight termination	-	Yes

14.2 Feasibility analysis

In this section the requirements that have not been met are discussed, in order of requirement's ID.

Requirement 1.1.2 The requirement assumes an initial kite mass of 41 kg [19], to which no more than 10 kg of mass may be added. During the design, however, it was found that this estimation was too low, as several mounting points and components had been excluded, as well as coating. The requirement has been re-evaluated with the tutor and coaches, and with the team's clients. It was agreed upon that the requirement could be violated, to enable a realistic design. Mass still was to be kept in check, however, to not compromise the system's flight envelope, as higher mass increases the stall speed, raising the minimum wind required for power generation. It was concluded that the average cycle power was to be leading in the mass sizing.

Requirement 1.1.3 The added rotors increase the drag of the kite by 15%, which is more than the allowed 10%. However, due to the added winglets, the C_L/C_D of the kite increases, which increases the power output. Failing to meet this requirement is therefore considered irrelevant.

Requirement 1.2.1.7 Launching the kite at a wind speed of 25 m/s at 10 m altitude was found to be meaningless, since this would mean that the wind speed at operational altitude is above the cut-out wind speed. Therefore the system has been designed such that the kite can be launched with a wind speed of 25 m/s at its operational altitude of 100 m. This has been agreed upon by the clients.

Requirement 2.2.1 The cost of the total system (kite and ground station) of €66,500 is more than the allowed €40,000. This requirement was initially describing the launching and landing system excluding the kite. However, now that the launching and landing system has been partly integrated into the kite, it is difficult to subdivide the total system costs over these system components. The only known parameter is the ground station cost of only €21,000. Failing to meet this requirement is therefore considered acceptable.

Requirement 2.5.2 A ground station mass of 300 kg has been deemed unrealistic, this has been agreed upon by the tutor and coaches, and with the team's clients. No new ground station mass requirement has been proposed.

Requirements 2.5.5, 2.5.5.1 and 2.5.5.2 The requirements on scalability have shown to be killer requirements during the design process. After discussing this with the client, it was concluded that providing a conceptual description of a scalable version of the design would be sufficient.

Conclusion

The purpose of the report is to provide a detailed design of an automated Airborne Wind Energy (AWE) system, focusing on autonomous launching and landing of the rigid aircraft. The main requirement stated that the launching and landing system should be designed for the rigid kite of the Fall 2014 DSE group 03 [19]. It was derived that a Vertical Take-off and Landing concept (VTOL) is the best approach to meet the performance requirements and design constraints. Furthermore, the concept also meets reliability, availability, maintainability and safety requirements.

The VTOL concept refers to the addition of motors and propellers to allow for vertical take-off and landing of the rigid kite. In the preliminary design phase of the VTOL concept, two propellers are added to the rigid kite by using winglets. The VTOL concept scored well in the maintenance and reliability criterion of the trade-off. The risk map for the concept shows a low number of likely and catastrophic failures.

The addition of VTOL to the AWE system is further analysed in this report to get to a detailed design. This is first done using systems engineering tools such as the functional flow diagram, the N2 chart, the communication flow diagram and the technical risk analysis. In the N2 chart, the power system, sensors, propulsion unit, control surfaces, autopilot system, communication system, winch system and ground station system are identified. It is identified that the autopilot system is a key component of the overall design as it is important for control, communication and overall performance of the rigid kite during launching and landing but also during nominal flight. The fault tree analysis shows that there are multiple sources of failure in the system. These include tether breakage, propulsion unit shutdown and autopilot failure.

Based on the results of the previous mentioned systems engineering tools the subsystems aerodynamics, stability & control, power & propulsion and structures were analysed in detail. For power & propulsion, this resulted in a design with two vertically oriented main rotors on a winglet with a 1 m offset to the wing and a rotor on the vertical tail that can rotate 90 deg; in this way, it can be oriented both horizontally and vertically. Their rotor radii are respectively sized to 54 cm and 31 cm. The motors to drive these rotors were sized as well and found to require a maximum power of respectively 35 kW and 7 kW and have a mass of respectively 3.2 kg and 1.3 kg. This required power is delivered by batteries that have a total mass of 18 kg.

The structure of the kite is altered to house the added components such as the batteries, shift the centre of gravity to make the kite stable and to create the winglets. An analysis is done to make sure that the structure can handle the loads generated during nominal flight with a maximum apparent velocity of 35 m/s. The critical part of the structure is the tail beam, but when using the high strength carbon fibre T700S it can handle the loads generated during nominal flight. For the ground station the drum and tether diameter are sized by setting a desired lifetime and were found to become 768 mm and 8.15 mm respectively.

In the analysis of the aerodynamics of the kite it was found that the winglets improve the lift over drag ratio. The wing download is estimated to be 8%, which means that 8% of the thrust generated is lost by rotor/wing interaction. In the stability and control analysis it was found that the kite can achieve longitudinal equilibrium in hover and climb using tail thrust and elevator deflection. The rigid kite requires active stabilisation to maintain equilibrium in longitudinal plane. An analysis of the flight path resulted in a maximum required total thrust of the main rotors ranging from 875 N to 1000 N. A range of tail rotor thrust up to 130 N is required during critical conditions for climb and equilibrium requirements. An energy efficient solution for landing the rigid kite was also explained.

Since eventually this project is done to come up with a profitable AWE system, the average power per cycle is determined for different reference wind velocities. Found was a rated power per cycle of 116 kW, an average power per cycle of 43 kW and a capacity factor of 38%. When combining the energy generated with the estimated costs per system that was found to be €65,374, the return on investment is 11% when the energy produced is sold for €95/MWh. The market analysis showed that if the energy is sold for this price, the system is a competitive product while having room and profit to keep on innovating.

Recommendations

Due to limited time and resources various research areas were left unexplored and should be further investigated. This chapter describes the recommended steps to further analyse and improve the system. However, before discussing improvements of the concept and the models and future design validations, a mistake which has been made when setting up the mass budget is described.

Mass budget error

While setting up the mass budget of the kite an error has been made in the average density calculation of the sandwich panels, shown in table 3.2b. Only the mass of the foam and resin uptake had been taken into account, the carbon fibre facing has been left out of this estimation. After the addition of the 1 mm of carbon fibre laminate (2 faces of 0.5 mm each), a resulting density of 175 kg/m^3 is obtained, by taking a weighted average between the foam's density and the carbon fibre's density. Altering the assigned densities for the panels to this new value results in a total estimated mass of 97 kg, and a design mass of 106.7 kg. The rotor, motor and battery sizing have to be re-iterated upon to allow for this extra mass in the VTOL manoeuvres. With the new estimation, the centre of gravity is located at 576 mm from the wing leading edge, still within the margin limited by the neutral point and motor placement.

Design improvements

For further research, the following alterations to the concept could be analysed. These alterations have been considered but not yet analysed in detail.

- Since the internal structural of the kite was based on the design of the 2014 DSE group 03, the kite is limited to an apparent kite velocity of 35 m/s. This apparent kite velocity is currently a limiting factor on the output power of the system. It is therefore strongly advised to redesign the wingbox and the tail beam in particular, such that they can withstand the higher loads from the increased apparent kite velocity.
- To save battery mass, a power cable can be plugged into the kite during launch. At a certain altitude, the cable is released, and slides back along the tether. After the kite has landed again, the cable is plugged back into the kite autonomously.
- The structure of the tail beam can be further optimised by applying uni-directional carbon fibre in longitudinal direction. The extra tensile strength will help to carry the bending moment, such that the mass of the tail beam can be reduced.
- The internal structure of the tether drum can be analysed in more detail, such that its mass moment of inertia can be reduced. This will result in a higher power output.
- The third rotor may be attached to the nose instead of the tail. The winglets can then be swept back further which may increase their effectiveness. Also, the kite will become more stable as the centre of gravity shifts forward. However, it may be that the total mass is increased due to the use of three large, lifting rotors in stead of two large rotors and the small tail rotor. Pitch and yaw control in hover may also be more difficult, due to the smaller arm at the nose.
- The rotors can be given a more optimal twist distribution, which will increase their efficiency.
- The amount of attachment points of the split bridle could be changed to decrease the mass of the internal structure of the wing. A trade-off should be made between this mass reduction and the added drag from the extra tether lines.

Model improvements

Power model

In the current power model, accelerations of the kite are neglected. Especially during reel-in this can make a significant difference in the amount of power it costs to reel the kite in. This is because high velocities need to be reached in a short time, for which high accelerations are needed that require high input power. Making a dynamic model instead of a quasi-static one gives a more refined outcome but with a lower average power per cycle.

Also as mentioned above, the apparent kite velocity is limiting the output power. Improving the structure to handle the loads generated by higher apparent kite velocities can increase the power output a lot.

Vertical take-off model

The vertical take-off model could be improved by further optimising the launch strategy for energy consumption. Currently, the launch strategy considered assumes a constant climb velocity and a constant pitching angle. This could be improved by considering a more complex launch strategy which has a variable vertical climb velocity and a variable pitch. Additionally, the possibility of winching the kite up to its operational altitude after it has been given an initial altitude with the rotors could be considered. Secondly, the vertical take-off model could be improved by analysing stability and controllability of the kite during flight or hover in wind gusts. These wind gusts could be modelled by generating random inputs on the wind direction and velocity.

Rotor model

Within the rotor model, the assumption of uniform inflow was made. For further research, this assumption should be eliminated to better represent and improve the actual rotor performance.

Structural model

In addition to the static loading analyses, the dynamic loading from the mass at the wingtip during nominal flight should be investigated. Although the point masses will cause wing bending relief, harmonic excitations near the natural frequency of the wing due to aeroelastic bending should be studied carefully. Additionally, the dynamic loading from the rotors on the wing during vertical take-off should be studied to ensure that the natural frequency of the wing and the rotational velocity of the rotors do not coincide.

Centralised system model

A final modelling step could be to combine the tether model, power model, rotor model, battery model, mass estimation and climb/stability model into one complete model, simultaneously sizing the system, or providing a relatively accurate system sizing. This will help to speed up the iterations, and will lead to a faster convergence to an optimised design.

Design validation

The following steps are required to validate the design. These validation steps have not been executed yet due to limited resources.

- The theory used to judge the rotor-wing interaction should be validated by measuring the maximum effective thrust delivered by the rotors during vertical take-off. Section 9.5.2 discusses several suggestions for future development on this topic.

- The aerodynamic coefficient curves of the kite should be validated with a CFD analysis or wind tunnel data. Unforeseen effects may be present at the high angles of attack and lift coefficient the kite is flown at. It is currently difficult to precisely calculate these coefficients because of the complex wingtip configuration.
- Validation of tether lifetime is required, since fatigue is difficult to model. This can be done by measuring the mean time to failure of the tether.

Bibliography

- [1] Siemens AG. What is the real cost of offshore wind energy? Technical report, Siemens, 2014.
- [2] AkzoNobel. *Aerodur® Primer S 15/90 technical datasheet*. AkzoNobel Aerospace Coatings, August 2009.
- [3] AkzoNobel. *Eclipse technical datasheet*. AkzoNobel Aerospace Coatings, February 2015.
- [4] R. W. Beard and T. W. McLain. *Small Unmanned Aircraft: Theory and Practice*. Princeton University Press, 2012. Chapter 4.
- [5] International civil aviation organisation. *Manual of the ICASO standard atmosphere*. International civil aviation organisation, 1993.
- [6] J. S. Light F. F. Felker. Aerodynamic interaction between a rotor and wing in hover. Technical report, NASA Ames research center, Moffett Field, California, April 1988.
- [7] R.C. Hibbeler. *Mechanics of Materials*. Pearson Prentice Hall, 2013.
- [8] S. Newman J. Seddon. *Basic Helicopter Aerodynamics, Third Edition*. Wiley Aerospace, 2011.
- [9] J. van der Vaart E. de Weerd C. de Visser A. in 't Veld E. Mooij J.A. Mulder, W. van Staveren. Ae3202 flight dynamics lecture notes. unpublished lecture notes, 2013.
- [10] A.L. Rogers J.F. Manwell, J.G. McGowen. *Wind Energy Explained*. Wiley, 2009.
- [11] Jr. John D. Anderson. *Fundamentals of aerodynamics*. McGraw-Hill, 2011.
- [12] John D. Anderson Jr. *Introduction to flight*. McGraw-Hill, seventh edition, 2012.
- [13] Timothy S. Swan Mark D. Maughmer and Steven M. Willits. The design and testing of a winglet airfoil for low-speed aircraft. Technical report, The Pennsylvania State University, 2001.
- [14] T.H.G. Megson. *Aircraft Structures for Engineering Students*. Elsevier, 2007.
- [15] F. Bouwman Y. Chiodi R. R. Fanijten T. J. S. Gertsen D. H. A. Groeneveld Y. C. Heije J. W. D. Kroese M.T. van Beek, G. J. Bouman and D. Sud. Dse - airborne wind power, mid-term report. Technical report, Delft University of Technology, 2017. DSE 2017 Mid-term report.
- [16] RWE npower renewables. Wind turbine power calculations. Technical report, The Royal Academy of Engineering, n/a.
- [17] Magdi Ragheb and Adam M. Ragheb. Wind turbines theory - the betz equation and optimal rotor tip speed ratio. Technical report, InTech, 2011.
- [18] Kai Beng Yap R.C. Hibbeler. *Mechanics for Engineers: Statics*. Pearson Prentice Hall, 2012.
- [19] M.T. Islam R.J. Kruithof K. Lindeborg R.J. Meijer F.T. Ndonga T. Smitsn R.J. Coenen, S. Drenth and M.L.W. Veraart. Dse - airborne wind power. Technical report, Delft University of Technology, 2015. DSE 2014 group report.
- [20] M.T. Islam R.J. Kruithof K. Lindeborg R.J. Meijer F.T. Ndonga T. Smitsn R.J. Coenen, S. Drenth and M.L.W. Veraart. Dse - airborne wind power, baseline report. Technical report, Delft University of Technology, 2017. DSE 2017 baseline report.
- [21] T.L.Saaty. Decision making with the analytic hierarchy process. *Int. J. Services Sciences*, 1(1):83–98, 2008.

- [22] Roland Schmehl Uwe Ahrens, Moritz Diehl. *Airborne Wind Energy*. Springer, 2013.
- [23] C. N. Keys W. Z. Stepniewski. *Rotary-wing interactions*. Dover Books on Aeronautical Engineering. Dover Publications, July 1984.
- [24] David Rival Xavier Ortiz 1 and David Wood. Forces and moments on flat plates of small aspect ratio with application to pv wind loads and small wind turbine blades. Technical report, Energies, 2015.

A | Functional analysis

A.1 Functional flow diagram

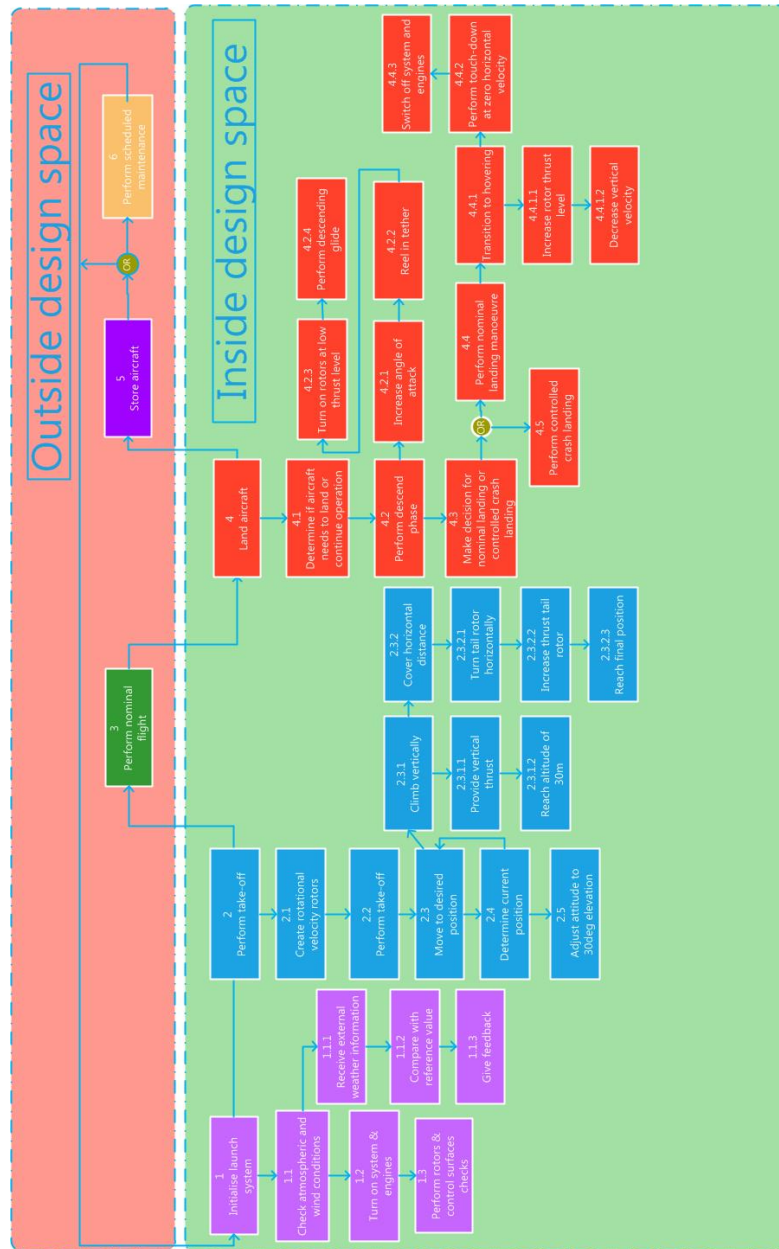


Figure A.1: Functional flow diagram of the final concept

A.2 Functional breakdown

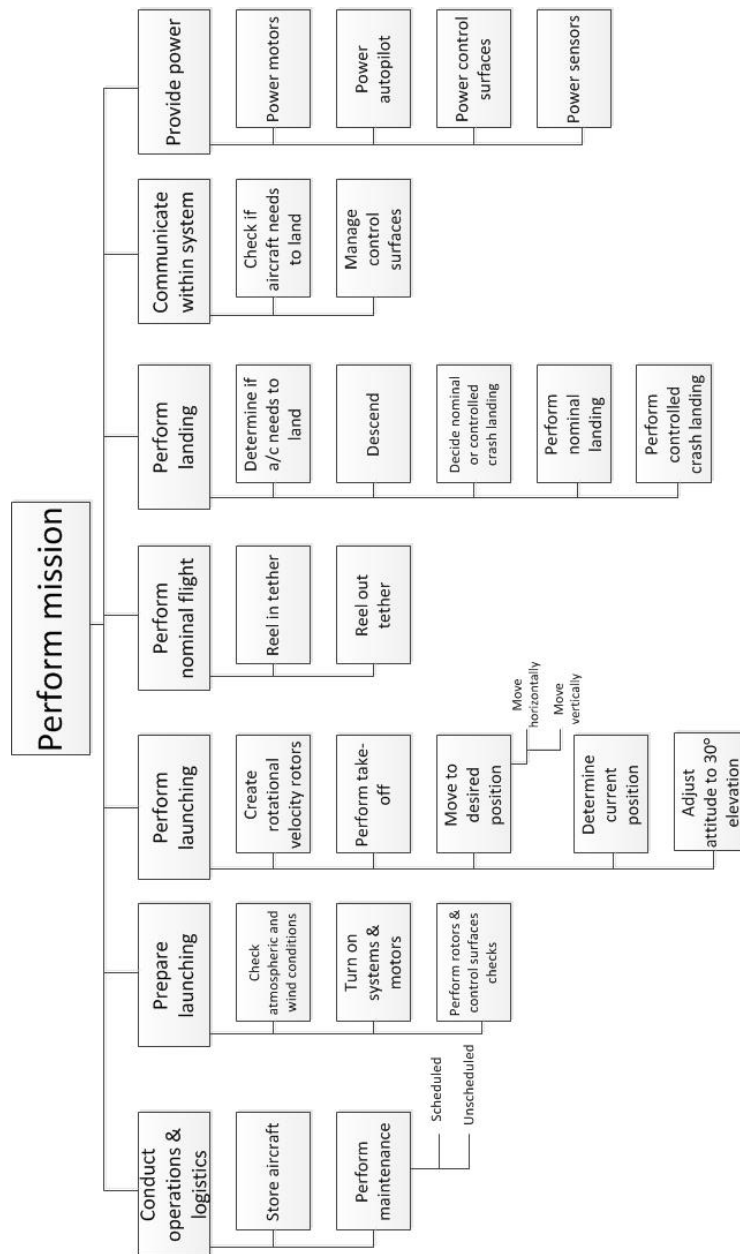


Figure A.2: Functional breakdown of the final concept

B | Fault tree analysis

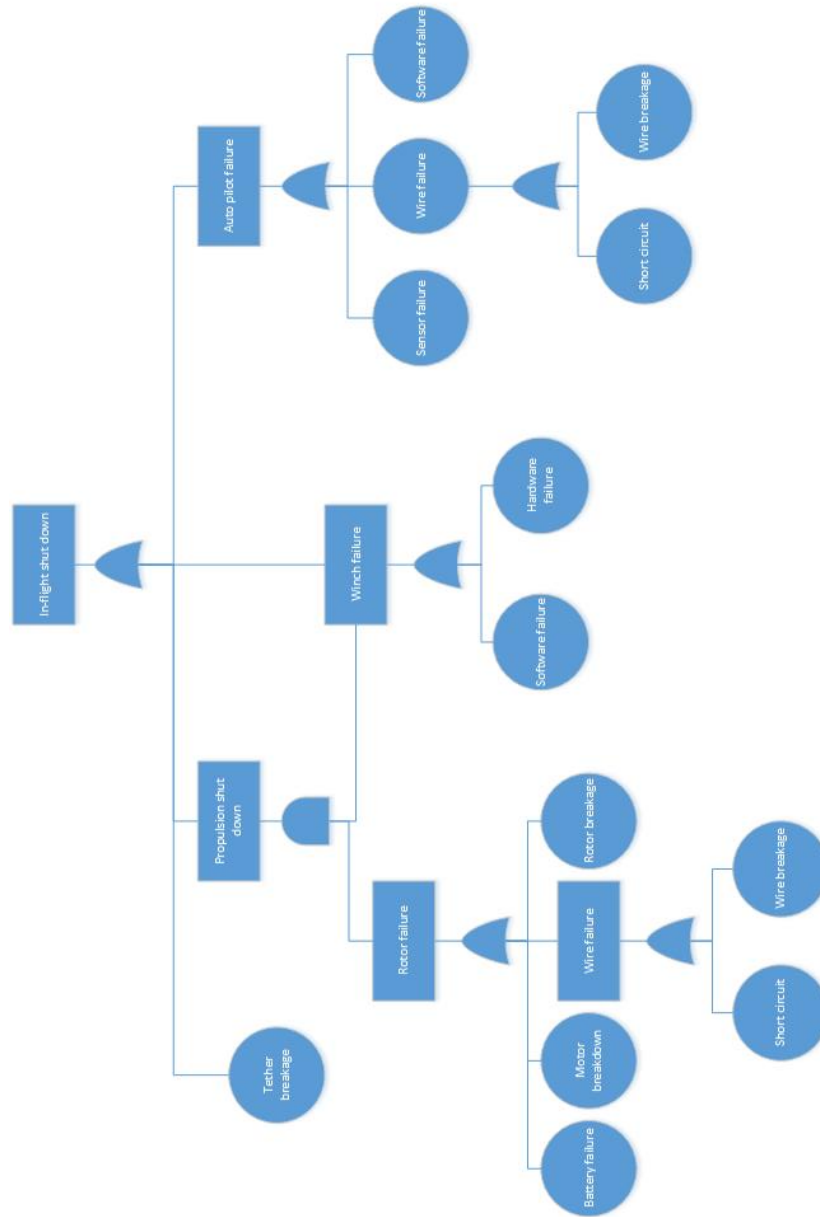


Figure B.1: Fault tree analysis of the VTOL concept

C | Cost breakdown structure

Table C.1: Development costs

Development costs				€ 930,262.36
Item	Cost [€/unit]	Unit	Amount	Subtotal
Facility costs	€ 1,000.00	Month	30	€ 30,000.00
Salaries	€ 20.00	hr.	38,400	€600,000.00
Molds wings	€ 20,000.00	pc.	4	€80,000.00
Molds tail surfaces	€ 5,000.00	pc.	4	€20,000.00
Mold tail connector	€3,000.00	pc.	2	€6,000.00
Prototype production costs	€41,420.79	pc.	3	€124,262.36
OJF testing	€15,000.00	day	2	€30,000.00
Valkenburg testing	€10,000.00	day	4	€40,000.00

Table C.2: Ground station production costs

Production cost ground station				€ 21.070
Item	Cost [€/unit]	Unit	Amount	Subtotal
Container	€2,500.00	pc.	1	€2,500.00
Drum	€50.00	pc.	1	€50.00
Generator	€5,000.00	pc.	1	€5,000.00
Pulleys	€10.00	pc.	2	€20.00
Electronics	€5,000.00	Ground station	1	€5,000.00
Rotating top	€2,000.00	pc.	1	€2,000.00
Brackets	€250.00	pc.	2	€500.00
Salaries (assembly)	€20.00	hr.	300	€6,000.00

Table C.3: Kite production costs

Production cost kite				€ 38.103
Item	Cost [€/unit]	Unit	Amount	Subtotal
Raw material costs				€10,616
Carbon fibre	€40.00	m ²	200	€8,000.00
Resin	€30.00	kg	20	€600.00
Aluminium	€0.02	cm ³	26150	€523.00
Bonding/filling pastes	€150.00	kg	2	€300.00
Rohacell IG-F 31	€36.00	m ²	19.6	€705.60
Primer	€4.00	m ²	36	€144.00
Topcoat	€4.00	m ²	36	€144.00
General mounting hardware	€200.00	general	1	€200.00
Component costs				€6,537.95
Main motor	€796.40	pc.	2	€1,592.80
ESC main motor	€1,099.00	pc.	2	€2,198.00
Tail motor	€384.30	pc.	1	€384.30
ESC tail motor	€399.00	pc.	1	€399.00
Main rotor	€50.00	pc.	2	€100.00
Tail rotor	€20.00	pc.	1	€20.00
Tubing for empennage structure	€23.00	m	4.3	€98.90
Aileron servos	€50.00	pc.	2	€100.00
Rudder/elevator servos	€30.00	pc.	3	€90.00
Main batteries	€315.00	pc.	1	€315.00
Secondary (system) batteries	€100.00	pc.	1	€100.00
Tail rotor servos	€22.95	pc.	1	€22.95
Wiring	€50.00	set.	1	€50.00
Autopilot	€232.00	pc.	1	€232.00
Processor	€10.00	pc.	1	€10.00
Transmitters/receivers	€25.00	pc.	1	€25.00
Tether	€800.00	pc.	1	€800.00
Production costs				€20,948
Salaries	€20.00	hr.	1000	€20,000.00
Peelply	€2.50	m ²	70	€175.00
Release film	€0.80	m ²	70	€56.00
Flowmesh	€ 1.90	m ²	70	€133.00
Vacuum film	€2.20	m ²	70	€154.00
Vacuum tubing	€1.00	m	70	€70.00
Tacky tape	€0.50	m	120	€60.00
Other tooling and consumables	€300.00	Kite	1	€300.00

D | Replacement costs

Table D.1: Yearly replacement costs estimation

Annual replacement costs		€4,161.32	
Item	Cost	Expected service time [y]	Cost/year
Main motor	€796.40	4	€199.10
ESC main motor	€1,099.00	4	€274.75
Tail motor	€384.30	4	€96.09
ESC tail motor	€399.00	4	€99.75
Main rotor	€50.00	4	€12.50
Tail rotor	€20.00	4	€5.00
Tubing for empennage structure	€23.00	20	€1.15
Aileron servos	€50.00	10	€5.00
Rudder/elevator servos	€30.00	10	€3.00
Main batteries	€315.00	2	€157.50
Secondary (system) batteries	€100.00	2	€50.00
Tail rotor servos	€22.95	10	€2,295.00
Wiring	€50.00	5	€10.00
Autopilot	€232.00	10	€23.20
Processor	€10.00	10	€1.00
Transmitters/receivers	€25.00	5	€5.00
Tether	€800.00	0.5	€1,600.00
Drum	€50.00	20	€2.50
Generator	€5,000.00	10	€500.00
Pulleys	€10.00	10	€1.00
Electronics	€5,000.00	5	€1,000.00
Rotating top	€2,000.00	20	€100.00
Brackets	€250.00	20	€12.50

E | Operations and logistics diagram

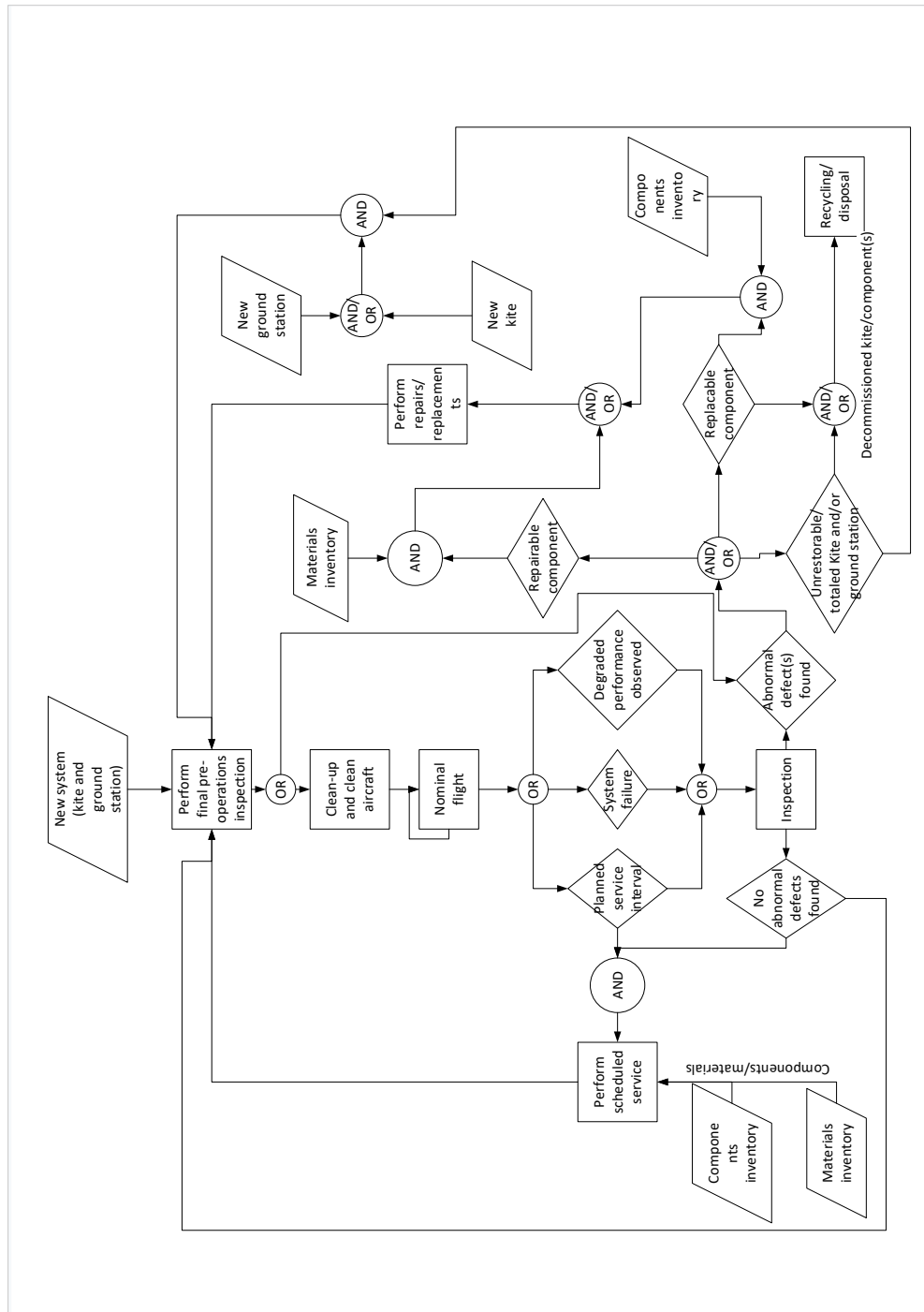


Figure E.1: Operations and logistics diagram

F | Component mass breakdown

Table F.1: Component mass estimation

Part	Mass (kg)	Number	X (mm)	M_np (Nm)
Wing skin	7.85	2.00	688.61	13.24
Spars	0.83	2.00	502.03	-1.63
Ribs	0.31	2.00	576.70	-0.16
Top panel	1.90	2.00	584.64	-0.67
Aileron	0.30	2.00	1209.42	3.51
Motor mount	0.96	2.00	511.64	-1.71
Tail connector	1.07	1.00	1462.63	9.01
Motor fairing	0.13	2.00	606.42	0.01
Main motor	3.20	2.00	499.95	-6.45
Spinner	0.02	2.00	499.95	-0.03
Rotor blade	0.04	4.00	500.00	-0.18
Horizontal Tail	0.76	2.00	4844.40	63.17
Empennage structure	0.46	1.00	4675.90	18.42
Vertical tail	0.54	1.00	4740.87	22.00
Tail motor mount	0.26	1.00	4597.07	10.34
Tail motor fairing	0.03	1.00	4601.84	1.22
Tail boom	1.90	1.00	2982.53	44.36
Tail motor	1.34	1.00	4506.25	51.12
Tail rotor	0.06	1.00	4506.25	2.37
Elevator	0.03	2.00	5096.67	2.73
Rudder	0.07	1.00	4990.99	2.97
Battery	9.00	2.00	-624.00	-216.61
Electronics	6.57	1.00	-674.00	-82.32
Body coating	0.20	2.00	530.95	-0.29
Main wing coating	1.92	2.00	756.91	5.81
Tail boom coating	0.20	1.00	2980.24	4.58
Vertical tail coating	0.23	1.00	4765.86	9.56
Horizontal tail coating	0.27	2.00	4845.48	22.79
Aileron brackets	0.05	2.00	1036.35	0.38
Rudder brackets	0.04	1.00	4990.99	1.72
Elevator brackets	0.04	2.00	5096.00	3.53
Total	68.46		577.08	
With 10% safety	75.30			

G | Task division

The tasks which have been executed are distributed amongst the team members according to table G.1.

Table G.1: Task Division

Student	Performed tasks
Maarten van Beek	Preface, Section 3.6, 3.7, 9.3, 11.3, Conclusion, Recommendation
Gijs Bouman	Section 2.1, 3.6, 5.1.5, 5.2, 5.3.2, 5.3.4, 9.5.2, 10.1.1, 10.2, 11.1, 14.1, 14.2, Recommendations, Appendix F
Frank Bouwman	Section 8.2, 9.4, 14.1, Recommendations
Yanni Chiodi	Executive summary, Section 3.3, 6.2.2, 6.2.3
Rakesh Fanijsen	Section 4.2, 7.4, 13.1, Recommendations
Thomas Gertsen	Preface, Section 2.2, 2.3, 3.8, 8.1, 10.4, Appendix B, Overall documenting
Diederick Groeneveld	Section 3.8, 5.1.1, 5.1.2, 5.1.4, 5.3.3, 7.3, 9.5.1, 12
Yannick Heijne	Introduction, Section 3.5, 7.2, 7.3, 9.2, 11.1, 11.2, Recommendations, Appendix C, D
Jurjen Kroese	Section 3.1, 3.2, 3.3, 3.4, 4.1, 7.1, 7.5, 7.6, 10.1, Appendices A.1, A.2, Jury Summary
Dikshant Sud	Section 5.1.3, 5.3.1, 6.1.1-3, 6.2.1, 6.3, V&V